UNIVERSITA' DEGLI STUDI DI NAPOLI

"FEDERICO II"

FACOLTA' DI INGEGNERIA

DOTTORATO DI RICERCA IN INGEGNERIA AEROSPAZIALE, NAVALE E DELLA QUALITA'

XIX CICLO

A STUDY OF A HIGH LIFT WING-BODY CONFIGURATION FOR LOW EARTH ORBIT RE-ENTRY

Coordinatore:

Ch.mo Prof. Ing. A. Moccia

Candidato:

Ing. Mario De Stefano Fumo

Tutor:

Ch.mo Prof. Ing. R. Monti

Ch.mo Prof. Ing. R. Savino

CONTENTS

Abstract iv

Preface v

List of Figures vii

List of Tables xiii

1 Hypersonic Lifting Flight: Past, Present and Future 1

1.1 Introduction 2
1.2 The Past: A Historical Perspective on Hypersonic Flight Vehicle 2
1.3 The Actual International Programs and Objectives 9
1.4 Future Development 13
1.5 Summary and Comments 15
Bibliography 15

2 System Concept and Missions Requirements 18

2.1 Introduction 19
2.2 Atmospheric Entry 19
2.3 System concept approach 21
2.4 The Boundary Layer Thermal Protection System 25
2.4.1 The effect of thermal conductivity: comparison between local and global radiative equilibrium 29
2.4.2 The role of the angle of attack 31
2.4.3 The role of chemical non equilibrium and surface catalysis 34
2.5 Main Vehicle Constraint 36
2.6 Mission Architecture 38
2.7 Summary and Comments 40
References 40

3 Vehicle Model 43

3.1 Vehicle Description and Characteristics 44
3.2 Aerodynamic Dataset 44
3.2.1 Description Of The Reference Frame 45
3.2.2 Description of the Numerical Model 46
3.2.3 Convergence Criteria for CFD Computations 47
3.2.4 Comparison of the two Numerical Models 49
3.2.5 Computation of Aerodynamic Coefficients 49
3.2.6 Effect of Mach number 56
3.2.7 Reynolds number effects 58
3.2.8 Hypersonic Performance 61
3.2.9 Aerodynamic Efficiency at Landing Conditions 63
3.3 Structure and Thermal Protection 67
3.4 Summary and Comments 67
References 68

4 Re-entry Trajectories Evaluation 70

4.1 Introduction 71
4.2 Trajectory Code Description 71
4.2.1 Approximate Aerothermal Analysis 73
4.2.2 Entry Code Validation 74
4.3 Entry Corridors 75
4.4 Computation of Entry Trajectories 78
4.5 Effect of Aerodynamic Bank Manoeuvre 84
4.6 The ground track 86
4.7 Comparison with the Space Shuttle re-entry. 88
4.8 Summary and Comments 90
References 90

5 Aerothermal Load and Thermal Protection System 92

5.1 Introduction 93
5.2 Evaluation of Heat Fluxes for the Most Critical Re-entry Conditions 93
5.2.1 Fuselage Nose 93
5.2.2 Wing 99
5.3 A simplified analysis for comparison with Space Shuttle heating. 100
5.3.1 Laminar-Turbulent transition evaluation 102
5.4 Thermal Analysis 106
5.5 Time- dependent computations 112
5.6 Thermal Protection System Layout 117
5.6.1 Nose and Wing Leading Edges Concept 117
5.6.2 Fuselage TPS 118
5.7 Summary and Comments 120
References 120

6 Conclusions 122

ABSTRACT

This study investigated the atmospheric re-entry of a winged body from low Earth orbit using a new strategy of re-entry based on the exploitation of the lift force. One of the main objectives of this work was to assess the potential impact on the system performance that results from the introduction of sharp nose and wing leading edges. A vehicle and a mission architecture are defined for Low Earth Orbit re-entry. A dedicated re-entry code was developed for trajectory computations. The vehicle is modelled as a point mass with three degree of freedom characterized by aerodynamic coefficients determined using panel and approximate method and Computational Fluid Dynamics. Constraint to the re-entry are identified and the re-entry corridors are defined. Aerothermal loads are evaluated by means of approximate formulas and Computational Fluid Dynamics in order to define the Thermal Protection System layout.

PREFACE

This study was initiated as a result of the increased interest of different national space agencies in the development of a small and fully reusable re-entry vehicle that could be launched on the top of a new generation evolved expendable launch vehicle. The necessity of an Orbital Space Plane was a reflection of NASA desires for a system that acts in a dual role as "lifeboat" to get the crew home from ISS in an emergency, and for ferrying crewmembers to the space station more economically and safely than the Space Shuttle currently can does. Furthermore, the even more growing interest for space commercialization for tourism ask for a vehicle with similar requirements.

The choice of a winged body in opposition to a ballistic capsule (Soyuz, Apollo-like) is mainly dictated by the higher lift to drag ratio allowing a significant increase in operation flexibility (larger down and cross-range and the possibility of landing on a conventional runway) and quality of flight (low decelerations).

The object of this work is to demonstrate the feasibility of a winged body with sharp leading edge (radius of curvature less equal to ten centimetres) for a Low Earth Orbit re-entry focusing on the re-entry trajectory and aerothermal environment.

Furthermore this work investigates a new re-entry strategy, of a winged vehicle with high aerodynamic efficiency, able to dissipate the high energy associated to the orbital speed in the atmosphere of the Earth. This objective must be accomplished by containing mechanical and thermal stresses, within the limits allowed for both the spacecraft and the flight crew.

This work has been developed during the last three years and it is now presented in the form of final dissertation in partial fulfilment of the requirements for the Ph.D. in Aerospace Engineering.

The first chapter is dedicated to a quick overview of past, present and future activities on hypersonic sustained flight. Particular interest is devoted to the evolution of hypersonic lifting configurations.

The second chapter deals with the identification of the reference missions for a feasibility analysis of a winged re-entry vehicle and with the identification of the main requirements of the whole re-entry system.

The third chapter introduces the aerodynamic characteristics and some of the performances parameters of the considered re-entry vehicle.

In the fourth chapter a detailed description of re-entry code will be furnished together with some validation results. The re-entry strategy will be discussed and the re-entry corridors allowing a safe re-entry will be identified.
The final chapter is devoted to a deeper analysis of the thermal environment during the re-entry trajectory. In particular CFD computations on the nose and on the wing of the vehicles will be presented. Furthermore a thermal analysis of the main elements of the re-entry vehicle will be reported in order to identify the thermal protection system layout.

Finally I would like to express appreciation to my tutors for their full support and guidance throughout the course of this three years. In particular I due my thanks to Prof. Rodolfo Monti for his ever clear explanations and to Prof. Raffaele Savino for our “constructive” discussions. I owe a great thank to Dr. Diego Paterna for his valuable help in this research effort and for his friendship. I would like also to thank my colleague of Ph.D. course, and friend, Arturo Francese for the collaboration in the many research activities performed. A special thanks goes to Davide, Lello and Stefano, for their “true” friendship demonstrated during these years. I cannot forget to be grateful for the support at home provided by my family, which allowed me to achieve this objective. And finally I would like to express my heartfelt appreciation to my “nearly wife” Francesca for her support and endurance throughout my studies. To her I owe thanks for helping me to maintain perspective and always focus on the important things in life.

Mario De Stefano Fumo

LIST OF FIGURES

Figure 1-1. The X-15, first hypersonic plane
Figure 1-2. The M2-F2, final configuration.
Figure 1-3. X-20 Dynasoar prototype configuration.
Figure 1-5. The ASSET and the PRIME.
Figure 1-6. X-24B in flight
Figure 1-7. Mig-105-11 in Monino Air Force museum
Figure 1-8. BOR-4S at MACS in Zhukovski (Sub-scale 1:2)
Figure 1-8. Artistic view of theX-33 and the X-38 prototype flight test
Figure 1-9. Four concepts for the Orbital Space Plane (OSP) design released by NASA
Figure 1-10. Clipper manned spacecraft (with SHM)
Figure 1-11. Artistic view of the IXV.
Figure 1-12. Phoenix on the runway
Figure 1-13. USV FTB-1 and FTB-X.

Figure 2-1. Entry corridor.
Figure 2-2. Re-entry trajectories.(a) orbital re-entry; (B) Apollo re-entry.
Figure 2-3. Energy dissipation rates for Shuttle and the proposed vehicle
Figure 2-4. Implications and consequences of a low risk re-entry trajectory
Figure 2-5. Local radiative equilibrium temperature on a 2-D body at zero and 25° of the angle of attack (M_∞=14.8; Z=60Km).
Figure 2-6. Geometry and configurations of the sphere-cone.
Figure 2-7. Effect of the ZrB_2 nose insert length. Configurations 1 and 2 (axis-symmetric).
Figure 2-8. Effect of a SiC insert. Configurations 3 and 4 (axis-symmetric)
Figure 2-9. Locations of the four stations.
Figure 2-10. Convective heat flux at different station along the body at an angle of attack of 15° axis-symmetric body.
Figure 2-11. Temperature at different station along the body at zero angle of attack (dashed perfect circles) and at an angle of attack of 15°(solid curves)axis-symmetric body.
Figure 2-12. Surface heat flux at different station along the nose-cone body at an angle of attack of 15°(axis-symmetric body).

Figure 2-13. Global radiative surface temperature for a fuselage at different angle of attack (3-D).
Figure 2-14. Temperature distributions on axis-symmetric body at zero angle of attack.
Figure 2-15. Temperature distributions on axis-symmetric body at 25°of angle of attack.
Figure 2-16. Re-entry corridors
Figure 2-17 – Possible trajectories in the Z-V plane
Figure 2-18. Reference mission 1: LEO re-entry
Figure 2-19. Vehicle architecture.

Figure 3-1. Re-entry vehicle configuration.
Figure 3-2. Geometry and reference frame (half model)
Figure 3-3. Surface mesh; a) Top view; b) Bottom view
Figure 3-4. Block traces (in different colours) on the vehicle surface
Figure 3-5. Lift coefficient profile during CFD iterations (M=0.3; α=20°)
Figure 3-6. Drag coefficient profile during CFD iterations (M=0.3; α=20°)
Figure 3-7. Pitching moment coefficient profile during CFD iterations (M=0.3; α =20°)
Figure 3-8. Pressure coefficient distribution corresponding to M=0.3, α=20°
Figure 3-9. Pressure coefficient distribution corresponding to M=2, α =10°
Figure 3-10. Pressure coefficient distribution in the symmetry plane (M=0.3, α=20°)
Figure 3-11. Pressure coefficient distribution in the symmetry plane (M=2, α=10 [deg]).
Figure 3-12. Lift coefficient vs. angle of attack (M=0.3, M=0.9)
Figure 3-13. Drag coefficient vs. angle of attack (M=0.3, M=0.9)
Figure 3-14. Pitching moment coefficient vs. angle of attack (M=0.3, M=0.9)
Figure 3-15. Lift coefficient vs. angle of attack (hypersonic regime)
Figure 3-16 – Drag coefficient vs. angle of attack (hypersonic regime)
Figure 3-17. Aerodynamic efficiency vs. angle of attack (hypersonic regime)
Figure 3-18. Lift coefficient vs. Mach number
Figure 3-19. Drag coefficient vs. Mach number
Figure 3-20. Lift slope coefficient vs. Mach number
Figure 3-21. Pitching moment coefficient vs. lift coefficient
Figure 3-22. Grid refinement accounting for viscous effects.
Figure 3-23. Pressure distribution on vehicle surface at M=0.3, α=20 deg.
Figure 3-24. Pressure distribution on vehicle surface at M=0.9, α =20 deg;
Figure 3-25. Pressure distribution on vehicle surface at M=5, α =13.6 deg;
Figure 3-26. Comparisons for seven lifting re-entry configurations.

Figure 3-27. Comparison of hypersonic lift-to-drag ratio for different lifting re-entry configurations.
Figure 3-28. Incremental lift, drag and pitching moment coefficients in ground effect for the X-34 vehicle.
Figure 3-29. Lift coefficient vs. angle of attack (M=0.2)
Figure 3-30. Drag coefficient vs. angle of attack (M=0.2)
Figure 3-31. Pitch moment coefficient vs. angle of attack (M=0.2, moment centre=nose)
Figure 3-32. Aerodynamic efficiency vs. angle of attack (M=0.2)
Figure 3-33. Lift to drag ratio for the X-34 vehicle (Ref. 1)
Figure 3-34. Pitch moment coefficient vs. angle of attack around the centre of gravity (M=0.2)
Figure 3-35. Vehicle frame and thermal and structure detail.

Figure 4-1. Atmospheric entry reference system and nomenclature
Figure 4-2. Nominal and optimal Apollo re-entry trajectories comparison between present computation and Young &Smith, 1967.
Figure 4-3. Re-entry from orbit comparison between present computation and ASTOS
Figure 4-4. Conditions at the entry interface by a single de-boost ΔV
Figure 4-5. Conditions at the entry interface
Figure 4-6. Trajectories obtained with different single de-boost ΔV
Figure 4-7. Re-entry trajectories
Figure 4-8. Angle of attack necessary to enter the Aerothermal curve (from 120 to 80 Km)
Figure 4-9. Nominal trajectory in Z-V plane
Figure 4-10. Nominal trajectory in Z -t plane
Figure 4-11. Angle of attack evolution along nominal trajectory
Figure 4-12. Lift coefficient evolution along nominal trajectory
Figure 4-13. Drag coefficient evolution along nominal trajectory
Figure 4-14. Flight path angle evolution along nominal trajectory
Figure 4-15. Velocity evolution along nominal trajectory
Figure 4-16. Mach number evolution along nominal trajectory
Figure 4-17. Radiative equilibrium stagnation point temperature evolution along nominal trajectory
Figure 4-18. Radiative equilibrium stagnation point heat flux evolution along nominal trajectory

Figure 4-19. Dynamic pressure evolution along nominal trajectory
Figure 4-20. Bank manoeuvre.
Figure 4-21. Crossrange versus downrange for different bank angle.
Figure 4-22. Re-entry trajectories for different constant bank angle.
Figure 4-23. Effect of the bank on the ground track.
Figure 4-24. Effect of the aerodynamic database on the ground track.
Figure 4-25. Trajectories comparison.
Figure 4-26. Acceleration and Stagnation point heat flux comparison.
Figure 4-27. Dynamic pressure comparison.

Figure 5-1. Nose Computational mesh
Figure 5-2. Convective Heat flux on the Bottom side AoA=0°. Local Radiative Equilibrium.
Figure 5-3. Convective Heat flux on the Top side AoA=0°. Local Radiative Equilibrium
Figure 5-4. Surface Temperature on the Bottom side, AoA=0°. Local Radiative Equilibrium.
Figure 5-6. Surface Temperature on the Top side, AoA=0°. Local Radiative Equilibrium.
Figure 5-7. Convective Heat flux on the Bottom side AoA=20°. Local Radiative Equilibrium.
Figure 5-8. Convective Heat flux on the Top side AoA=20°. Local Radiative Equilibrium
Figure 5-9. Surface Temperature on the Bottom side, AoA=20°. Local Radiative Equilibrium
Figura 5-10. Surface Temperature on the Top side, AoA=20°. Local Radiative Equilibrium.
Figure 5-11. Sections at 1cm, 10 cm and 50cm from leading edge.
Figure 5-12. Temperature comparison between preliminary and rounded nose geometry along the section at 1cm from leading edge for windside and leeside
Figure 5-13. Temperature comparison between preliminary and rounded nose geometry along the section at 10cm from leading edge for windside and leeside
Figure 5-14. Temperature comparison between preliminary and rounded nose geometry along the section at 50cm from leading edge for windside and leeside
Figure 5-15. Surface temperature on nose symmetry plane at 0 and 20° of the angle of attack.
Figure 5-16. Surface temperature on nose symmetry plane at 10° of the angle of attack.
Figure 5-17. Wing Computational mesh
Figure 5-18. Radiative equilibrium temperature at Z=60 Km and M=15
Figure 5-19. Radiative equilibrium temperature at two different sections along wing semi-span (y=0.8m and y=2.5)
Figure 5-20. Distribution of convective heat flux along a flat plate at different angle of attack for the conditions of maximum aeroheating along the Shuttle(red) and the proposed (blue) re-entry trajectory

Figure 5–21. Distribution of convective heat flux along a flat plate at 40°of angle of attack (red dashed line),an axis-symmetric sphere-cone (R=0.6m) nose (red solid line) for the conditions of maximum aeroheating of the Shuttle and axis-symmetric sphere-cone (R=0.01m) nose (blue solid line) for LERV trajectory
Figure 5-22. Laminar turbulent transition for Low Risk Trajectory at x/L=0.9 and x/L=0.1
Figure 5-23. Laminar turbulent transition for Shuttle Trajectory at x/L=0.9 and x/L=0.1
Figure 5-24. RV Temperature history on fuselage lower surface centreline at x/L=0.1 and at x/L=0.9.
Figure 5-25. Shuttle temperature history on fuselage lower surface centreline at x/L=0.1 and at x/L=0.9.
Figure 5-26. Laminar and turbulent wall temperature computations (Z=42Km; M=4)
Figura 5-27. Internal configuration of the nose (symmetry plane).The dimensions are in mm.
Figure 5-28. Surface temperature on the nose symmetry plane for local radiative condition at zero angle of attack(dashed line) and at1500s during re-entry (solid line)
Figure 5-29. Comparison of the preliminary and second configuration
Figure 5-30. Surface temperature of nose leading edges. Configurations comparison
Figure 5-31. Surface temperature of wing leading edges . Configurations comparison
Figure 5-32. Steady state surface temperature contours of nose leading edge in the symmetry plane with preliminary configuration.
Figure 5-33. Steady state surface temperature contours of nose leading edge in the symmetry plane with second configuration.
Figure 5-34. Steady state surface temperature contours of wing leading edge in the symmetry plane with preliminary configuration.
Figure 5-35. Steady state surface temperature contours of wing leading edge in the symmetry plane with 2nd configuration.
Figure 5-36. Temperature evolution on three control point in the symmetry plane of the nose.
Figure 5-37. Heat load evolution along the trajectory.
Figure 5-38. Surface temperature at 500s of the re-entry time.
Figure 5-39. Surface temperature at 1000s of the re-entry time.
Figure 5-40. Surface temperature at 1500s of the re-entry time.
Figure 5-41. Surface temperature in the symmetry plane at 500s of re-entry time.
Figure 5-42. Surface temperature in the symmetry plane at 1000s of re-entry time.
Figure 5-43. Surface temperature in the symmetry plane at 1500s of re-entry time.

Figure 5-44. Comparison between local and global radiative equilibrium temperature along the trajectory.
Figure 5-45. The design of leading edges assembly.
Figure 5-46. Fuselage TPS configuration.
Figure 5-47. Fuselage TPS layout.
Figure 5-48. Internal insulator scheme.

LIST OF TABLES

Table 2-1. Materials thermal properties

Table 2-2. Reference Missions

Table 3-1. Numerical codes comparison

Table 3-2. Computational matrix and corresponding aerodynamic coefficients

Table 3-3. Viscous effects on aerodynamic coefficients

Table 5-1. Recommended Mach number coefficients

Table 5-2. Material properties

CHAPTER 1

HYPERSONIC LIFTING FLIGHT: PAST, PRESENT AND FUTURE

1.1 Introduction

The Orbital Space Plane (OSP) goal was to have International Space Station (ISS) crew rescue capability by the year 2010 and crew transfer by 2012 relying on expendable launch vehicles both safer and less expensive to operate than the current space transportation system. In particular compared to the Space Shuttle, the system will require less time to prepare and execute a mission and less time and cost to refurbish after every mission.

This drove the OSP system toward crew escape capability during ascent, high control margins, and low entry and landing acceleration environments especially for critically ill or deconditioned ISS crew. All these requirements match quite well with the needs of flight quality for space tourism vehicle, too.

For the aerodynamicist and performance analyst this requires high stability and control margins, especially for a launch escape option, high hypersonic Lift-to-Drag ratio (L/D) for reduced entry g loads, and high subsonic L/D and landing lift coefficient (C_L). By a system analyst point of view a winged or lifting body implies more difficulties than a capsule configuration, in particular for as concern thermal management during re-entry and for the launch configurations. Moreover the experiences developed during the Moon race with the Apollo program are a so strong background to drive the NASA to repeat those experiences exploiting the improved technologies developed in the last forty years for the Crew Exploration Vehicle (CEV).

Because the subject of this study is a lifting vehicle and not a capsule, in the next paragraphs the past activities on lifting vehicles, that led to Space Shuttle development, are presented together with a glance on present and future planned activities.

1.2 The Past: A Historical Perspective on Hypersonic Flight Vehicle

The U.S. Mercury, Gemini and Apollo and the Soviet Vostok, Voskhod and Soyuz were capsules that re-entered the atmosphere ballistically. They had ablative heat shields and used parachutes to slow the final descent. This system worked fine. The Soyuz-type vehicle is still in use today, transporting cosmonauts to and from the International Space Station (ISS). Each spacecraft capsule, however, flew only once, and they required extensive ground and sea support for recovery.

Since 1960s, NASA and the U.S. Air Force tested a series of lifting vehicle designed to be spacecraft, not airplanes. They were designed to re-enter the atmosphere from orbit and fly at relatively low speeds just well enough to land safely without parachutes.

The ideal spacecraft would be able to maneuver from orbit to a chosen landing site. It would land like an airplane. Equally important, it would be reusable. Flying each craft more than once and eliminating the need for a naval task force recovery expedition on every flight would dramatically reduce the cost of space flight. The aerodynamics of such a craft would have to be fundamentally different from those of the ballistic capsule.

Figure 1-1. The X-15, first hypersonic plane

The X-15 was the first manned airplane to fly hypersonic. On its fastest flight, it achieved Mach 6.7 and returned with some pieces melted off. This flight showed that the thermal problems at the higher speeds of an orbital re-entry would be extremely difficult to solve with the available materials and technology of the time. The sharp leading edges of the wings get extremely hot. They have a lot of surface area to absorb heat but little material volume to act as a heat sink and conduct heat away from the surface. The hypersonic L/D of the X-15 was higher than needed for an acceptable spacecraft. L/D values of between 1 and 1.5 give enough cross-range for many missions. An additional goal was to have good enough subsonic flying qualities to allow the vehicle to land like an airplane.

To overcome the limit of the thermal protection materials of that time NASA and U.S. Air Force researchers began to look at combining the thermally effivcient blunt body with the ability to generate lift. These shapes could have acceptable cross-range and be protected by the same ablative heat shields as are used on the capsules.

Dr. Alfred Eggers at NASA's Ames Research Center concluded that if one side of a blunted cone were flattened, it would generate lift. Trailing flaps at the base could provide control. His configuration M1 was a half cone with a blunted nose. It had a hypersonic L/D of 0.5 and could produce a cross-range from orbit of 170 miles. The M1 evolved into the M2, which was a 13-degree half cone with a blunt nose. Hypersonic L/D was 1.4. The M2 was a step in the right direction, but subsonically, it still flew like a bowling ball. It was not capable of a gliding landing. To give it some low-speed glide, the Ames engineers modified the basic M2 by squeezing the back of the cone down like a tooth paste tube to form a chopped-off trailing edge. Twin fins were added for directional stability. The final M2 configuration also had a canopy.

Figure 1-2. The M2-F2, final configuration.

The U.S. Air Force was also looking at moderate L/D re-entry concepts. The Air Force had tried to develop a winged re-entry vehicle: the X-20 Dyna-Soar. Unfortunately, the Dyna-Soar did not survive in December of 1963, it joined the too-long list of technologically advanced projects canceled in the name of economy. Although the Dyna-Soar was dead, the Air Force continued work on hypersonic lifting configurations.

Figure 1-3. X-20 Dynasoar prototype configuration.

Starting in 1963, the ASSET program launched a series of small, unmanned test vehicles. The ASSET configuration was flat-bottomed and had a 70-degree, swept, blunt-leading-edge delta wing. The body was a modified cone almost as wide as the wing. ASSET tested the hypersonic part of the flight envelope. No attempt was made to land it like an airplane; the vehicles splashed down in the ocean under parachutes. The ASSET flights demonstrated lifting re-entry for the first time. One ASSET was recovered and can be seen at the Air Force Museum in Dayton, Ohio.

In 1964, Air Force project START (spacecraft technology and advanced re-entry test) to test the SV-5 configuration began. Phase 1 of START was Project PRIME (precision recovery including maneuvering entry). Subscale SV-5D vehicles were launched on Atlas boosters and flew hypersonic re-entries in 1966 and 1967. The PRIME SV-5D demonstrated a cross-range of over 710 nautical miles on the third flight It was recovered by parachute. It was in flyable condition and could have been re-launched after replacement of the ablative heat shield.

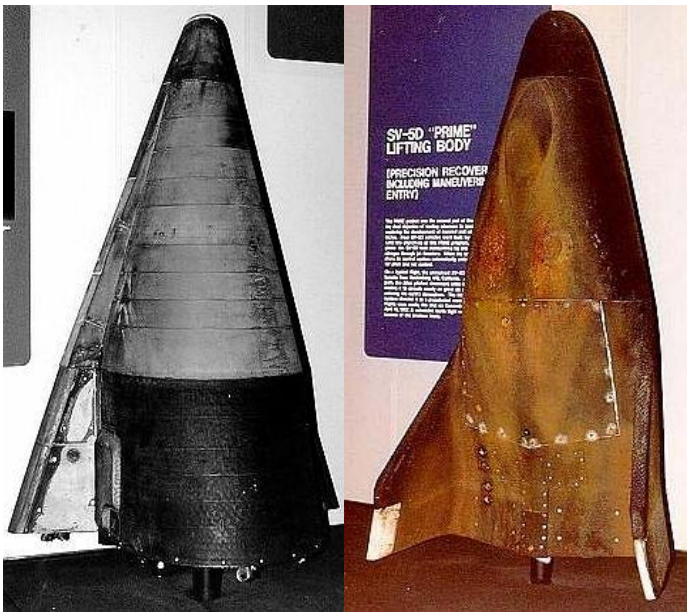

Figure 1-5. The ASSET and the PRIME.

Phase 2 of START was to build and fly a full-scale, manned vehicle to explore speeds from low supersonic down to landing. This machine, the SV-5P ("P" for "piloted") became the X-24A. Design features. The first-generation lifting-body configurations shared some design features. They all had blunt noses and highly swept delta planforms. The radius of the "leading edges," or body sides, was very large.

All had twin fins mounted at what would have been the wingtips if there had been wings. The M2 started with just two fins, while the HI,10 and the X-24A both had a third, centerline fin.

All had chopped-off back ends with large base areas. This caused a lot of drag, but it was necessary for transonic and supersonic stability. It also kept the trailing edges of the controls from being so thin that they would melt during re-entry. All of the vehicles had the ability to "flare" upper and lower flaps to give the back end of the vehicles a wedge shape.

The amount of wedge used was a compromise between drag and stability. At low speeds, the drag caused by the base area was undesirable, so the flaps were retracted to reduce drag. At transonic speeds, the fat shape of the lifting bodies caused problems. Air flowing aft from the thickest point on the body formed shock waves that moved around rapidly following small changes in Mach and angle of attack. This caused large, unpredictable pitching moments and made the vehicles unstable in pitch. Wedging the flaps open to give the machine a shape like a shuttlecock restored stability at a cost in drag.

Two of the vehicles could also generate wedge angle for directional stability. The X-24A rudders on the outboard fins were both toed out at high speed. The HL10 could split the trailing edges of all three fins to give them a wedge cross-section.

The lifting-body designs differed greatly in cross-section and camber. The M2 was a half-cone, pinched toothpaste-tube fashion at the rear. It was flat on top, and the canopy protruded above this flat deck. A nose window gave the pilot a little down/forward visibility for the landing.

The HL-10 had a more airfoiled shape with inverted camber. Viewed from the side, the bottom had a lot of rocker, like a surfboard, while the top was a nearly straight line. In transverse cross-section, the HL-10 was much flatter on the bottom and rounder on top than the M2. The HL-10 had no protruding canopy; windows were integrated into its basic shape.

The X-24A had positive camber. In side view, the top had more curvature than the bottom. Cross-sections were closer to those of the HL,10-sort of flat on the bottom and very round on top. The positive camber made it possible to put the canopy where the sides and nose all sloped down, away from the canopy base. This gave the X-24A the best pilot visibility of all the first-generation lifting bodies

The Air Force Flight Dynamics Lab developed a series of shapes designed to have higher hypersonic L/D (about 2.5) than the first lifting bodies. They were intended both for re-entry vehicles and hypersonic-cruise airplanes. After flight testing, the X-24A was returned to Martin. A glove was built around it that completely changed its shape to a configuration designated "FDL-8." This was a 78-degree, swept, flat-bottom shape with moderately rounded nose and edges. The sides were canted inward 30 degrees. Small delta strakes with ailerons were added outboard of the fins.

The new X-24B was delivered in fall 1972. It proved to be the best flier of all of the lifting bodies. The flat bottom and sloping sides combined with the outboard ailerons eliminated most of the undesirable yaw/roll coupling that had plagued earlier lifting bodies. Pilots compared its flying qualities favorably with those of contemporary fighters. The X-24B proved the soundness of the FDL-8 configuration. A ramjet-powered, hypersonic research aircraft, the X-24C was planned but died due to funding cuts. It was extensively analyzed and was once called "the most studied airplane never built."

Figure 1-6. X-24B in flight

The last two flights of the X-24B were important to the space shuttle. Pilots John Manke and Mike Love were convinced that the machine could be landed on a conventional concrete runway instead of the dry lakebed. On 5 August 1975, Manke made the first ever landing of a lifting body on a conventional runway. Fifteen days later, Love repeated the feat. Both landings were on the centerline and within 500 feet of the aim point. These flights paved the way for today's shuttle landings on the runway at the Kennedy Space Center.

Soviets also experimented with lifting bodies under "Project Spiral." MiG built a subsonic test vehicle-the Mig-105-11. It had two interesting features: the landing gear retracted into the upper body sides so that the heat shield would not be broken by landing-gear doors; the outboard flying surface had variable dihedral and could convert from fins to wings. During re-entry, they were tilted up like the outer fins on the American lifting bodies. For landing, they could be flattened out to act as wings. The Mig-105-11 flew successfully, and is now in the Monino museum.

Figure 1-7. Mig-105-11 in Monino Air Force museum

The Soviets also tested several sub-scale BOR-4 vehicles in a program similar to PRIME. A space interceptor called "Urgan," presumably designed to counter U.S. shuttles flying out of Vandenberg, was planned. The Urgan was never built due to the decline of the Soviet Union and the U.S. cancellation of the military use of the shuttle.

Figure 1-8. BOR-4S at MACS in Zhukovski (Sub-scale 1:2)

With the end of the X-24B project, the lifting-body concept appeared dead in the U.S. Early shuttle concepts were based on the HL-10, but a combination of factors drove the design to the deltawing orbiter of today. The cargo bay of the shuttle is large to accommodate big payloads. The decision to use an expendable external tank made internal volume less desirable. The final decision to make the shuttle a winged configuration was forced by the need for very high cross-range to be able to fly the projected Air Force missions from Vandenberg AFB into polar orbit and land safely. The development of the fragile, but effective, thermal-protection tiles made it possible to survive the higher re-entry leading-edge heating. Ironically, the shuffle never flew out of Vandenberg. After the Challenger accident, the Air Force returned to using expendable boosters. A lifting-body configuration would be quite capable of flying the trajectories used by the shuttle today.

Recently, two new lifting-body projects have emerged. The first was the Lockheed/NASA X-33. The X-33 was intended as a test craft for a fully reusable single-stage-to-orbit vehicle. All of its fuel internally, making the large volume of a lifting body highly desirable.

The second new lifting body was the X-38 test vehicle for the International Space Station. The X-38 was intended to be a space lifeboat, manned, but not piloted. In the event of an emergency, the station crew would cast off in the X-38, which would then re-enter and land automatically. The X-38 had to be developed by Scaled Composites in collaboration with ESA and European industries.

Instead of landing at 200-plus knots like earlier lifting bodies, it was foreseen a parafoil gliding parachute to come to a soft, low-speed landing. An X-38 test vehicle completed the first successful test of parafoil deployment and landing before to be cancelled.

Figure 1-8. Artistic view of theX-33 and the X-38 prototype flight test

1.3 The Actual International Programs and Objectives

The Orbital Space Plane (OSP) program was designed to support the International Space Station requirements for crew rescue, crew transport and contingency cargo such as supplies, food and other needed equipment. After the Space Shuttle Columbia disaster, NASA scrapped the OSP in favor of the Crew Exploration Vehicle, a Project Apollo-style capsule with separate crew and service modules. Initially hailed as a more flexible replacement for the Shuttle, NASA had envisioned the capabilities for crew rescue and crew transfer could result in different versions of the same Orbital Space Plane vehicle design. Since it was designed to support the International Space Station, the Orbital Space Plane was initially designed to serve as a crew rescue vehicle for the Station; this replaced the previous plans for a dedicated

station Crew Return Vehicle, which had been sidelined by budget cuts. This early version of the plane had been expected to enter service by 2010. The Orbital Space Plane was also designed to provide safe, affordable access to the International Space Station, as a replacement for the aging Shuttle. Top level requirements for the Orbital Space Plane and its related systems were approved in February 2003. In March 2003, the program began evaluating system operations to ensure the alignment of systems design between the NASA mission and the contractor design. The program was put on indefinite hold after the Columbia breakup, and was cancelled in favor of the CEV program. The CEV program emerged from the initial OSP proposals which had been based on four groups of concepts being considered for the physical design of the space plane itself - or the vehicle architecture: a capsule, a lifting body, a sharp body with wings and a blunt body with wings.

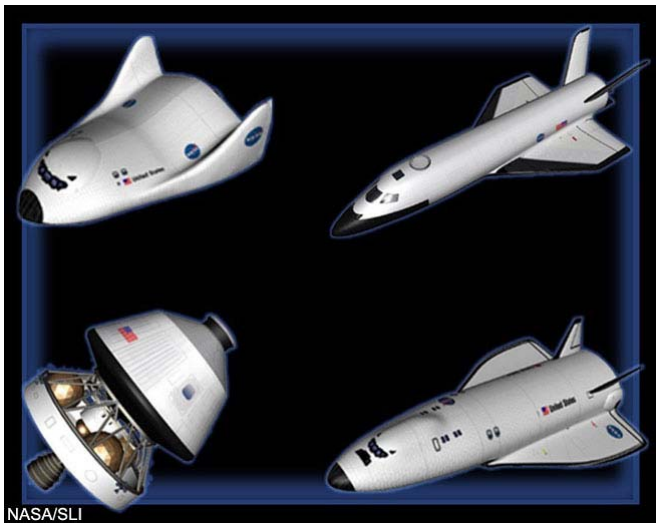

Figure 1-9. Four concepts for the Orbital Space Plane (OSP) design released by NASA

After the Columbia accident investigation, the capsule design with a separate escape system was considered the optimal design for crew safety.

By the russian side, the Clipper manned spacecraft replacement for Soyuz was first announced at a Moscow news conference on 17 February 2004. The 14.5 tons reusable lifting body would be used as a space station ferry and lifeboat, or could operate independently to shuttle tourists to space. RKK Energia had begun the work on the design in 2000, at the request of the Russian Space Agency. Energia had studied a unique new manned spacecraft concept envisioned for launch on the Angara or Zenit launch vehicles in the 1990's.

Figure 1-10. Clipper manned spacecraft (with SHM)

In the original design the Kliper was a "lifting body," a wingless iron-shaped fuselage, which would enable the craft to maneuver in the Earth atmosphere during the re-entry. However, by the end of 2004, engineers favored a stubby delta-winged re-entry vehicle, which would increase the cross range of the vehicle, while reducing g-loads on the crew.

In the frame of the Future Launch Preparatory Program the European Space Agency is developing an Intermediate eXperimental Vehicle (IXV) dedicated to validating re-entry technologies. Studies for this are already underway and the IXV is scheduled to make its first orbiting flight, launched by Vega, Europe's new small launcher, in 2010.

Figure 1-11. Artistic view of the IXV.

The aim is for the IXV to make a controlled Earth re-entry flight, aided by active aerodynamic control surfaces. IXV will be used to verify and investigate: advanced thermal protection systems and hot structures in-flight performance, key aerothermodynamics phenomena, innovative materials , structural health monitoring and guidance, navigation and control issues. The program continues to suffer from the multiplication of next-generation launcher and re-entry vehicles efforts in France, Germany and Italy.

In particular in Germany a flight demonstrator is being developed and built. This flight demonstrator, which was given the name PHOENIX, is a one-seventh scale model of the future space transport vehicle HOPPER. The vehicle particularly serves for acquiring real flight and landing attitude data that cannot be simulated. With a span of 3.90 m, wing and control surfaces of the PHOENIX flight demonstrator, an aluminum structure having a weight of about 1,000 kg, were kept as small as possible to minimize drag during automatic touchdown.

During the test flights, the PHOENIX proved its ability to detect and automatically correct track deviations on the ground. The braking system also underwent extensive testing. Phoenix was released at a distance of up to five metres from the centreline to see whether the system was able to automatically return to the centreline by applying the necessary track corrections using the nose wheel.

Figure 1-12. Phoenix on the runway

Onboard navigation computers calculated the track on the basis of position data provided by the GPS satellite system. The tests were also used to demonstrate the straight-run capability of Phoenix and to calibrate brake pressure. Under real conditions, the vehicle will touch down at a speed of 255 kilometres per hour. After landing, Phoenix will reduce speed by first applying the wing flaps and then the disk brakes of the main landing gear to retard to full stop. Acceleration of the prototype to about 150 kilometres per hour was the highlight of the taxis tests. This speed comes as close to real landing conditions as is possible in a ground test. In this case, too, Phoenix was able to precisely correct track deviations so that the distance from the centreline was just a few centimetres.

The USV (Unmanned Space Vehicles) Program is the Italian technological development program oriented toward future generations of reusable space vehicles, able to sustain frequent and repeated launches into space and atmospheric re-entries. Aiming to reach higher aerodynamic –efficient operational configurations than the Space Shuttle, the orbit re-entry

will be characterised by very high heat fluxes and thermal loads, requiring the development of new structural concepts (SHS, Sharp Hot Structure) based on innovative materials which are resistant to the highest temperatures. In order to control these parameters a broad knowledge of hypersonic aerodynamics, aerothermodynamics, materials engineering and space flight dynamics is necessary.

The 9.2-m. long USV-1 will be taken up via a high altitude balloon to 24-25-km and dropped. It will "glide for about 2 min., reach high transonic speeds and perform several maneuvers before opening its parachute for recovery and splash down". The 1,250kg vehicle is expected to reach Mach 2.5 during its descent.

Figure 1-13. USV FTB-1 and FTB-X.

There will be 4 drops by the end of 2007, with the high test drop at 35-40km. A second USV-1 is under construction. Also, a smaller (990kg, 5.2m long) USV-X vehicle is under development for a flight to orbit in the 2011 time frame. It will fly atop the Vega launcher into a low orbit and after a few hours re-enter to test its thermal protection systems.

1.4 Future Development

Two are the main objectives envisaged by the international agencies and private industries in the next or far future: Human exploration of the Moon and Mars and the development of commercial transportation for space tourism.

The Vision for Space Exploration calls for humans to return to the moon by the end of the next decade, paving the way for eventual journeys to Mars and beyond.

The U.S. president Bush announced the new course for America's space program in January 2004, saying it would give NASA a new focus and clear objectives for the future. "We do not know where this journey will end," said the President, "yet we know this: Human beings are

headed into the cosmos." After completing the International Space Station and retiring the shuttle fleet by 2010, the Vision calls for human and robotic explorers to work together on new journeys to worlds beyond. NASA's Constellation Program is already hard at work on the next generation of human spacecraft.

Aurora is the response of Europe to this challenging goals. It can be seen as a road map for manned exploration from where a large number of scientific as well as technology spin-offs will emerge. It should pave the way to placing a European on the surface of Mars by 2025. The objective of the Programme is to formulate first, and then implement, a European long term plan for the robotic and human exploration of the Solar System bodies which hold promise for traces of life. The Programme is multidisciplinary, crossing many sectors of science, technology and space activities.

Space tourism is the recent phenomenon of space travel by individuals for the purpose of personal pleasure. As of 2006, space tourism is only affordable to wealthy individuals and corporations, with the Russian space program providing transport.

Among the primary attractions of space tourism are the uniqueness of the experience, the thrill and awe of looking at Earth from space (described by astronauts as extremely intense and mind-boggling), the experience's notion as an exclusivist status symbol, and various advantages of weightlessness. The space tourism industry is being targeted by spaceports in numerous locations, including California, Oklahoma, New Mexico, Florida, Virginia, Alaska and Wisconsin, as well as Singapore and the United Arab Emirates.

In conjunction with the Federal Space Agency of the Russian Federation and Rocket and Space Corporation Energia, Space Adventures facilitated the flights for the world's first private space explorers: Dennis Tito, Mark Shuttleworth, Greg Olsen, Anousheh Ansari and the future missions of Daisuke Enomoto and Charles Simonyi. The first three participants paid in excess of $20 million (USD) each for their 10-day visit to the ISS.

The more affordable suborbital space tourism is viewed as a money-making proposition by several companies, including the European "Project Enterprise", Space Adventures, Virgin Galactic, Starchaser, Blue Origin, Armadillo Aerospace, XCOR Aerospace, Rocketplane Limited, and others. Most are proposing vehicles that make suborbital flights peaking at an altitude of 100-160 kilometres. Passengers would experience three to six minutes of weightlessness, a view of a twinkle-free star field, and a vista of the curved Earth below. Projected costs are expected to be in the range of $100,000-$200,000 per passenger, with costs dropping over time to $20,000 or less.

In December of 2005, the U.S. Government released a set of proposed rules for space tourism.

Under current US law, any company proposing to launch paying passengers from American soil on a suborbital rocket must receive a license from the Federal Aviation Administration's Office of Commercial Space Transportation (FAA/AST).
Constellation Services International (CSI) is working on a project to send manned spacecraft on commercial circumlunar missions. Their offer would include a week-long stay at the ISS, as well as a week-long trip around the Moon. They expect to be operational by 2008, according to their best case scenario. Space Adventures Ltd. have also announced that they are working on circumlunar missions, also possibly in 2008 or 2009.

1.5 Summary and Comments

Since 1960's lifting vehicle have been studied, designed and, in some cases, tested by Americans and by Russians in order to develop a "spaceplane" as early Space Shuttle was considered.
Today, after four decades of wide use of ballistic vehicles , those studies and results, achieved in the past, is keeping into account to substitute the Space Shuttle and to develop a new re-entry system more flexible and affordable.
Though the NASA, after a first choice on lifting vehicle, has turned to ballistic configurations, the ESA, European national space agencies and the Russian RKK is still exploring the possibility to develop a winged configuration for orbital missions and beyond.
All these research and development activities are also strongly encouraged by the even more industries interested in the space market for space transportation and space tourism in the next future.

Bibliography

"AURORA Proposal, Executive Summery", ESA/EXPLO-PP(2001)5 Paris, 7 November 2001

Becker, J. V., "The X-15 program in retrospect", Raumfahrtforschung Heft 2/69, pp. 45-53, 1969.

Belyakov, R A and Marmain, J, MiG-Fifty Years of Secret Aircraft Design, Airlife, England, 1994

Boyle, Alan. "Regulators OK Oklahoma spaceport - Suborbital test flights could begin in 2007, setting stage for tourists", *MSNBC*, 13 June 2006. http://www.msnbc.msn.com

Cook, S. A., “The Reusable Launch Vehicle Technology Program and the X-33 Advanced Technology Demonstrator”, 6th; AIAA Aerospace Plane and Hypersonics Technology Conference; Chattanooga, TN; United States, NASA-TM-111868, Apr. 04, 1995.

Encyclopedia Astronautica, “X-23 (SV-5D) Prime,”http://www.astronautix.com.

Gockel**,** W., “Reusable RLV Demonstrateur Vehicles - Phoenix Flight Test Results and Perspectives” IAC-04-V.6.04, 55th International Astronautical Congress, Vancouver, Canada, Oct. 4-8, 2004

Graf, E.D., The X-38 and Crew Return Vehicle Programmes, ESA bulletin 101, february 2000.

Hallion, R. P., The Path to the Space Shuttle:the Evolution of lifting re-entry technology. J. Brit. Interplanetary Soc. 36, pp. 523 -541, 1983.

Hallion, R. P., “ The hypersonic revolution: eight case studies in the history of hypersonic technology, vol. 1. Ohio, U.S.A. :USAF Aeronautical System Division, 1987.

NASA Headquarters Press Release, “NASA’s Integrated Space Transportation Plan Released, November 13, 2002. http://www.spaceref.com/news/viewpr.html?pid=9809

NASA Headquarters Press Release, ”Missions, Orbital Space Plane Program Level-One Requirements Mission Needs Statement” by Beth Beck, last updated February 18, 2003. http://www.nasa.gov/missions/current/MI_FM_osp.html

NASA Headquarters Press Release, ”NASA Selects Orion Crew Exploration Vehicle Prime Contractor” by Braukus M.,Dickey B., Humphries K.,last updated FAugust 31, 2006. http://www.nasa.gov/home/hqnews/2006/aug/HQ_06305_Orion_contract.html

"No more space for space as tickets sell out", *Yahoo! News*, 13 November 2006. Retrieved on 2006-11-13. http://news.yahoo.com/s/afp/20061113/lf_afp/russiaspacetourism

Pastena, M., Di Donato, M., Palma, D., Guidotti, G., Pellone, L., Rufolo, G. and Sabatano, R., “PRORA USV1: The First Italian Experimental Vehicle to the Aerospace Plane**”**, AIAA/CIRA 13th International Space Planes and Hypersonics Systems and Technologies Conference, Capua, Italy, May 16-20, 2005

Pesavento, Peter, Spaceflight, "Russian Space Shuttle Projects 1957-1994", 1995, Volume 37, page 226.

Powell, J. W., hengeveld, E., “Asset and Prime: gliding re-entry test vehicle”, J. Brit. Interplanetary Soc., 36, pp. 369-376, 1983.

Reed, R. Dale; Darlene Lister and J. D. Hunley. *Wingless Flight: The Lifting Body Story*. NASA History Series. NASA/SP 4220. Washington, D.C. 1997.

Siddiqi, Asif A, The Soviet Space Race With Apollo, University Press of Florida, 2003. (Originally published as the latter part of 'Challenge to Apollo' by NASA in 2000 as NASA SP-2000-4408).

The X-33 History Project Home Page, NASA Headquarters History Office, Updated April 11, 2001, Accessed March 31, 2003 http://www.hq.nasa.gov/office/pao/History/x-33/menu1.htm

USV FTB-X., http://www.cira.it/usv/ftbx.asp

Wong, Thomas J., Hermach, Charles A., Reller, John O. Jr., and Tinling, Bruce E., "Preliminary Studies of Manned Satellites—Wingless Configurations: Lifting Body," NACA Conference on High-Speed Aerodynamics: A Compilation of the Papers Presented, NASA/TM-X-67369, 1958, pp. 35–44.

CHAPTER 2

SYSTEM CONCEPT AND MISSION REQUIREMENTS

2.1 Introduction

The purpose of this chapter is to define the guideline for the development of the re-entry system. A reference mission will be identified to prove the feasibility of the re-entry strategies and methods for low Earth orbit (LEO) re-entry.
The mission and system requirements will be defined only to a level necessary to prove the concept feasibility. A basic vehicle parameters will be defined in order to drive the space craft design.

2.2 Atmospheric Entry

All space mission planning begins with a set of requirements it must meet to achieve mission objectives. The entry phase of a mission is no different. It must delicately balance three, often competing, requiring during atmospheric entry: deceleration heating, and accuracy.
A vehicle's structure and payload limit its maximum deceleration. Well conditioned humans can withstand a maximum deceleration of about 12 Earth g's for only a short time. For a deconditioned crew, this maximum is only 3.5-5 Earth g's. The maximum deceleration a vehicle experience during entry must be low enough to prevent damage or injury to the weakest part of the spacecraft , including the human crew. But entry designers must consider other issues. For example, too little deceleration can also cause serious problems. Like a rock skipping off a pond , a vehicle that does not slow down enough may literally bounce off the atmosphere and back into space.
Another limitation during entry is the heating, a result of friction between the speeding entry vehicle and the atmosphere. A crewed vehicle generates trillion of joules of heat that must be dissipated during the atmospheric re-entry. The trajectory and the vehicle must be designed to withstand these tremendous heat loads.
A third mission requirements is accuracy, as dictated by the spacecraft's capability for inertial navigation and the ground support resources available to guide the spacecraft to pa predetermined position in space relative to the target planet. This accuracy require control and knowledge to that position in space. To meet this constraint, it must again adjust the trajectory and vehicle design.
From all these constraints an entry vehicle must walk a tightrope between being squashed and skipping out, between fire and ice, and between hitting and missing the target. This

tightrope is a three dimensional entry corridor, shown conceptually in figure 2-1, through which an entering vehicle must pass to avoid skipping out or burning up. The size of the corridor depends on these competing constraints, deceleration, heating, and accuracy.

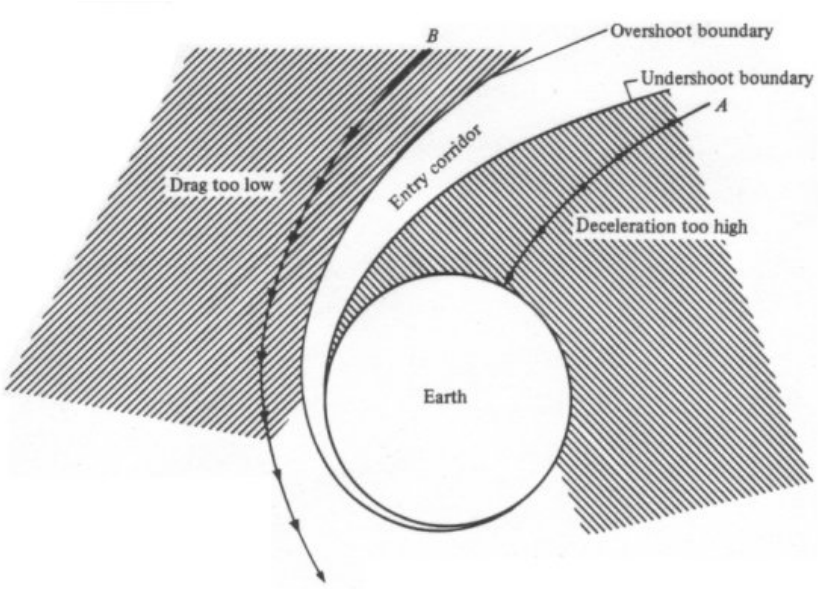

Figure 2-1. Entry corridor scheme.

Whereas these three constraints fix the entry corridor's size, the vehicle's control system determines its ability to steer trough the entry corridor.

Considering a vehicle, coming from LEO, which encounters the upper layer of the Earth atmosphere, three types of entry paths are possible:

1. *Ballistic entry*. The vehicle has little or no aerodynamic lift. It falls through the atmosphere under the influence of gravity and drag impacting the surface on a point depending only from conditions at the entry interface. The pilot has no control over his landing position during ballistic entry. This is the case of capsules as the Mercury, the Gemini and the actual Soyuz (Fig. 2-2a, red line). Platus (1982) gives an excellent summary of the state of the art in ballistic entry analysis.

2. *Skip entry*. The vehicle has a certain lift to drag ratio (L/D) and uses this lifting ability to first graze the atmosphere, then slow a bit, then pitch up such that the lift carries it back out of the atmosphere. This is repeated several time until the vehicle is slowed down appropriately and penetrates the atmosphere and landing. This entry mode has been used

partially by the Apollo capsules which exploited their little lift control for a single jump in the atmosphere (Fig. 2-2b).[Graves & Harpold, 1970]

3. *Glide entry.* The vehicle is essentially an airplane, generating a large L/D ratio. The vehicle enters the atmosphere at high angle of attack (25° or more), flies to the surface, and land on a runway. The advantages of such vehicles, as the Space Shuttle, are that the pilot can, in principle, choose the landing site and the vehicle can be landed safe to be used again. (Fig. 2-2a, blue line).[Eggers et al.,1957]

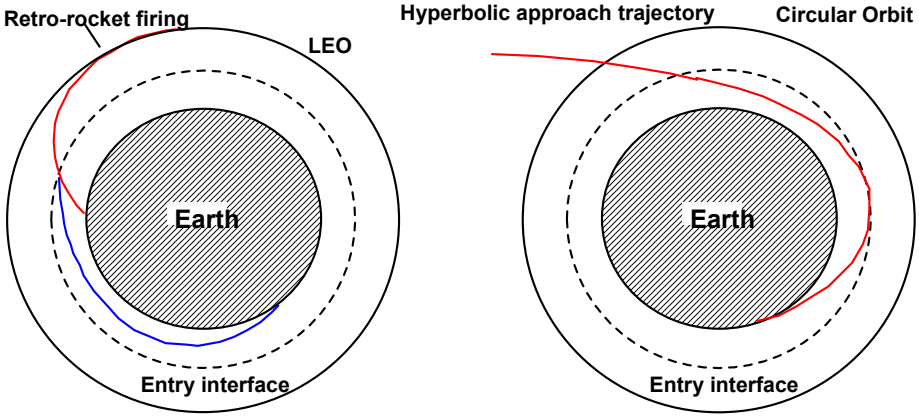

Figure 2-2. Re-entry trajectories.(a) orbital re-entry; (B) Apollo re-entry.

The choice of one of these re-entry strategies implies the choice of a type of vehicle configuration that can be characterized by two entry performance parameters: the lift to drag ratio(L/D) and the wing loading (m/S) (or the ballistic coefficient, m/C_DS).

By means of these two parameters it is possible to compare the vehicles performances even though the vehicles have dramatically different masses, references area and aerodynamic characteristics.

2.3 System concept approach

As initially proposed by Monti [Monti 2003; Monti et al., 2004] this study starts from the basic idea of avoiding an abrupt dissipation of the kinetic energy as happens during the capsules ballistic re-entry and ,in such a way, during the Space Shuttle descent. [Arringhton and Jones, 1983] On the contrary here is proposed a new strategy of re-entry based on the gradually conversion of kinetic energy in thermal energy.

To appreciate the difference in the aero-thermal behaviour of the proposed trajectory with respect to the traditional blunt body (capsule or Shuttle like) trajectories let us plot the kinetic energy conversion rate per unit mass ($\dot{e}$) during the deceleration phase:

$$\dot{e} = \frac{1}{M}\frac{dE}{dt} = \frac{d}{dt}\left(\frac{V^2}{2}\right) = V\frac{dV}{dt}$$

For the two different re-entry trajectories, starting from the re-entry interface (i.e. t=0; Z_0=120Km; V=V_0) to landing (at t=t_f; $V_f \approx 0$) the time integral of $\dot{e}$, represented by the area beneath the two curves, is:

$$\int_0^{t_f} \dot{e}\, dt \cong \frac{V_0^2}{2}$$

and is equal for both the trajectories cases (Fig. 2-3).

Figure 2-3 shows as the Shuttle re-entry is characterized by a strong deceleration in a short time, that implies a value of kinetic energy dissipation rate into thermal energy of the body (and of the surrounding air) higher than in the proposed re-entry strategy.

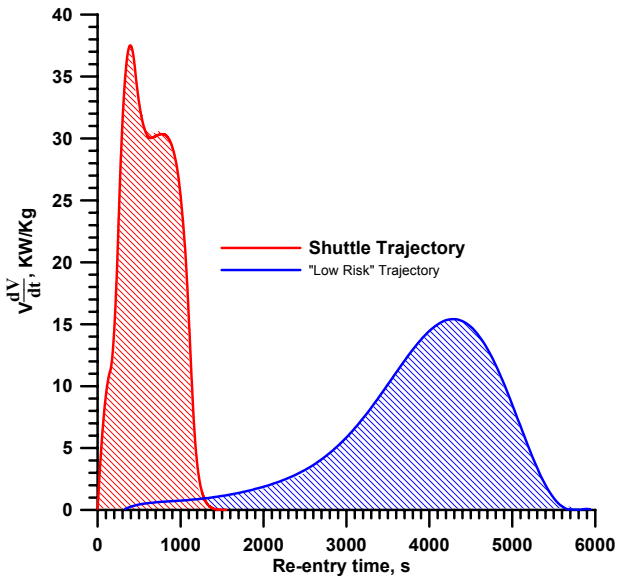

Figure 2-3. Energy dissipation rates for Shuttle and the proposed vehicle

The thermal load, i.e. the time integral of the convective heat flux at the body surface, is a fraction of the total converted energy and strongly depends on the body shape and on the surface point location. The fact that the heat flux will be kept almost constant and that the

maximum value of $\sqrt{\rho}V^3$ is smaller for the low risk trajectory allows the use of sharp edge bodies with a small radius of curvature at the nose or at the wing tips.

The ratio between

$$\dot{Q}_c = \int_S \dot{q}_c(t)dS$$

and

$$MV\frac{dV}{dt} = \frac{1}{2}C_D\rho V^3 S$$

represents the fraction of the entire kinetic energy converted into thermal energy convectively entering the body: one would like therefore to keep this fraction as small as possible.

This ratio depends on the vehicle shape and trajectory. If radiation is being considered, the use of materials (that can withstand high temperatures) allows that a radiative thermal equilibrium be achieved so that all the heat that is convectively transferred from the air to the body surface could be radiated back into space [Arnold et al., 2001]. The new way of thermally protecting the vehicle's structural material is made possible by the surface distributions of the convective heat flux that very strongly decreases downstream from the sharp leading edge.

Figure 2-4 shows the logical consequences of such choices.

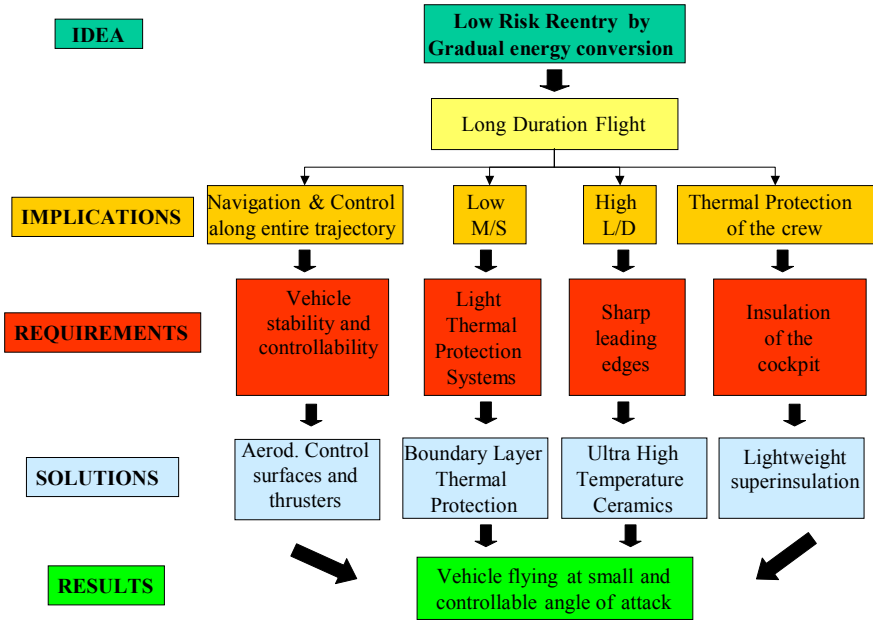

Figure 2-4. Implications and consequences of a low risk re-entry trajectory

This gradual conversion can be implemented by low deceleration in the upper layers of the atmosphere and consequently by a longer duration flight (more than one hour), compared with the conventional re-entries (of about 20 minutes). As a consequence, the kinetic energy rate dissipated as heat flux and the dynamic pressure levels, reached during the most severe aero-thermal conditions, are drastically lower.

In order to flight for a long time at high altitude the vehicle must be characterized by high aerodynamic efficiency and low wing loading and it must be able to control the vehicle through the entire trajectory and to protect the crew for the long time of re-entry. To do that it needs of good stability and controllability by means efficient aerodynamic control surfaces and thrusters and it makes use of a state of the art technology for the insulation of the cockpit with very light refractory materials.

The main points of the concept are, however, a strong reduction of the Thermal Protection System weight exploiting the Boundary Layer Thermal Protection System [Monti et al., 2003] approach allowing the use of Ultra High Temperature Ceramics (UHTC) [Rasky, 1992] only for the sharp leading edges, still maintaining in hypersonic flight an aerodynamic configuration resulting in a high aerodynamic efficiency.

These unconventional solutions represent a new way of protecting the structural material by positioning it at a location where the thermal boundary layer is sufficiently thick. The high heat flux takes place in the neighborhood of the stagnation point where the UHTC are located and where very high radiative equilibrium temperatures are attained.

One of the main advantage of this strategy is the long glide phase that provides operational advantages like increased cross-range linked to much more flexibility with regard to possible landing sites as well as drastically increased number of opportunities for re-entry (larger re-entry window).

The Shuttle risk is best witnessed by a single figure: 23.000 tiles for the thermal protection system! The required craftsmanship of the gluing process, the inspections of all the tiles make the refurbishment expensive and of high complexity that, by definition, contradicts safety. Dealing with a large number of TPS tiles, each one of which could be responsible for a catastrophic event, provides the evidence of an inherent low safety.

A clean structure of the re-entering vehicle with TPS localized only at the fuselage and wings tip, the low dynamic pressure encountered during the aerothermal critical phases of the flight and the even smaller pressure forces exerted over the vehicle surfaces (due to low angle of inclination of the shock wave) are all in favour of safety. These considerations lead to a clean and light structure that contributes to an inherent safety of the low risk re-entry vehicle.

Large values of down and cross ranges, together with the possibility of landing at very low speeds (of the order of 150 Km/h) in any airport tend to reduce the risk also during the super/subsonic phases of the flight, other than during the hypersonic regime.

With regard to re-entry guidance, or GN&C system must be available to force the trajectory within the entry corridor. For example the aerodynamic coefficients (i.e. the angle of attack α) must be modulated make the vehicle to fly along the aeroheating limit.

The basic concept adopted is completely different to that used by Space Shuttle [Harpold and Graves, 1979] and which was also proposed for the European Hermes [Jaensch &.Markl, 1991] vehicle and for the X-33 vehicle [Hanson et al., 1998].

Starting at the atmospheric entry interface (120 Km), with the shallow entry angle γ_e the vehicle exhibits a negative angle of attack to avoid the skip beyond the Earth atmosphere.

Hence in order to start decelerating the vehicle at the highest altitudes the spacecraft angle of attack initially increases up to $\alpha \cong 25°$, which is the maximum allowable angle for a convenient boundary layer thermal protection. This value is kept constant until the lift force becomes so large that the vehicle would tend to skip. At that moment α is gradually reduced in order to fly at the maximum constant convective heat flux. Once the vehicle reduces its velocity to value corresponding to low heat fluxes bearable by structural material it can fly without thermal constraint to the Terminal Area Energy Management [Moore, 1991] to approach the desired landing sites.

2.4 The Boundary Layer Thermal Protection System

Assuming that an axis-symmetric cone-sphere vehicle flies at hypersonic speed during re-entry at zero angle of attack and let us compute the heat flux over the body surface corresponding to a nose tip of a certain radius of curvature R. In vehicle design the behaviour of the temperature at leading edges is of particular interest, because at the stagnation point the boundary layer is very thin and the leading edge curvature governs the wave drag and the maximum heat flux. Rearranging the Tauber formula [Tauber, 1989] and considering the radiative equilibrium hypothesis for a spherical or cylindrical nose:

$$\dot{q}_{sp} = \sigma \varepsilon T_{sp}^4 = \frac{K(T_r - T_{sp})}{\sqrt{2^n R}} \cos\varphi$$

where T_{sp} is the stagnation point temperature, K is a constant depending on the gas, n is 0 for a spherical nose and 1 for a cylindrical nose, φ is the swept angle (zero for a spherical nose and for unswept wing), σ is the Stefan-Boltzmann constant, and ε the surface emissivity; if $T_{sp}<<T_r$ (T_r is the recovery temperature) one finds the following general trends:

spherical nose	$T_{sp}^4 \propto \frac{1}{\sqrt{R}}$
cylindrical leading edge	$T_{sp}^4 \propto \frac{1}{\sqrt{2R}}$
swept cylinder	$T_{sp}^4 \propto \frac{\cos\varphi}{\sqrt{2R}}$

In this way it is possible to evaluate the leading edge temperature and therefore to design the nose or wings leading edge radius of the vehicle on the basis of the maximum temperature allowable by the TPS material.

A simple thermal boundary layer analysis for a radiation cooled wall in hypersonic flow, based on the local equilibrium between convective and radiative heat fluxes, shows that for a flat plate at zero angle of attack and for perfect gas:

$$\frac{\delta_T}{x} \propto \frac{1}{Pe_x^{1/2}}; \quad T_{wr}^4 \propto \frac{1}{\sigma\varepsilon}\frac{(T_r - T_{wr})}{\delta_T}$$

where δ_T is the thermal boundary layer thickness, x the distance from stagnation point, and Pe_x is the local Peclet number ($Pe_x = Re_x Pr$). If $T_{wr} << T_r$:

$$T_{wr}^4 \propto \frac{1}{\sigma\varepsilon}\frac{Pe_L^{1/2}}{\left(\frac{x}{L}\right)^{1/2}}\frac{T_r}{L}$$

where L is the length of the flat plate. This equation shows that the fourth power of the radiative-adiabatic wall temperature (in laminar flow):

1) is inversely proportional to the characteristic boundary-layer thickness;
2) is proportional to the recovery temperature(T_r);
3) decreases with increasing distance from the nose tip as $x^{-1/2}$.

Therefore it is possible to estimate the distance (x) from the stagnation point at which the temperature is low enough so that we can employ a structural material and then it is possible to identify the UHTC tip insert length.

Two-dimensional geometries at angles of attack show a different $\dot{q}(x)$ distribution on the windside and on the leeside as illustrated in fig. 2-5. This figure shows the main idea behind the BLTP: only the front part of the sharp body exceeds high temperature and needs UHTC materials; the rest of the body can be made of structural materials (hot structure). Needless to say that the expected mass of the BLTPS is dramatically less than the conventional systems (Shuttle like) because it is limited to the very front tips. Sharp bodies tend to behave as blunt bodies at high angles of attack by exposing more and more of the wind side surface to high heat flux (as it is for the Shuttle).

The result of this observation is that the Boundary Layer Thermal Protection (BLTP) concept does not apply if the angle of attack (α) exceeds some limits.

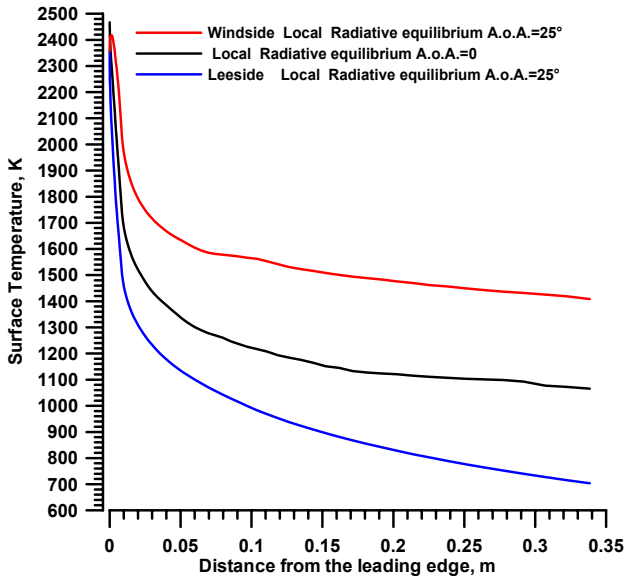

Figure 2-5. Local radiative equilibrium temperature on a 2-D body at zero and 25° of the angle of attack (M_∞=14.8; Z=60Km).

Figure 2-5 shows how a large angle of attack (say above 25°) implies that most of the windside structure is exposed to high heat fluxes and consequently it achieves high temperatures and would therefore survive only if one uses conventional TPS. In conclusion UHTC materials resist at very high temperature and allow for small radius of curvature and light protection systems. The only strong constraint, as we will be discussed later is to fly at a small angle of attack.

Examination of fig.2-5 identifies two problems posed by the new concept of the TPS:

1. Use of a material that can withstand stagnation point temperature;
2. A nose tip insert able to protect the rest of the structure without the need of tile (or blanket) type TPS.

A number of study cases has being selected to provide the evidence of the role played by :

1. the extension of the UHTC insert at the leading edge /nose tip;
2. the thermal conductivity of the UHTC materials;
3. the angle of attack.

All the computations have been performed for sphere-cone and cylinder-wedge geometries. Both the cone and wedge curvature radius is 1 cm and the half angle is 12.5°; these geometries simulate a sharp nose for the new vehicle concept. The radius of curvature of the cone has been chosen by a trade off between stagnation point temperature (a lower radius implies high stagnation temperature close to the limit of the TPS) and by the reduction of the drag of the vehicle and of its weight (large radius increase the wave drag and increase the TPS weight).

The internal configurations (fig. 2-6) consist of different length massive noses (or leading edges) and different thickness walls. The total length is 40 cm. The chosen size of UHTC tip is driven by the weight , the stagnation point temperature and by the maximum temperature achievable by (at the end of UHTC tip) the hot structure material.

Table 2-1 shows the physical properties of the materials under investigations at room temperature (ZrB_2, SiC and Inconel-617). Materials thermal properties were assumed constant. Systematic computations did not show large difference if assuming temperature dependent properties (according to the NASA TPSX Materials Database).

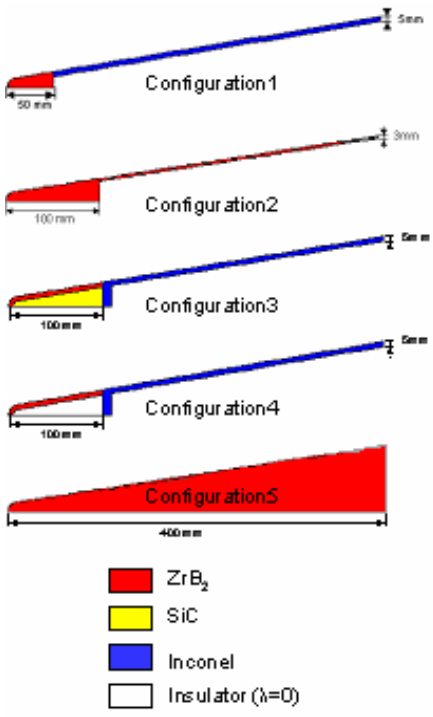

Figure 2-6. Geometry and configurations of the sphere-cone.

Table 2-1. Materials thermal properties

Material	Density, ρ Kg/m^3	Specific heat, c_p J/Kg K	Thermal conductivity, λ_s W/m K
ZrB_2	6000	628	66
SiC	3210	660	60
Inconel-617	8300	400	15

The selected point for the computations is Z=60Km and M_∞=14.8.

For all the cases considering the coupling between aero-thermal field and thermal field of the solid, the simple assumption of perfect gas has been assumed to speed up the computation, justified by the fact that for a sharp leading edge and for the considered flight conditions the flow is almost chemically frozen in the shock layer [Monti et al., 2005].

2.4.1 The effect of thermal conductivity: comparison between local and global radiative equilibrium

At the selected orbital re-entry conditions, convective heat transfer to the surface is partly conducted to the solid and partly re-radiated into the atmosphere. When a steady state is achieved, global radiative equilibrium is established, in the sense that the (surface) overall convective heat flux is perfectly balanced by the overall surface radiative flux. When conduction in the solid may be neglected (i.e. TPS materials with very low thermal conductivity), local equilibrium is established between radiative and convective heat transfer. The corresponding surface temperature will be referred to as "local"(for λ_s=0) and "global"(for $\lambda_s \neq 0$) "radiative equilibrium temperature", respectively. TPS realized so far are characterized by refractory low conductivity materials, acting as thermal insulators in order to cover and protect the metallic structure; the heat flux is alleviated making use of blunt configurations. The proposed new scenario for re-entry vehicles introduce sharp geometries that are subjected to much higher heat fluxes and temperatures that conventional TPS materials would not sustain.

Figures 2-7, 2-8 show the temperature distributions and contours for different axis-symmetric configurations. In each case the local radiative equilibrium temperature distributions are reported for comparison. The effect of high thermal conductivity of the UHTC is a strong

decrease of the maximum tip temperature and an increase of the temperature downstream of the stagnation point (i.e. the maximum temperature of the structural material) respect to the local radiative equilibrium condition.

We note (fig. 2-7) that increasing the bulk nose length from 50 to 100 mm (Configurations 1 and 2) the stagnation point temperature decreases, as well as the structural materials interface temperature. If we assume that structural materials cannot stand temperature higher than 1500K then we must select configuration 2(with 10cm of UHTC insert).

There are no substantial differences between configurations 3 and 4(fig. 2-8), corresponding to the same geometry and to the same external ZrB_2 shell but different materials for the nose insert.

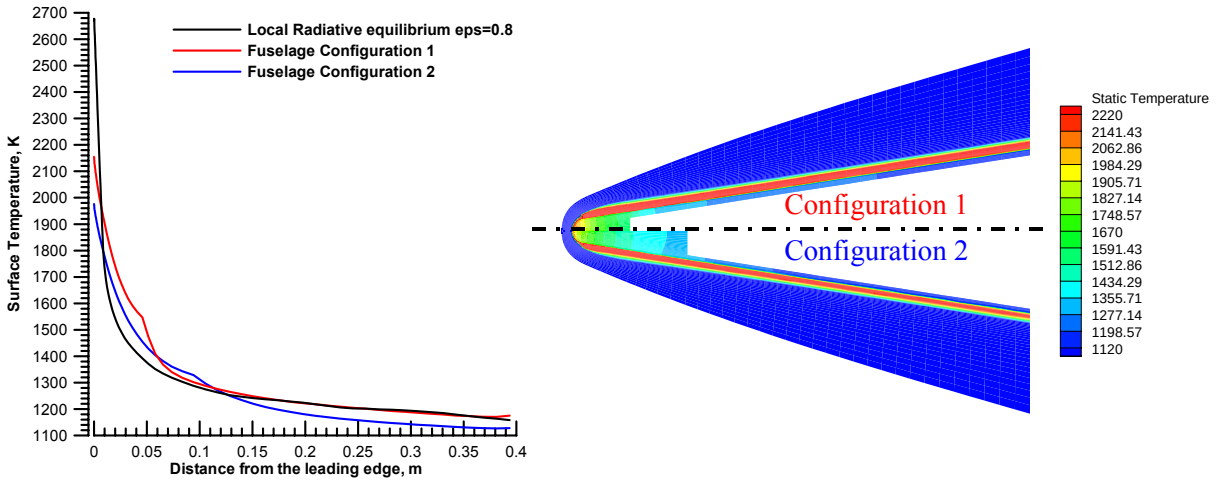

Figure 2-7. Effect of the ZrB_2 nose insert length. Configurations 1 and 2 (axis-symmetric).

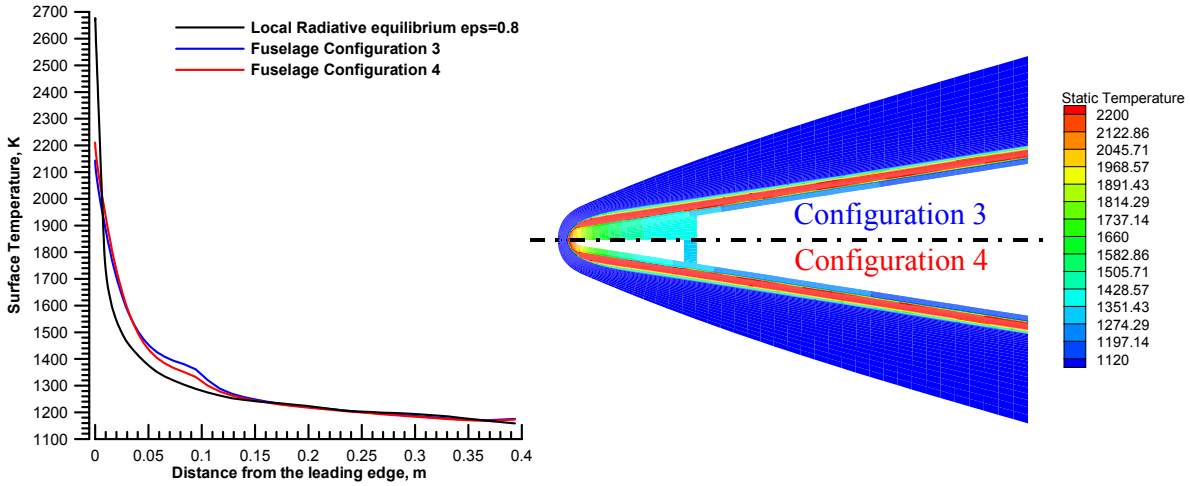

Figure 2-8. Effect of a SiC insert. Configurations 3 and 4 (axis-symmetric)

The assumption of local radiative equilibrium (LRE) wall over-estimates the stagnation point temperature and under-estimates the surface temperature distribution downstream from the leading edge. This effect is larger when TPS materials are characterized by high thermal conductivity.

2.4.2 The role of the angle of attack

As mentioned previously to ensure the efficiency of the BLTPS new generation re-entry vehicles need to fly at a low angle of attack to avoid exposing the windside metallic structure of the vehicle to high heat fluxes. On the other hand, during re-entry an appropriate angle of attack is necessary to ensure a sufficient C_L to sustain the vehicle.

In other words, the BLTP benefit obtained at zero angle of attack must be checked at different angles of attack. To investigate this effect a number of numerical simulations with different angles of attack have been performed.

Polar plots have been prepared that show at four different locations (fig. 2-9) on the fuselage the value of the heat flux and of the surface temperature on different meridian planes (configuration 5).

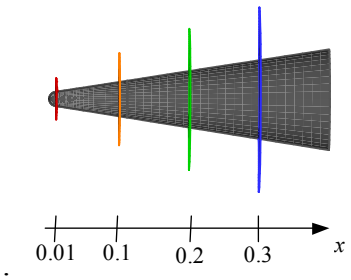

Figure 2-9. Locations of the four stations.

The first plot (fig. 2-10) shows the local convective heat fluxes at steady state (i.e. global radiative equilibrium conditions) for an angle of attack of 15° and an axis-symmetric configuration. On the windside the convective heat flux, is almost double that on the leeside. When flying at an angle of attack the windside is exposed to higher heat fluxes than the leeside and therefore “heat” will flow conductively across the fuselage between windside and leeside, levelling the temperatures and improving the thermal conditions of the TPS on the windside.

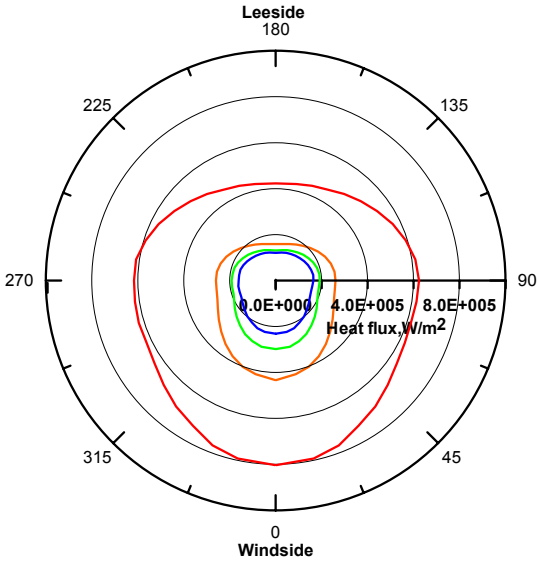

Figure 2-10. Convective heat flux at different station along the body at an angle of attack of 15° axis-symmetric body.

Figure 2-11 shows the skin temperature distribution along the azimuth angle at the same locations considered in Fig. 8 at the global radiative equilibrium condition. Radial distance measures the skin temperature: larger circles are relative to stations near the stagnation point (x=0.01;0,1 m), concentric circles(dashed) refer to zero angle of attack.

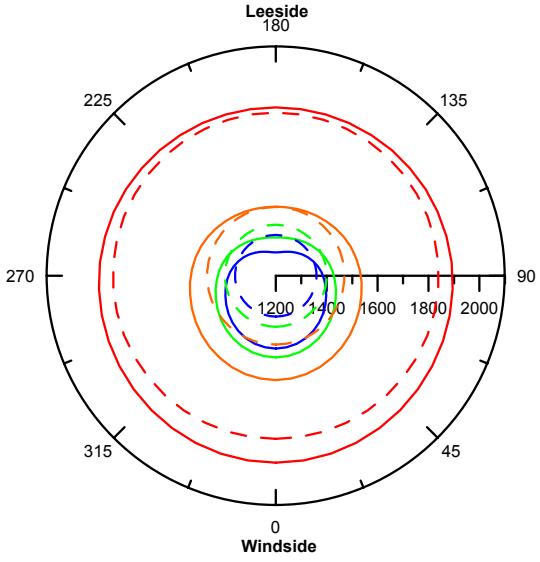

Figure 2-11. Temperature at different station along the body at zero angle of attack (dashed perfect circles) and at an angle of attack of 15°(solid curves)axis-symmetric body.

Figure 2-12 shows the local heat fluxes at steady state (i.e. global radiative equilibrium conditions) for an angle of 15° and an axis-symmetric configuration.

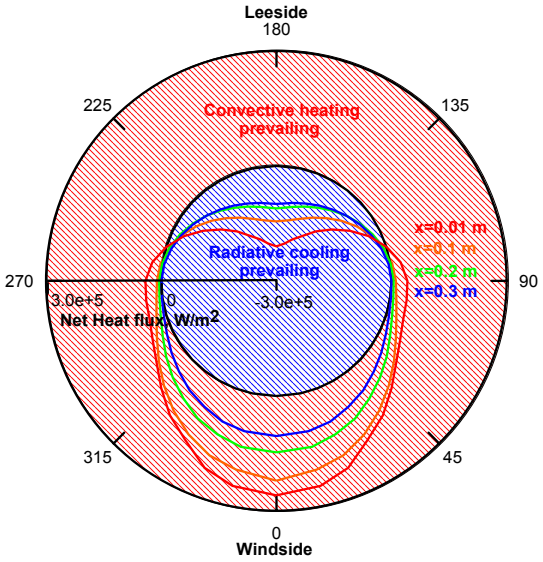

Figure 2-12. Surface heat flux at different station along the nose-cone body at an angle of attack of 15° (axis-symmetric body).

The different profiles of surface heat flux (once the global radiation equilibrium has been reached) show that on the windside the convective heat flux is larger than the radiative one and, vice versa on the leeside.

The radial distance from the (black) inner circle measures the net heat flux entering the structure i.e. convective minus radiative. The inner circle corresponds to a perfect balance of the two fluxes (net heat flux equal to zero), i.e. to local radiation equilibrium that would prevail if the thermal conductivity of the body skin is zero(λ_s=0).

The largest values correspond to stations close to the tip for which a large difference from the windside and leeside exists in heat flux and the relatively large thermal conductivity tends to level the temperatures at the sides(upper and lower) and at the front and back part. Both the axisal and radial heat flux are responsible for the unbalance of the overall heat flux at each station.

Figures 2-13 shows that the temperatures in the TPS zone do not change drastically up to 10° with configuration 3. Increasing angle of attack up to 25° not only increases the temperature on the windside increase(as we would expect) but also on the leeside.

These increases could be expected considering the high conductivity of TPS which drives the heat from the hotter windside to the colder leeside until global radiative equilibrium is reached. For a sphere-cone geometry at 10 cm downstream of the nose tip, and for an angle of attack larger than 10° the temperature at the interface between TPS and structural material grows up to values that cannot be sustainable by any conventional structural material. This is explained by the heat flux from the ZrB_2 nose tip to the metallic structure across the interface

and also by the lower thermal conductivity of the metallic structure that reduces the heat transfer from the hotter windside to the colder leeside

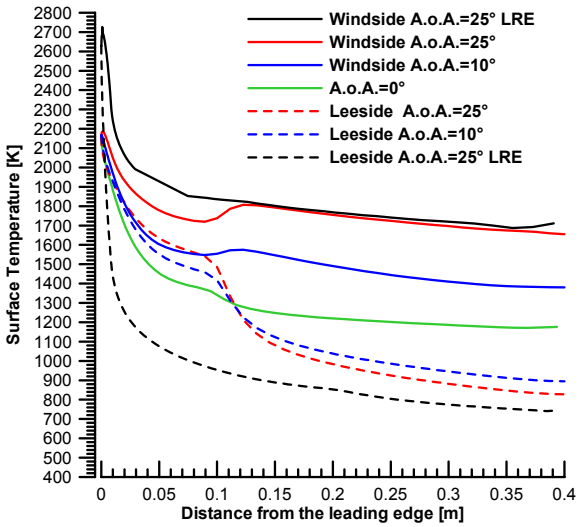

Figure 2-23. Global radiative surface temperature for a fuselage at different angle of attack (3-D).

Metallic structures at the state of the art cannot withstand, without TPS, temperatures higher than 1500 K (ODS alloys). Therefore during re-entry, for the considered configuration, the angle of attack cannot exceed 10°. This is another constraint for low risk re-entry trajectory for which it is necessary to monitor not only the stagnation point temperature but also the temperature of the structural material at the junction between the UHTC nose tip and the metallic structure.

Conditions can substantially improve on a half cone with a bottom flat surface (typical of fuselage tips) because the belly exposure is reduced by an angle of 12.5°. We would then expect roughly a situation for the windside corresponding to an inclination of α minus 12.5°. The windside surface temperature at 25° of angle of attack will therefore be close to that at 10° as shown in figure 2-13.

2.4.3 The role of chemical non equilibrium and surface catalysis

All the numerical simulations presented before have been performed considering a perfect gas model. For parametric analyses this results in a considerable reduction of computer time, in particular when the thermal coupling between fluid and solid is taken into account. In general during a re-entry mission the real gas behaviour must be considered since a large

amount of kinetic energy of the hypersonic free-stream is converted into thermal energy across the shock wave, hence resulting in very high temperature near the nose and in the boundary layer where chemical reactions occur. Considering a sharp body, the chemical reactions take place only in a thin shock layer that surrounds the sharp leading edge, therefore only in this zone we can expect differences between catalytic and non catalytic walls. Furthermore the oblique shock wave corresponding to the slender nose is much weaker than the normal shock. Considering this thin shock layer and the high flow velocity, the residence time between the shock and the body is smaller than the characteristic time necessary for the species to chemically react and to arrive at equilibrium.

To evidence the differences between the two models of ideal perfect gas and reacting mixture, numerical computations at the same flight condition (M_∞=14.8; Z=60Km) and with the local radiative equilibrium condition (λ_s=0) have been carried out considering an axis-symmetric body at different angles of attack. The results of the simulations are summarized in figures 2-14 and 2-15. For the axis-symmetric configuration (i.e. fuselage nose-tip) negligible differences can be appreciated between real gas and ideal gas, both at zero and at relatively high angles of attack.

The differences between the case of fully catalytic wall and non catalytic wall are also very small, when compared to the case of blunt bodies, where peak values of the heat fluxes may vary by more than 100% at the same flow conditions [Monti et al., 2005].

Similar results have been found at other positions along the trajectory. They all point out at the different importance of the catalytic effect in free-flight for blunt(and high angle of attack) compared to sharp (and low angle of attack). In this last case the gas almost does not dissociate for two reasons:

1. the weak oblique shock wave induces a temperature jump much smaller of that behind a normal shock wave(and therefore no large dissociation is to be expected close to the wall).
2. The distance along the streamlines(from the entrance into the shock to the wall) is much larger for the blunt body so that the air has time to reach almost chemical equilibrium conditions (and large dissociations)

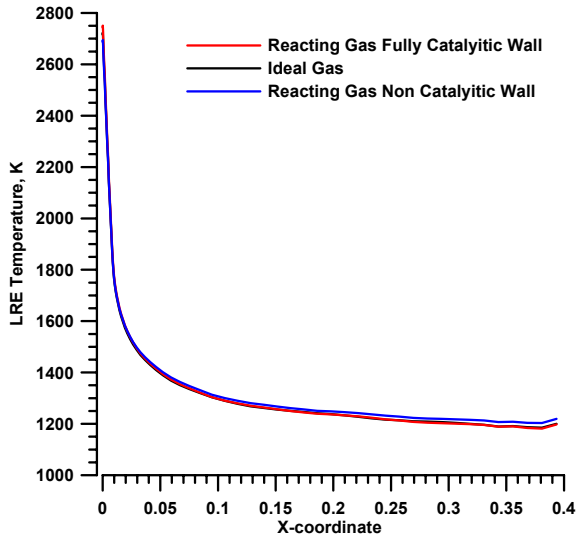

Figure 2-14. Temperature distributions on axis-symmetric body at zero angle of attack.

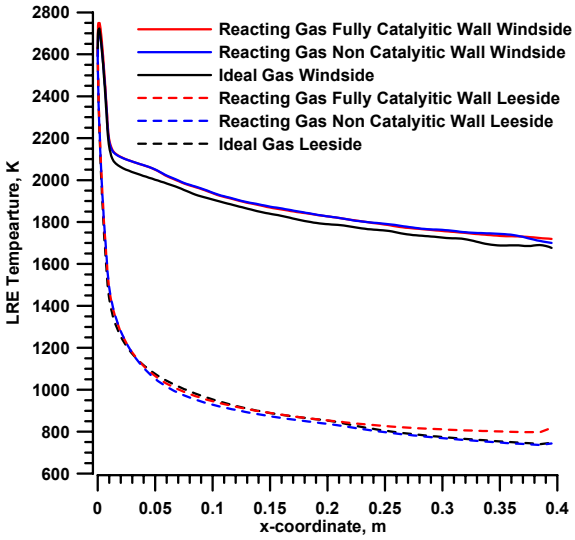

Figure 2-15. Temperature distributions on axis-symmetric body at 25°of angle of attack.

2.5 Main Vehicle Constraint

The re-entry strategy dictates the main vehicle requirements for the re-entry missions in terms of aerodynamic performance and aeroheating loads. To be compliant with the selected strategy the vehicle must fly in a re-entry corridor that ensures the necessary lift force and that, at the same time, does not exceed the maximum tolerable structure temperature, for instance at the stagnation point.

For LEO re-entry a very sharp leading edges (R_N=1.5cm) can be considered for the nose and the wings. A maximum stagnation point heat fluxes must be lower than 2 MW/m^2 corresponding to a radiative equilibrium temperature of about 2500K. Such temperatures can

be tolerate by the innovative Ultra High Temperature Materials (UHTC), that have been identified for leading edges. To reduce the aerothermal load a low wing loading (m/S) of the order of 80 kg/m^2 is necessary to flight at high altitude without diving deeply into the atmosphere.

In particular a parametrical analysis has been carried out to determine the effect of the wing loading on the re-entry trajectory and on the stagnation point heat flux for a LEO re-entry. The considered wing loading are 60, 80 and 100 Kg/m^2.

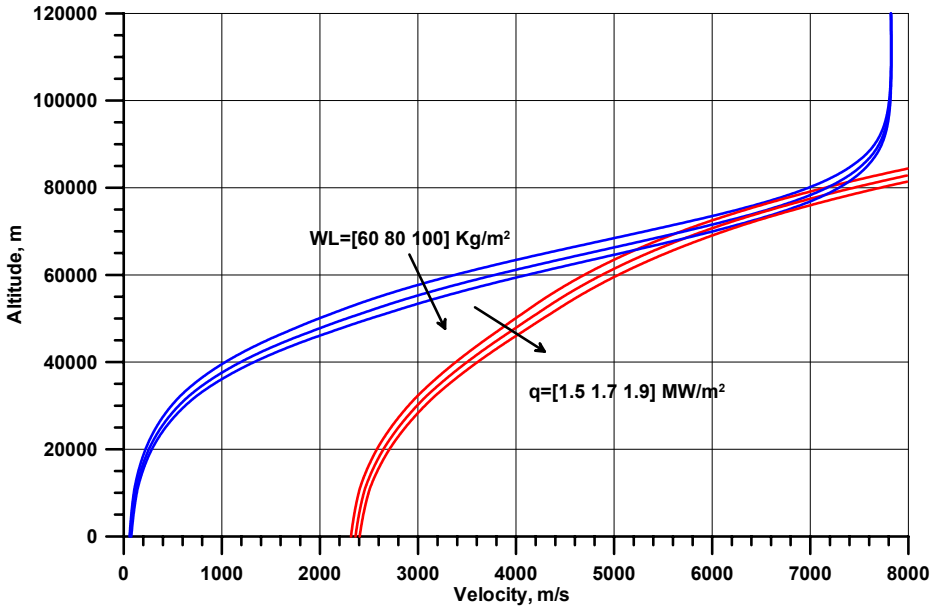

Figure 2-16. Re-entry corridors

The re-entry flight corridors in the altitude-velocity plane (Fig. 2-16) are bounded by two curves:

1. the equilibrium glide curve (γ=0) at the maximum lift coefficient (C_{Lmx}):

$$\rho_\infty v_\infty^2 = \frac{2}{C_{Lmx}} \frac{m}{S_r} \left(g - \frac{v^2}{r} \right)$$

where the value of C_{Lmx} is a function of Mach number and of the angle of attack (α).

2. the curve corresponding to the maximum radiation equilibrium temperature T_{wmax} at the stagnation point that the tip material can tolerate. This curve satisfies the equation:

$$T_{w\max} \cong \sqrt[4]{\frac{\dot{q}_s}{\varepsilon\sigma}} = T_{wmax}(\rho_\infty, R_n, V_\infty)$$

where $\dot{q}_s$ is the stagnation point convective heat flux at the "local" radiative equilibrium conditions for the stagnation point (R_n=1.5cm, red curve).

A flight corridor exists whenever the curve of equilibrium glide (blue) runs higher than the curve of maximum T_{wmax}. The almost tangent red curves to the equilibrium glide curves (blue) refer to the minimum stagnation point temperature needed to define a re-entry corridor, depending by the wing loading, and correspond to 2400, 2470 and 2540K. The corresponding re-entry trajectories limited to hypersonic flight (M>5) are shown in the figures 2-17.

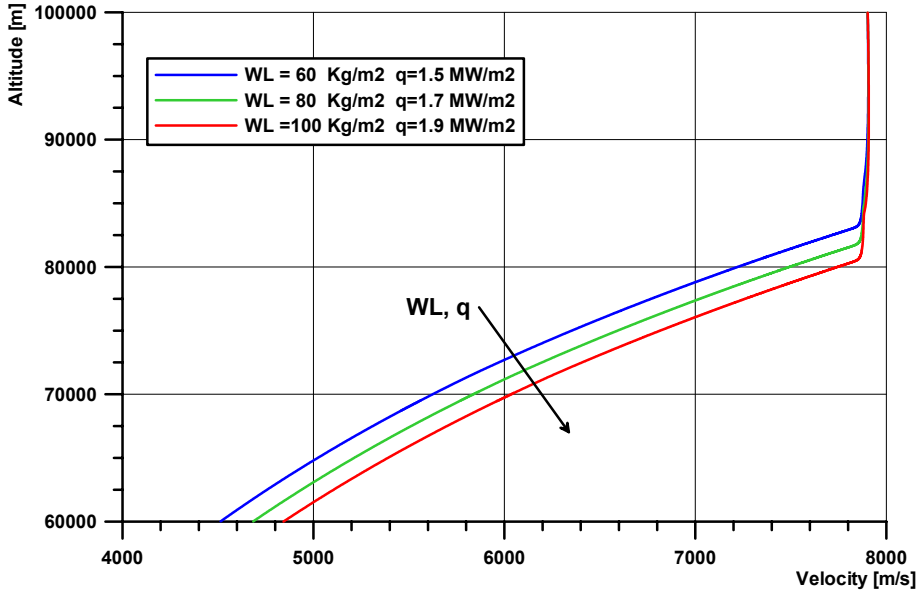

Figure 2-17 – Possible trajectories in the Z-V plane

By these preliminary results the wing loading has been fixed to 80 kg/m^2 and the maximum stagnation point heat flux at the radiative equilibrium condition has been fixed to 1.7MW/m^2.

2.6 Mission Architecture

The reference mission selection involves the re-entry phase from LEO. The previous phases of the missions (i.e. launch, orbit insertion, etc.) are not considered in this study.

The reference mission (Fig. 2-18) is characterized by an entry velocity of 7.8 km/s (LEO velocity) and with an entry flight path angle of about 0.5°-1.5°. The payload consists of three crew members and related items for a human payload mass of about 600 kg. The necessary vehicle internal volume must be not lower than 6m^3. The vehicle must be able to perform a landing on conventional runways.

Table 2-2. Reference Missions

MISSION PARAMETER	REFERENCE MISSION 1
P/L Return Orbit	
Altitude	**120 km**
Velocity	**7.8 km/s**
P/L Capabilities	**3 Astronauts**
Mass	**100 kg pp +100 kg crew items pp**
Volume	**6m^3**
Landing Sites	**Standard airport**
Vehicle Nominal Operations	▪ **Attached to ISS** ▪ **De-boost** ▪ **Separation of service module** ▪ **Re-entry and landing**

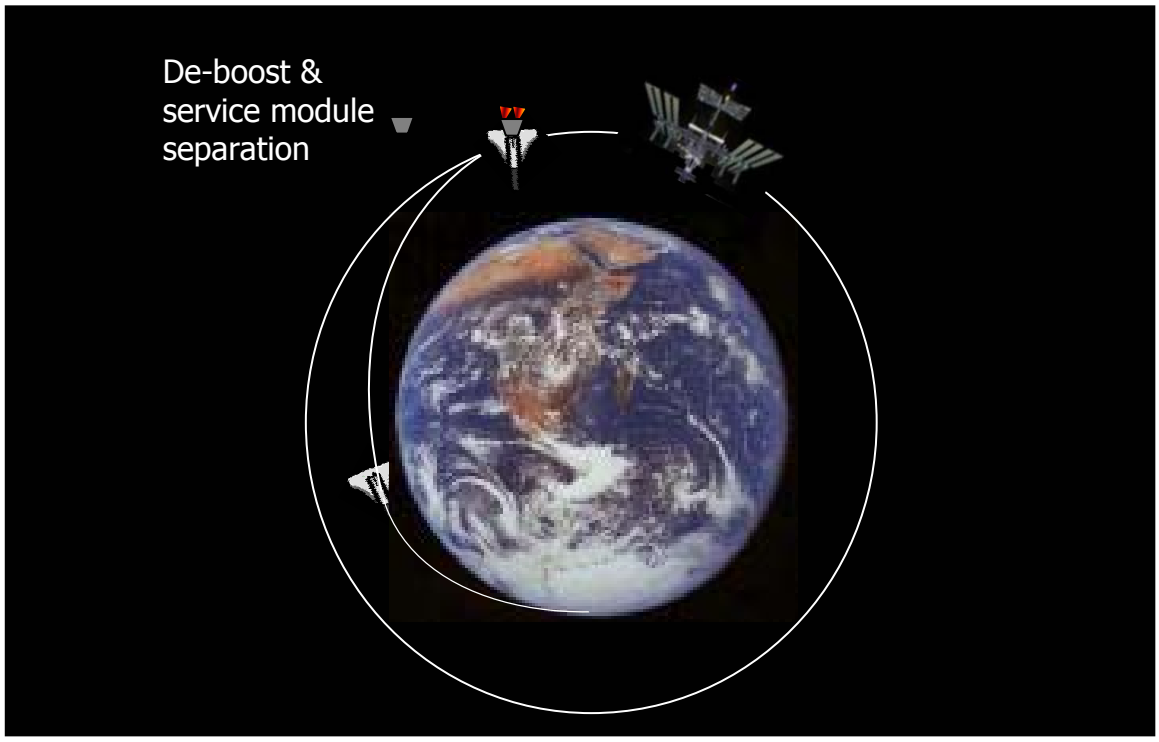

Figure 2-18. Reference mission 1: LEO re-entry

The mission architecture consists of a Return Vehicle (**RV**) and of a Service Module (**SM**) (fig. 2-19)

The **SM** contains propulsion system, fuel, consumables and power-generation/storage for orbital phase prior to re-entry; it is separated at the re-entry interface (SM is not the objective of this study).

The **RV** contains only resources (air, power, etc.) for limited re-entry time (approx. 8 hours) and it performs autonomous, horizontal landing on conventional runway for a direct re-entry or ISS docking for aerocapture mode.

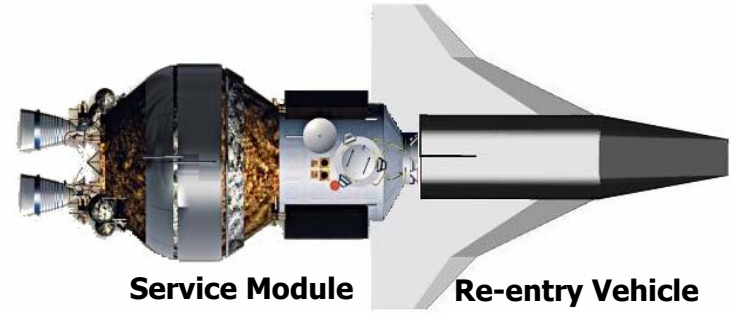

Figure 2-19. Vehicle architecture.

2.7 Summary and Comments

After a brief review of the possible re-entry strategy, a gliding approach has been chosen in order to reduce the kinetic energy dissipation rate with the results of a strong reduction of deceleration level. In addition a slow thermal dissipation avoiding the peak heating occurring during capsule like re-entry has been achieved. This choice is sustained, by a thermal point of view, by the exploiting the Boundary Layer Thermal Protection concept allowing to use massive materials only at the tip of the nose and of the leading edges than the ceramic tiles of the Shuttle on the whole belly. This work in the direction of a beneficial reduction in weight (so low wing loading) and in maintenances/refurbishments costs. The existence of an innovative class of materials able to sustain 2500 K allows to use sharp leading edges improving the aerodynamic characteristics of the vehicle and it allow to fly at higher altitude for a long time than the Space Shuttle. All these characteristics make of the proposed vehicle and strategy an interesting alternative for re-entry vehicle as looking for a lifeboat for the ISS as for the long term exploiting of the space for tourism.

References

Anderson Jr. J.D., *Hypersonic and High Temperature Gas Dynamics*, Mc-Graw Hill Book Co., New York, 1989, p. 498.

Arnold J., Johnson S. and Wercinski P., " SHARP: NASA's Research and Development Activities in Ultra High Temperature Ceramic Nose Caps and Leading Edges for Future Space Transportation Vehicles", *52nd International Astronautical Congress*, May 1-5, 2001, Toulouse, France.

Arringhton J.P., Jones J.J., "Shuttle Performance: Lessons Learned", NASA Conference Publication 2283, 1983

Dispersion-Strengthened High Temperature Materials, Material Properties and Application, PLANSEE, 2004, http:/www.plansee.com

Eggers, A. J., Allen, H. J., and Neice, S. E., "A Comparative Analysis of the Performance of Long-Range Hypervelocity Vehicles", NACA TN-4046, 1957.

Fahrenoltz W.G., Hilmas G.E., Final Report from "*NSF-AFOSR Joint Workshop on Future Ultra-High Temperature Materials"*, 2004 , URL: web.umr.edu/~uhtm.

Gasch M., Ellerby D., Irby E., Beckman S., Gusman M., Johnson S., "Processing, properties and arc-jet oxidation of hafnium diboride/silicon carbide ultra high temperature ceramics", Journal of Materials Science, No. 39, 2004, pp. 5925-5937.

Graves , C. A., Harpold, J. C., "Re-Entry Targeting Philosophy and Flight Results from Apollo 10 and 11", AIAA Paper 70-28, Jan. 1970.

Hanson, J. M., Coughlin, D. J., Dukeman, G. A., Mulqueen, J. A. and McCarter J. W., Ascent, transition, entry, and abort guidance algorithm design for the X-33 vehicle, AIAA-1998-4409, Guidance, Navigation, and Control Conference and Exhibit, Boston, MA, Aug. 10-12, 1998

Harpold, J. C., Graves , C. A., "Shuttle Entry Guidance", Journal of the Aeronautical Sciences, Vol. 27, July-Sept. 1979, pp. 158-163.

Jaensch, C., Markl, A., Trajectory optimization and guidance for a Hermes-type re-entry vehicle, AIAA Guidance, Navigation and Control Conference, New Orleans, LA, Aug. 12-14, 1991.

Larson, W. J., Pranke, L. K., Human Spaceflight: Mission Analysis and Design, McGraw-Hill Companies, 1999.

Larson, W. J., Wertz, J. R., Space Mission Analysis and Design, Microcosm Press, 1999.

Monti R.,"Aerotermodinamica del rientro atmosferico a basso rischio", XVII Congresso Nazionale AIDAA, Roma 15-19 September 2003

Monti R.. and Pezzella G., "A new philosophy for the design of re-entry vehicles", Space Technology, Vol. 24, No 4, pp.179-191 - 2004

Monti R., De Stefano Fumo M. and Savino R., "Thermal shielding of a re-entry vehicle by UHTC materials", 13th International Space Planes and Hypersonic Systems and Technologies Conference, May 16-20, 2005, Capua, Italy. Pubblicato in Journal of Thermophysics and Heat Transfer, Vol. 20, n.3, pp 500-506, 2006.

Monti, R., Pezzella, G., Savino, R., Paterna, D., and Esposito, A., Aerothermodynamic Study of an Advanced Thermal Protection System, Proceedings of the 4th European Symposium on Hot Structure and Thermal Protection Systems for Space Vehicles, ESA SP-521, Nov. 2002,pp. 139–146.

Monti R., Savino R., De Stefano Fumo M., "On Wind Tunnel Testing of Low Risk Re-entry Trajectory", *4th International Symposium Atmospheric Re-entry Vehicles& Systems*, March 21-23, 2005, Arcachon, France.
Moore, T. E., "Space Shuttle Entry Terminal Area Energy Management", NASA TM-104744, Novemberv 1991.

Platus, D. H., "Ballistic Re-entry Vehicle Flight Dynamics", Journal of Guidance, Control, and Dynamics, Vol. 5, Jan.-Feb. 1982, pp. 4-16.

Rasky, D. J., Advanced Ceramic Matrix Composites for TPS, Current Technology for Thermal Protection System, NASA CP-3157, 1992, pp. 43-52.

Tauber M.E., " A Review of High Speed Convective, Heat-Transfer Computation Methods, NASA Technical Paper 2914, 1989.

TPS-X Database Website, NASA Ames Research Center, http://tpsx.arc.nasa.gov.

CHAPTER 3

VEHICLE CONCEPT

3.1 Vehicle Description and Characteristics

The baseline vehicles for LEO re-entry is characterized by a length of 11 m and a wingspan of 9 m and has accommodation for three astronauts (and the crew items) with an internal volume of $6m^3$ as requested by the requirements. The airframe consists of a double-delta wing with leading edge sweep angles of 65° and 45° with five trailing edge control surfaces, a vertical tail and a fuselage with a forward cone angle of 20°. The entire lower side of the vehicle is flat. The fuselage is separated in three compartments (fig. 3-1), two unpressurized compartments for the equipment and landing gears and a pressurized compartment for the crew, providing space for three astronauts. The hatch and docking port is located on top of the fuselage, whereas the interface to the resource module is at the back side of the vehicle [Janovsky et al., 2006]. Including all subsystems and the crew, a total mass of approx. 4200 kg for the RV was determined [MacConochie & Klich, 1978]. The vehicles are equipped with a tricycle landing gear with pneumatic tires.

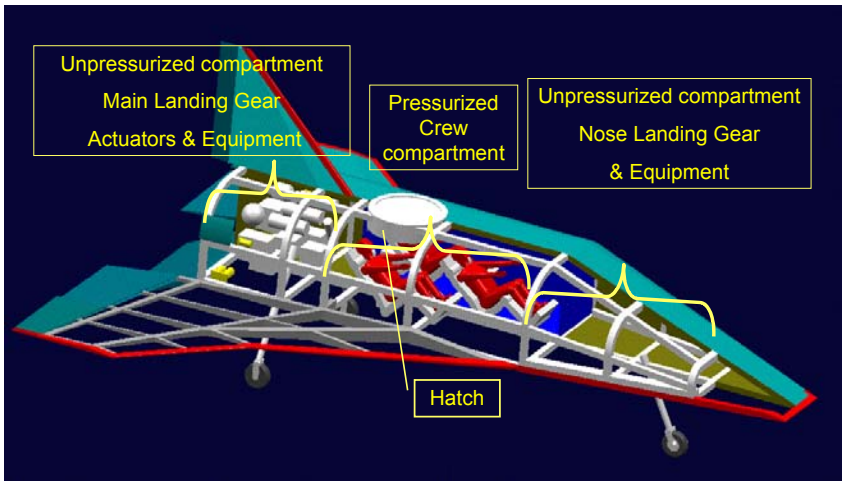

Figure 3-1. Re-entry vehicle configuration.

3.2 Aerodynamic Dataset

Two different numerical methodologies have been employed for the computation of aerodynamic coefficients: one is based on a Computational Fluid-Dynamic (CFD) code, which spans all the range of Mach numbers; the other relies on a numerical code based on approximate methods, and is limited to the hypersonic part of the re-entry trajectory.

An initial phase has been dedicated to the mesh development. Preliminary CFD computations have been then performed to assess the grid independence on aerodynamic coefficients of the computed solutions. Furthermore, hypersonic eulerian CFD computations have been performed to cross-check the numerical code based on approximate methods.

The CFD numerical code has been utilized for the computation of the subsonic, transonic and supersonic portion of the trajectory. In particular, simulations corresponding to Mach numbers: 0.3, 0.5, 0.7, 0.9, 2, and to angles of attack: 0, 10, 20 [deg], have been performed.

The approximate methodology has been utilized to compute the aerodynamic coefficients at Mach numbers of 5, 10, 15, 20, 25, and at different angles of attack (from -20 to 20 [deg]).

3.2.1 Description Of The Reference Frame

The origin of the coordinate system is on the vehicle nose, in the symmetry plane (fig. 3-2). The x axis (roll axis) is along the body length, in the symmetry plane. The y axis is the pitch axis and z the yaw axis.

The reference area is the planform area (A=49.6 m^2). The reference length for the moments calculations is 1 m and the reference point is on the nose.

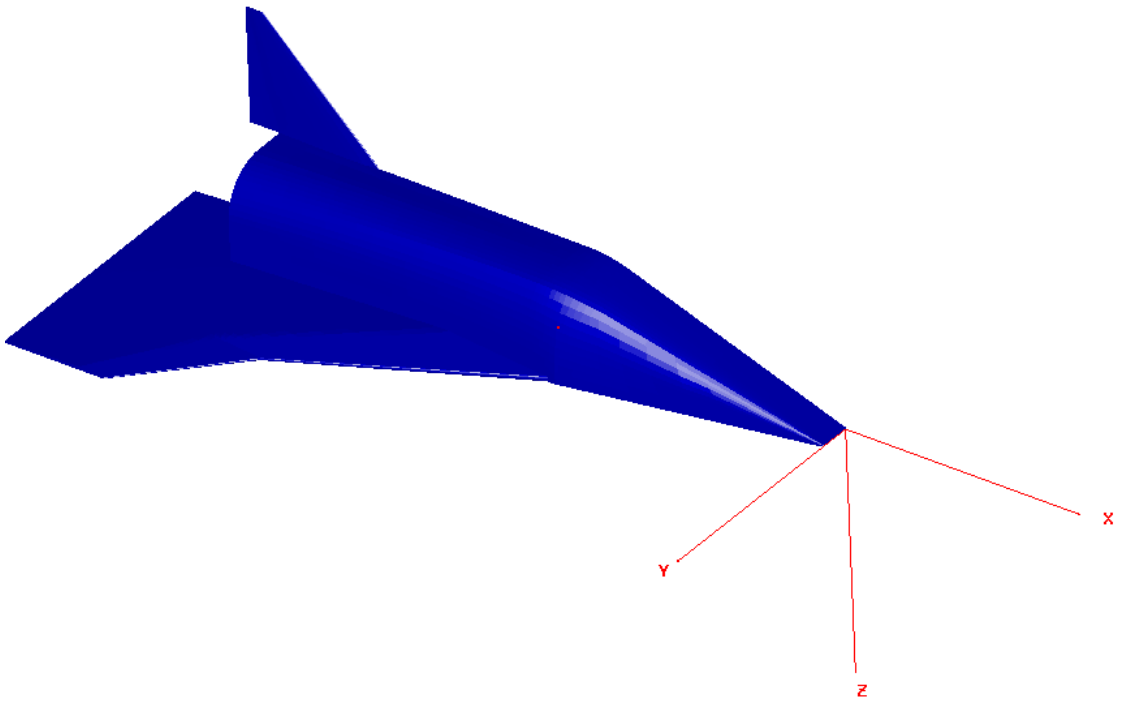

Figure 3-2. Geometry and reference frame (half model)

3.2.2 Description of the Numerical Model

The CFD code utilizes the finite volume method to solve the three-dimensional Euler equations in a block-structured discretized domain.

Numerical inviscid fluxes are based on the flux difference splitting technique [Savino and Paterna, 2005], while diffusive fluxes are computed using central schemes. Second order accuracy is achieved by the use of the minmod flux limiter. Time integration is fully implicit. The resulting linear system is solved by means of an Algebraic Multi-Grid (AMG) method [Weiss et al., 1999].

CFD computations are performed on a parallel cluster of workstations.

Hypersonic coefficients are computed according to approximate methodologies. In particular, on the vehicle wing the tangent wedge method [Anderson, 2000] and/or the hypersonic small disturbance theory [van Dyke, 1954] are adopted.

Figures 3-3 show two views of the surface mesh on the re-entry vehicle. The surface mesh is the same for both the CFD and approximate methods computations.

The volume grid is composed of a total of 103 and 53 blocks, for subsonic and supersonic simulations, respectively. The blocks distribution on the vehicle surface is shown in fig. 3-4.

The total number of cells is about $8 \cdot 10^5$ for subsonic and transonic simulations, $5 \cdot 10^5$ for supersonic and hypersonic computations. These grid sizes are the result of a grid convergence analysis, aimed at assuring the independence of the computed results from the mesh size.

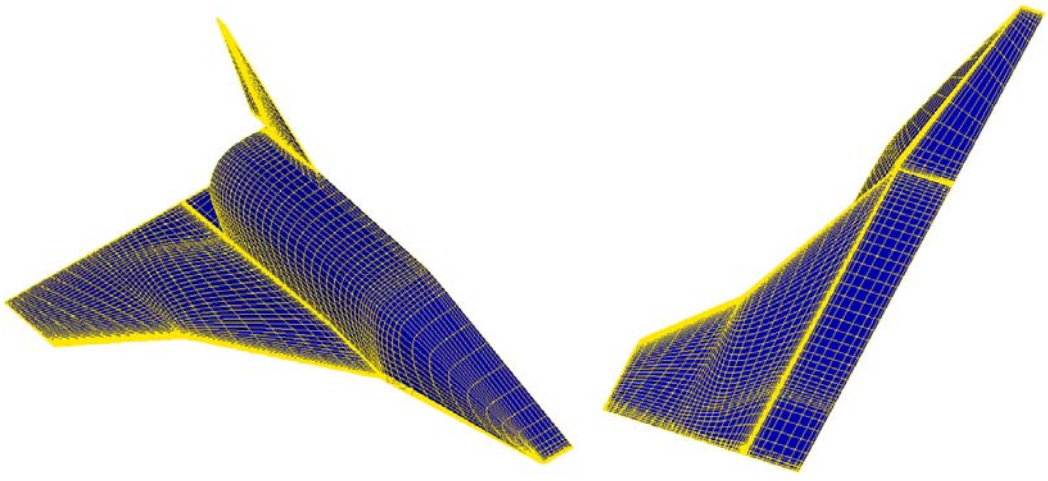

(a) **(b)**

Figure 3-3. Surface mesh; a) Top view; b) Bottom view

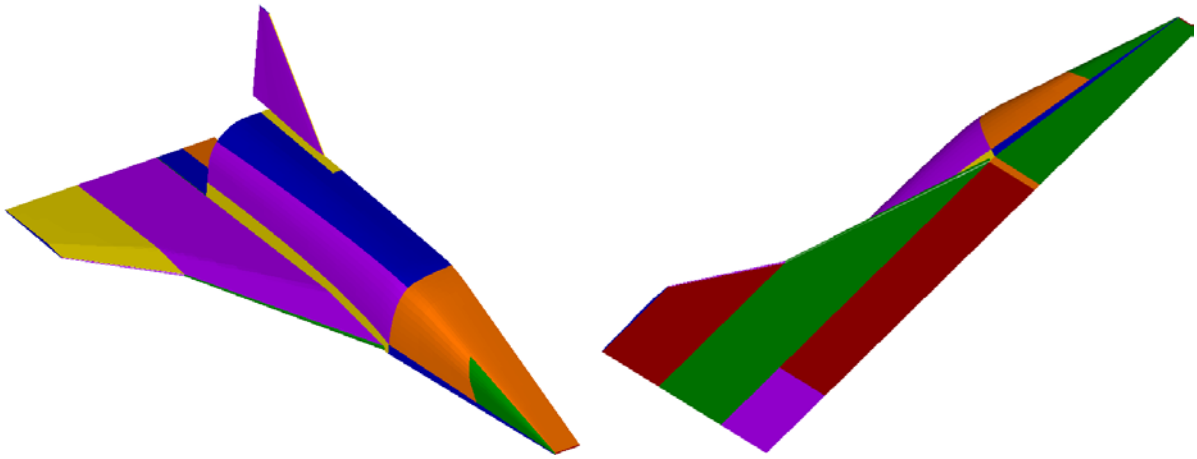

(a) (b)

Figure 3-4. Block traces (in different colors) on the vehicle surface

The total number of cells is about $8 \cdot 10^5$ for subsonic and transonic simulations, $5 \cdot 10^5$ for supersonic and hypersonic computations. These grid sizes are the result of a grid convergence analysis, aimed at assuring the independence of the computed results from the mesh size [Papadopoulos et al., 1999].

Since Eulerian computations have been performed, the grid has not been refined near the body. In the supersonic cases the shock layer has been suitably refined. The external boundary position has been chosen to avoid problems of interference with the flowfield around the vehicle. In the case of the subsonic/transonic simulations, the overall length of the computational domains is about 5 times the length of the body. For supersonic/hypersonic simulations, the external domain is about two times the length of the vehicle.

3.2.3 Convergence Criteria for CFD Computations

The adopted convergence criteria rely basically on the values of the equations residuals (i.e. the time derivative terms) and of the global aerodynamic coefficients, during the iterations. Figures 3-5, 3-6 and 3-7 show, respectively, the drag, lift and moment coefficients profiles during the iterations. It can be seen from figures 3-5, 3-6 and 3-7 that 3000 iterations are sufficient to consider the solution as converged, since the coefficients profile is flat. Furthermore, the corresponding equations residuals drop by about three orders of magnitude

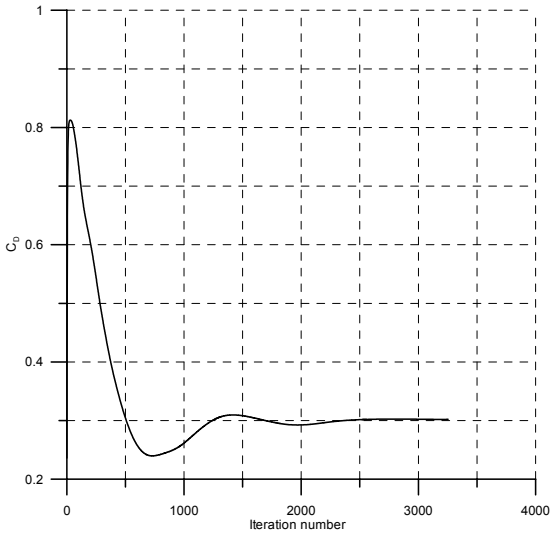

Figure 3-5. Lift coefficient profile during CFD iterations (M=0.3; α=20°)

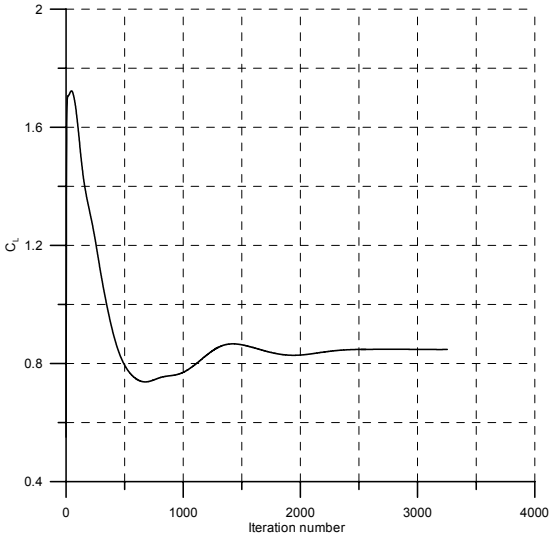

Figure 3-6. Drag coefficient profile during CFD iterations (M=0.3; α=20°)

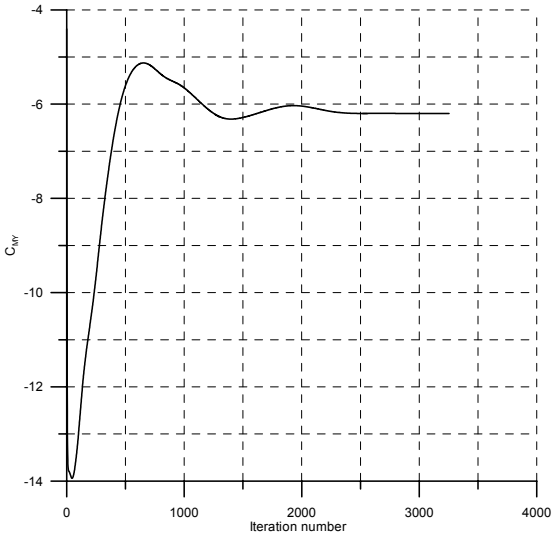

Figure 3-7. Pitching moment coefficient profile during CFD iterations (M=0.3; α =20°)

3.2.4 Comparison of the two Numerical Models

Preliminary computations have been performed to cross-check the results of the two numerical codes. The results for four hypersonic flight conditions, corresponding to Mach numbers 5 and 15, and angles of attack 0 and 20, are shown in Table 3-1.
Apart from the lift and pitching moment coefficient values at 0 angle of attack, which are not relevant since close to 0, a good agreement is found at all flight conditions.

Table 3-1. Numerical codes comparison

M=5	**APPR. METHODS**			**CFD**		
	C_L	**C_D**	**C_{my}**	**C_L**	**C_D**	**C_{my}**
α=0	-0,052	0,026	0,32	-0,037	0,025	0,086
α=20	0,36	0,13	-3,1	0,33	0,13	-2.7
M=15	**APPR. METHODS**			**CFD**		
	C_L	**C_D**	**C_{my}**	**C_L**	**C_D**	**C_{my}**
α=0	-0,044	0,022	0,28	-0,045	0,022	0,1
α=20	0,276	0,106	-2.3	0,273	0,101	-2,2

3.2.5 Computation of Aerodynamic Coefficients

3.2.5.1 Subsonic-Supersonic regime

The pressure distribution on the vehicle surface, corresponding to the simulations M=0.3, α=20 [deg], and M=2, α=10 [deg], are shown in figg. 3-8and 3-9.

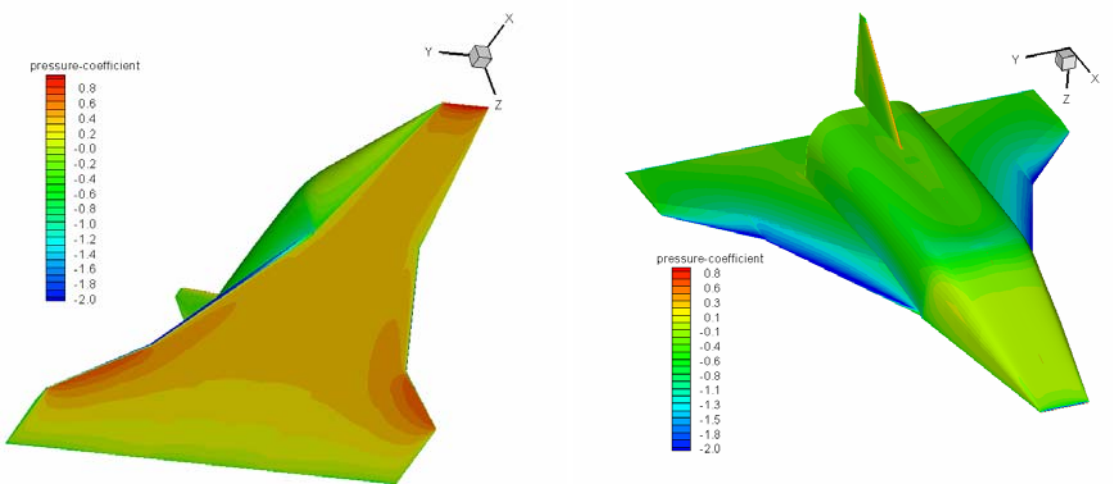

(a) (b)

Figure 3-8. Pressure coefficient distribution corresponding to M=0.3, α=20°

(a) Windside; (b) Leeside

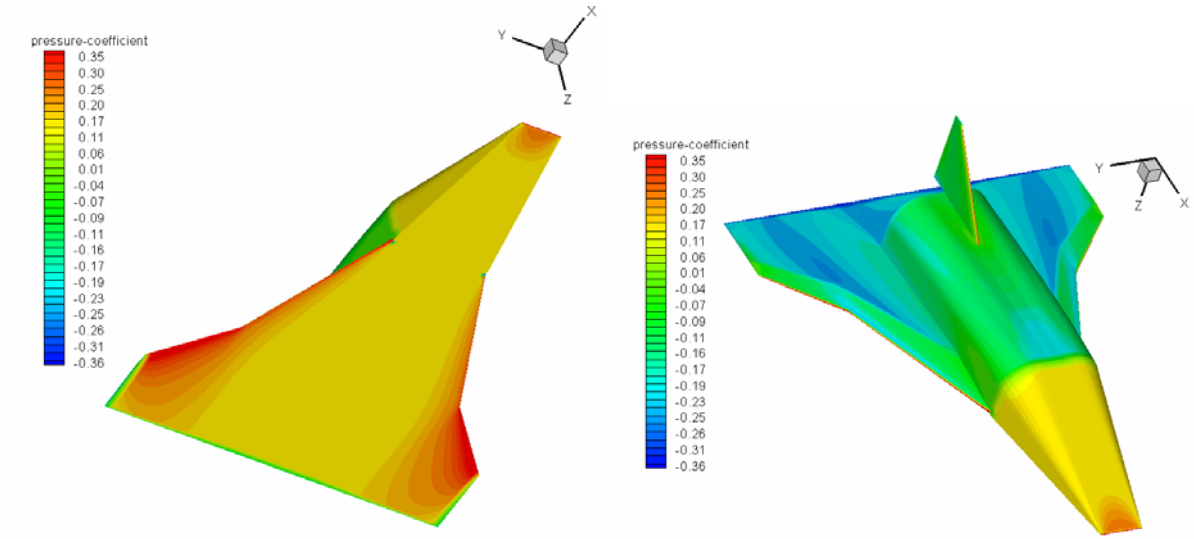

(a) (b)

Figure 3-9. Pressure coefficient distribution corresponding to M=2, α =10°

(a) Windside; (b) Leeside

The corresponding pressure distributions in the symmetry plane are shown in figg. 3-10and 3-11.

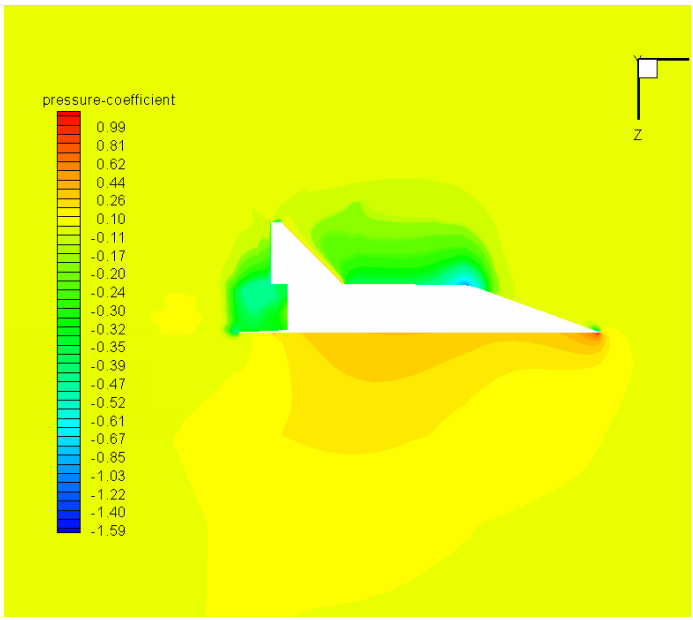

Figure 3-10. Pressure coefficient distribution in the symmetry plane (M=0.3, α=20°)

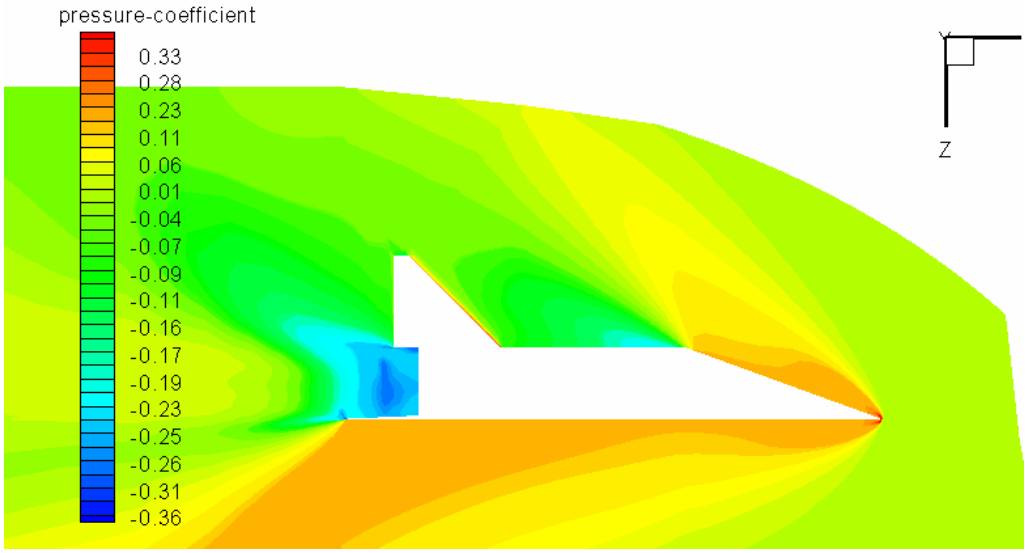

Figure 3-11. Pressure coefficient distribution in the symmetry plane (M=2, α=10 [deg]).

In the supersonic case a shock wave is formed around the nose, which has the same shock angle both on the windside and on the leeside, due to the angle of attack of 10°

Figures 3-12, 3-13 and 3-14 show the behaviour of aerodynamic coefficients with angle of attack, for two values of Mach number. The lift and pitching moment coefficients have an almost linear profile in the examined range of angles of attack, while the drag coefficient presents the typical parabolic behaviour. The lift curve slope is about 2.

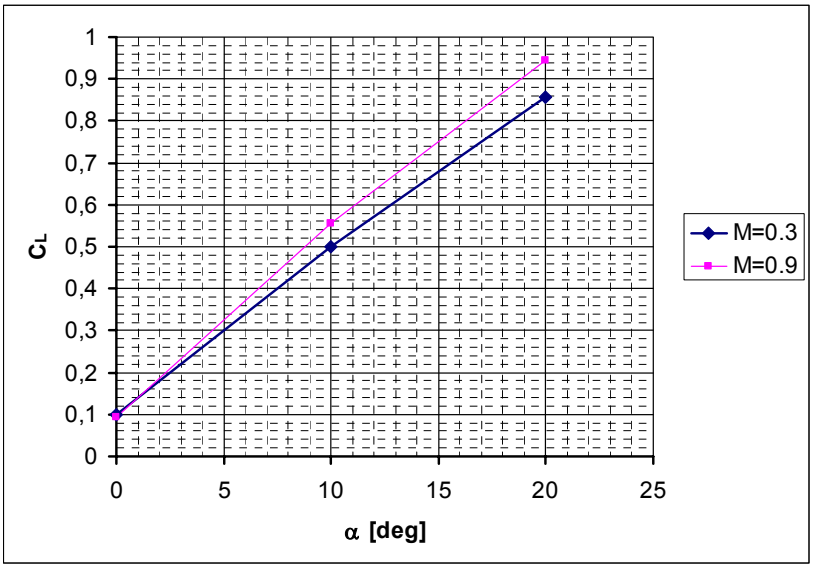

Figure 3-12. Lift coefficient vs. angle of attack (M=0.3, M=0.9)

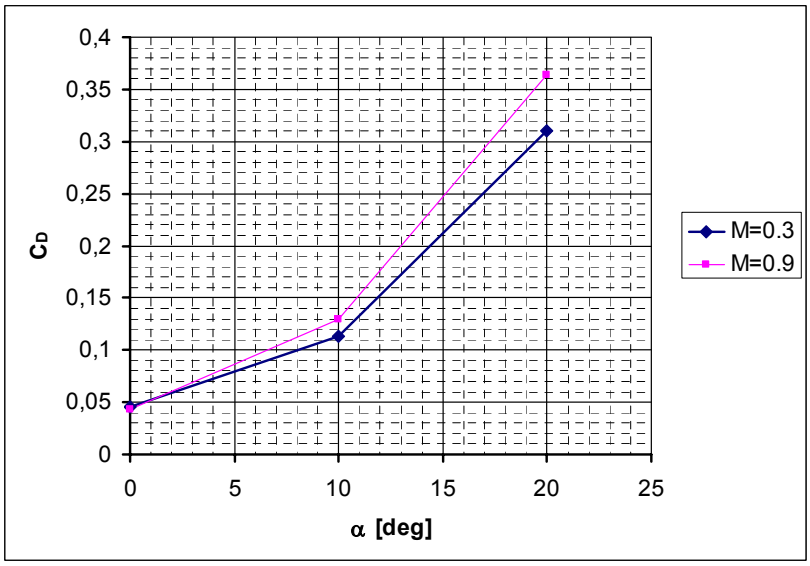

Figure 3-13. Drag coefficient vs. angle of attack (M=0.3, M=0.9)

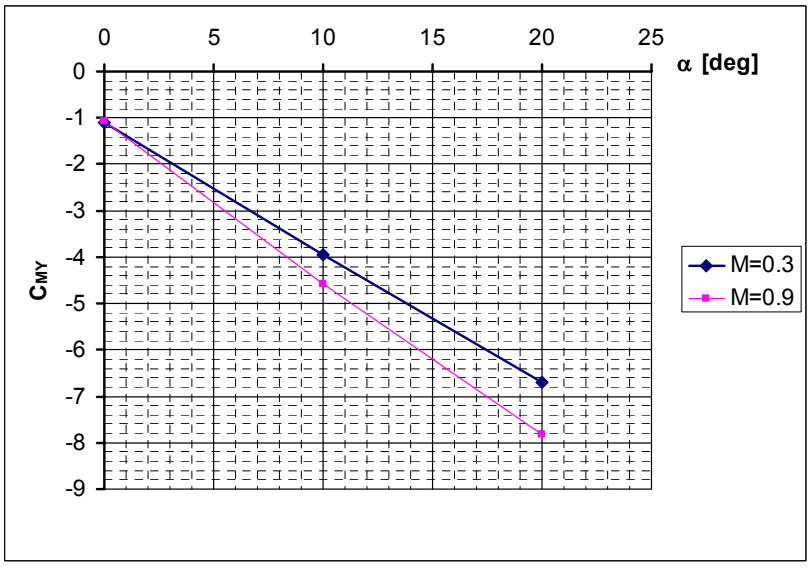

Figure 3-14. Pitching moment coefficient vs. angle of attack (M=0.3, M=0.9)

3.2.5.2 Hypersonic regime

Lift and drag coefficients behaviour with angle of attack at hypersonic Mach numbers is shown in Figs. 3-15 and 3-16. Contrary to the subsonic and supersonic cases, the functional dependence on the angle of attack is α^2 and α^3, respectively for lift and drag coefficients.

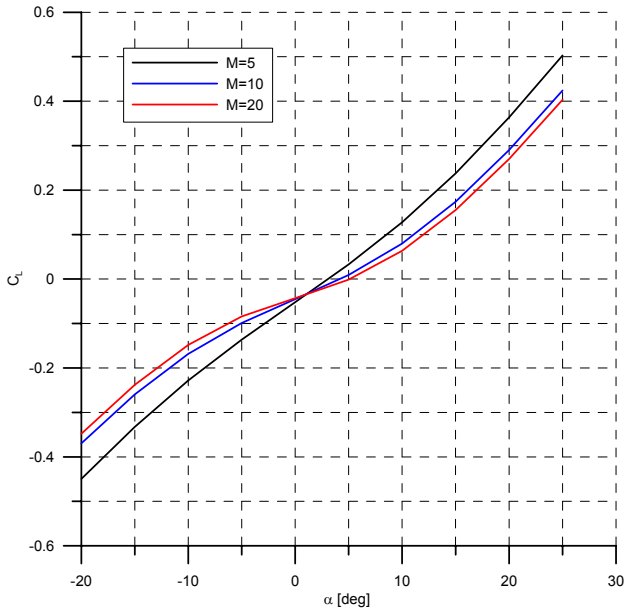

Figure 3-15. Lift coefficient vs. angle of attack (hypersonic regime)

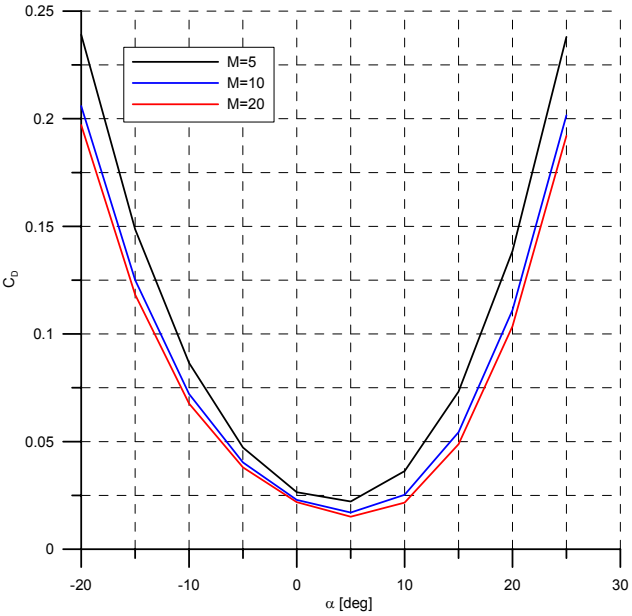

Figure 3-16 – Drag coefficient vs. angle of attack (hypersonic regime)

Figure 3-17 shows the aerodynamic efficiency in the hypersonic regime. An efficiency larger than two is attained in the range $7° \leq \alpha \leq 20°$.

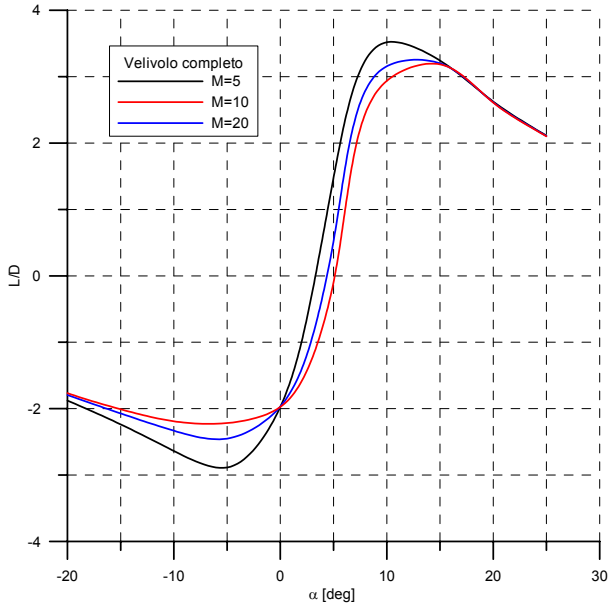

Figure 3-17. Aerodynamic efficiency vs. angle of attack (hypersonic regime)

The following table summarizes the computational matrix and the corresponding computed global coefficients.

Table 3-2. Computational matrix and corresponding aerodynamic coefficients

Mach number	Angle of attack [deg]	Lift coefficient	Drag coefficient	Pitch moment coefficient
0.3	0	0,1	0,0456	-1,088
	10	0,499	0,113	-3,939
	20	0,857	0,31	-6,698
0.5	0	0,0971	0,0486	-1,082
	10	0,514	0,12	-4,092
	20	0,879	0,324	-6,937
0.7	0	0,0994	0,0452	-1,099
	10	0,525	0,121	-4,203
	20	0,897	0,334	-7,161
0.9	0	0,095	0,0426	-1,069
	10	0,557	0,129	-4,585
	20	0,945	0,364	-7,82
2	0	0,00188	0,0294	-0,269
	10	0,292	0,0869	-2,541
	20	0,55	0,219	-4,68

5	-20	-0,449	0,239	3,174
	-15	-0,332	0,149	2,183
	-10	-0,228	0,0865	1,377
	-5	-0,136	0,0472	0,720
	0	-0,0523	0,0265	0,151
	5	0,0327	0,0222	-0,419
	10	0,128	0,0363	-1,079
	15	0,237	0,0732	-1,891
	20	0,364	0,138	-2,893
10	-20	-0,369	0,206	2,534
	-15	-0,259	0,125	1,619
	-10	-0,168	0,072	0,932
	-5	-0,099	0,040	0,459
	0	-0,045	0,023	0,130
	5	0,009	0,017	-0,199
	10	0,080	0,025	-0,672
	15	0,174	0,054	-1,357
	20	0,290	0,111	-2,277
15	-20	-0,354	0,199	2,408
	-15	-0,243	0,120	1,497
	-10	-0,154	0,069	0,824
	-5	-0,089	0,039	0,386
	0	-0,044	0,022	0,125
	5	0,002	0,016	-0,136
	10	0,068	0,023	-0,571
	15	0,160	0,050	-1,242
	20	0,276	0,106	-2,153
20	-20	-0,348	0,197	2,363
	-15	-0,238	0,118	1,453
	-10	-0,148	0,068	0,782
	-5	-0,084	0,038	0,355
	0	-0,043	0,022	0,125
	5	-0,001	0,015	-0,109
	10	0,064	0,022	-0,533
	15	0,155	0,049	-1,200
	20	0,270	0,104	-2,109

25	-20	-0,345	0,196	2,342
	-15	-0,235	0,118	1,433
	-10	-0,146	0,067	0,763
	-5	-0,082	0,038	0,339
	0	-0,043	0,022	0,124
	5	-0,003	0,015	-0,095
	10	0,061	0,021	-0,514
	15	0,153	0,048	-1,180
	20	0,268	0,103	-2,089

3.2.6 Effect of Mach number

Figures 3-18 and 3-19 show the behaviour of the global lift and drag coefficients with the freestream Mach number. The coefficients rise with Mach number in the subsonic regime, especially at high angles of attack, reaching a maximum at about M=1, then decrease in the supersonic/hypersonic regime, approaching a constant value for Mach numbers above 10 (in agreement with the Mach number independence principle).

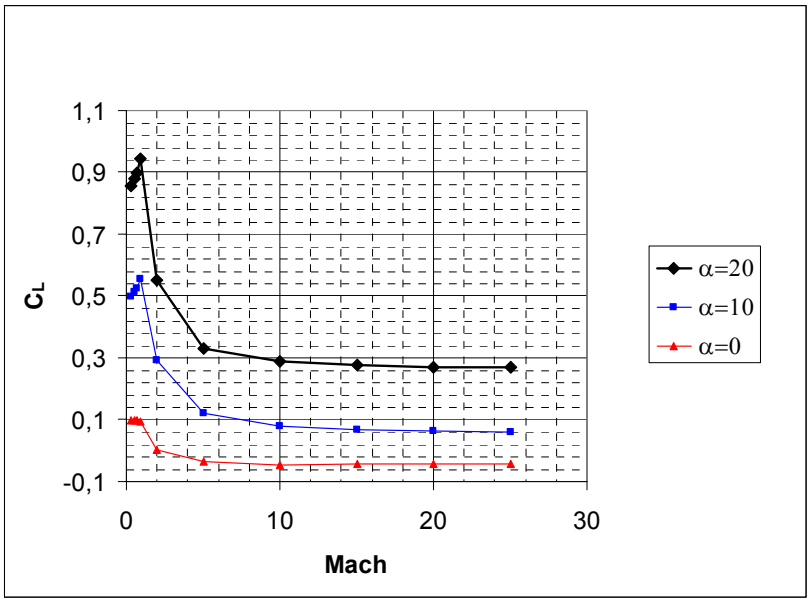

Figure 3-18. Lift coefficient vs. Mach number

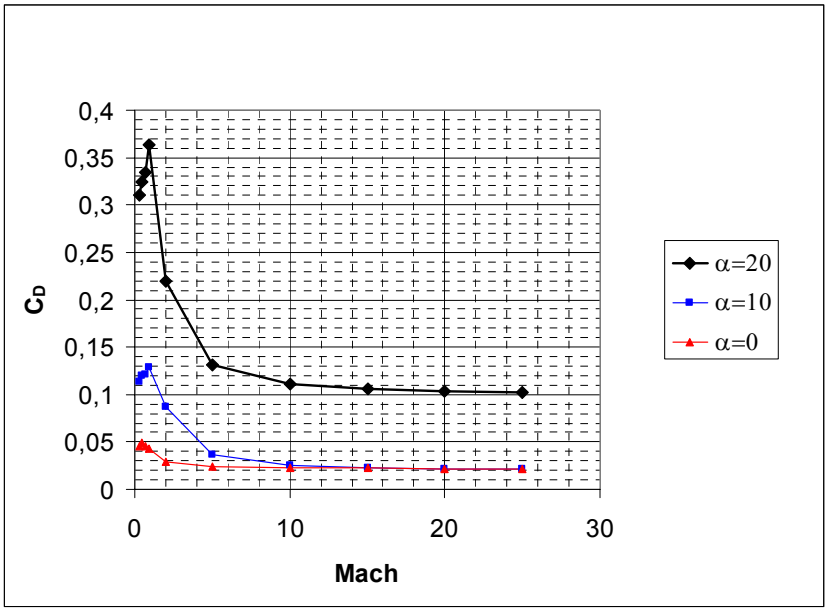

Figure 3-19. Drag coefficient vs. Mach number

The same behaviour is presented by the lift curve slope , which is shown in fig. 3-20.

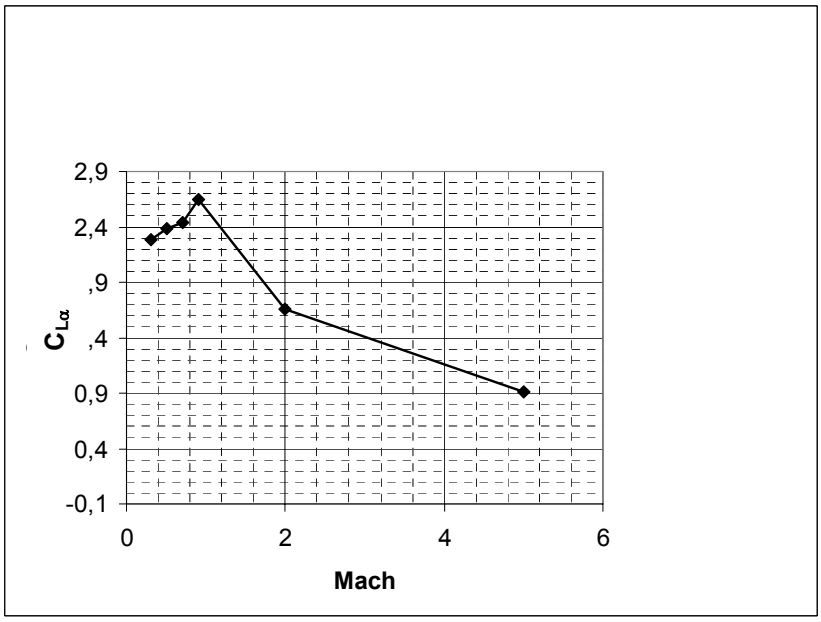

Figure 3-20. Lift slope coefficient vs. Mach number

The pitching moment coefficient as function of lift coefficient is shown in fig. 3-21. The behaviour is almost linear for all Mach numbers. However the slope dC_{my}/dC_l changes from subsonic to supersonic regime, passing from 7.8 to 8.3.

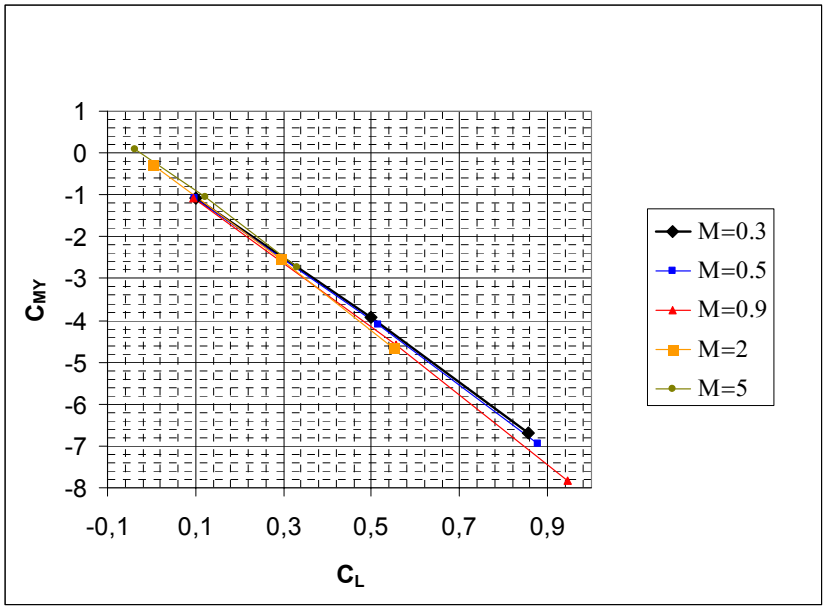

Figure 3-21. Pitching moment coefficient vs. lift coefficient

3.2.7 Reynolds number effects

Viscous effects are taken into account to evaluate their influence on lift, drag and pitching moment coefficients. To simulate the boundary layer around the body a grid refinement near walls has been performed on both the computational grids for subsonic/transonic and supersonic/hypersonic computations. Figure 3-22 shows the grid refinement on the fuselage in the symmetry plane.

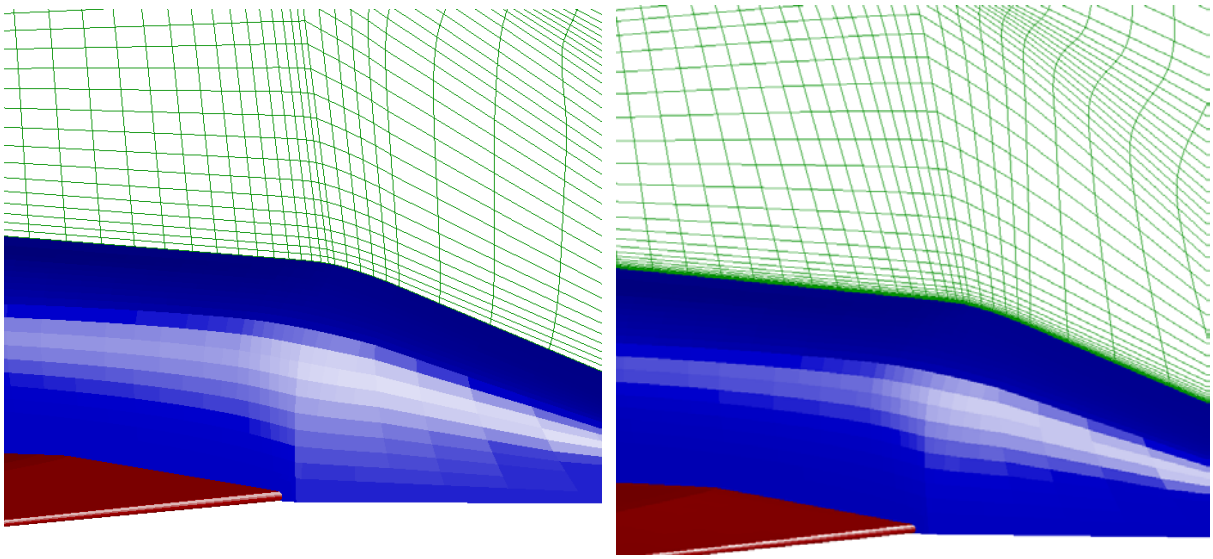

(a) **(b)**

Figure 3-22. Grid refinement accounting for viscous effects;
(a) original (eulerian) grid; (b) grid after near-wall refinement

Figures 3-23, 3-24 and 3-25 show the computed pressure distributions on the vehicle surface with and without taking into account fluid viscosity.

No substantial difference is present between the two cases for the low Mach number value, which corresponds to approximately sea levels altitudes along the re-entry trajectory, the Reynolds number for the selected case, based on the vehicle length, is about $7 \cdot 10^7$. At these values of the Reynolds number significant viscous effects are not expected.

This is confirmed by the values of the aerodynamic coefficients, which present negligible differences with respect to the previously computed inviscid values, see Table 3-3.

Same considerations hold for the transonic regime. Figure 3-24 shows the computed pressure distribution on the vehicle surface for M=0.9, α=20°, comparing the Eulerian results with the Navier-Stokes results.

When considering hypersonic Mach numbers, which correspond to higher altitudes along the re-entry trajectory, Reynolds numbers are lower and an increased importance of viscous effects on aerodynamic coefficients is expected. A trajectory point with an altitude of 43 km and an angle of attack of 13.6° have been selected. These flight conditions correspond to M=5 and a Reynolds number of about $6 \cdot 10^4$. Figure 3-25 shows that the surface pressure distribution is not affected by viscous effects at the considered flight condition. However, as shown in Table 3-3, viscous drag contribution to the total drag becomes more important. This is even more evident when considering the flight conditions at M=15 (z=60 km, a=13.6° along the re-entry trajectory), corresponding to a Reynolds number of $2.4 \cdot 10^4$. In this case, differences between viscous and inviscid drag coefficients of 30% have been computed. It can be noted that the pitching moment coefficient is almost unaffected by viscosity.

Table 3-3. Viscous effects on aerodynamic coefficients

Mach Number	Reynolds Number	AoA [deg]	Lift coefficient	ΔC_L w.r.t. inviscid calculations	Drag coefficient	ΔC_D w.r.t. inviscid calculations	Pitching moment coefficient	ΔC_M w.r.t. inviscid calculations
0.3	$7 \cdot 10^7$	20	0.857	0	0.312	+0.65%	-6.69	-0.12%
0.9	$7 \cdot 10^7$	20	0.944	-0.11%	0.365	+0.27%	-7.81	-0.13%
5	$6 \cdot 10^4$	13.6	0.146	-1.35%	0.0474	+8.71%	-1.096	-0.72%
15	$2.4 \cdot 10^4$	13.6	0.0989	-2.07%	0.0412	+31.6%	-0.723	-0.41%

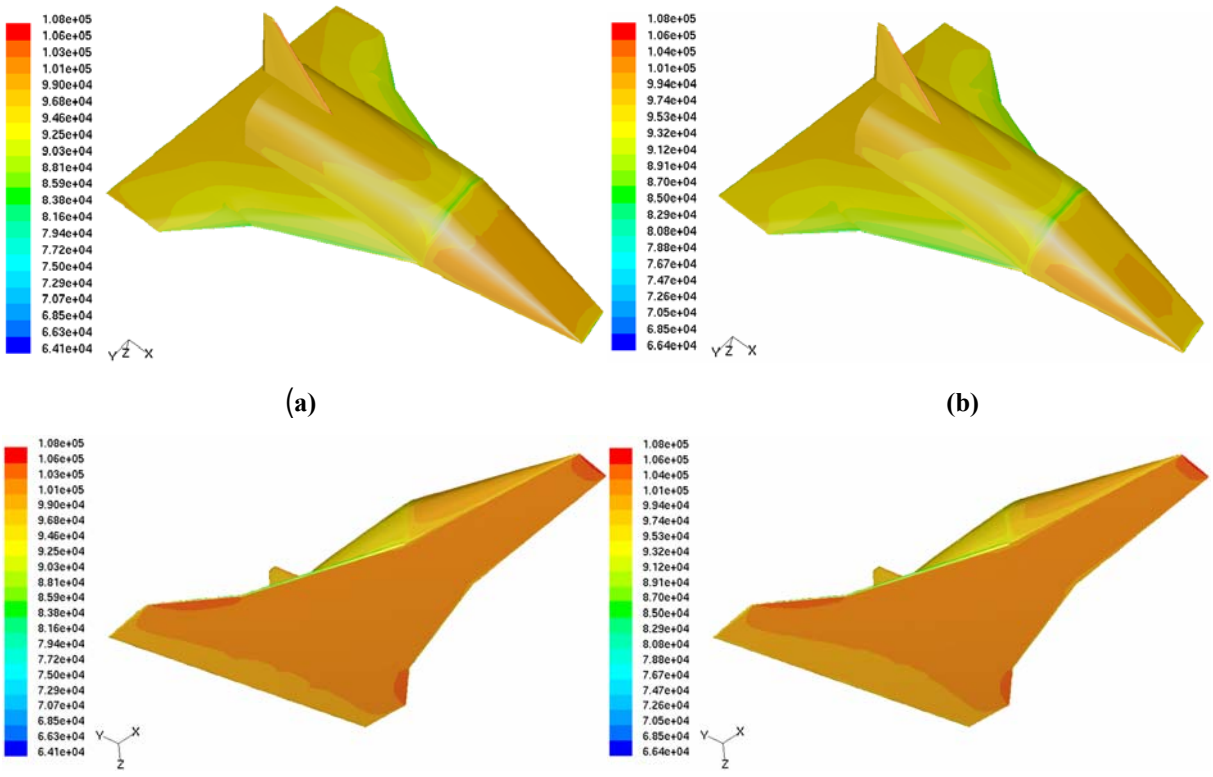

Figure 3-23. Pressure distribution on vehicle surface at M=0.3, α=20 deg;

Eulerian results: (a) Leeside; (c) WindsideNavier-Stokes results: (b) Leeside; (d) Windside

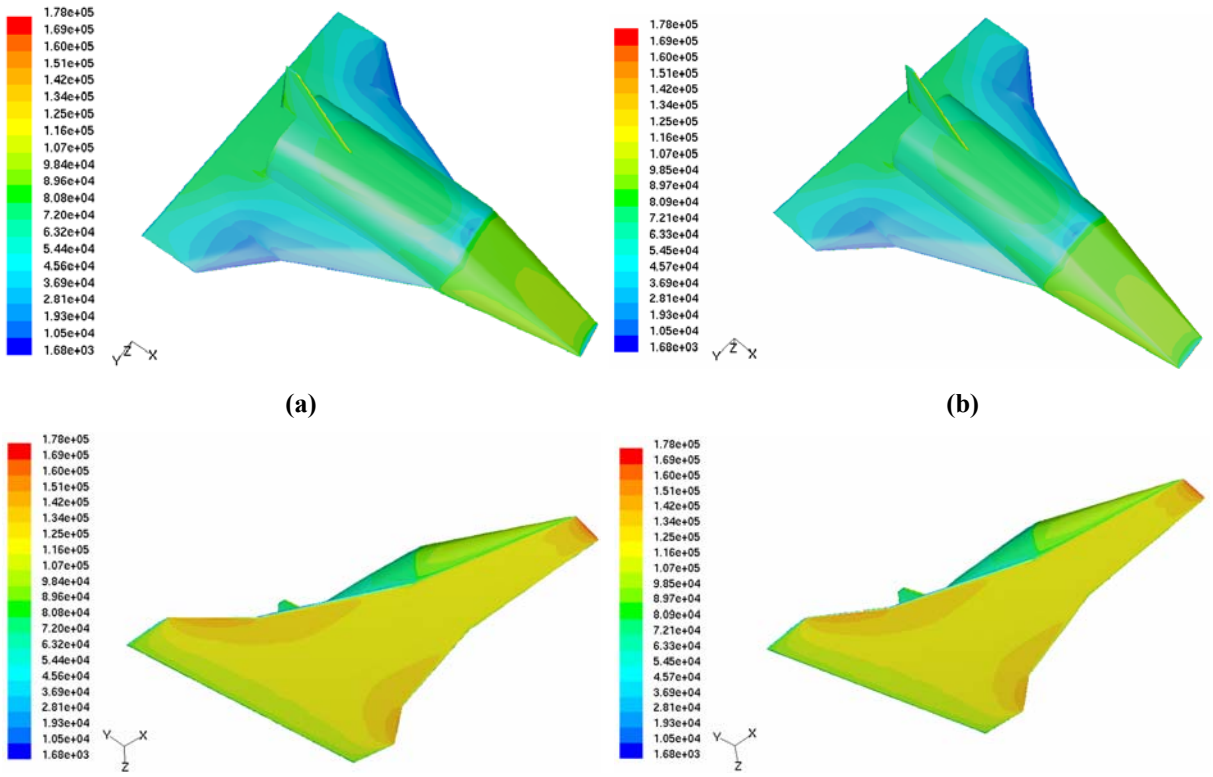

Figure 3-24. Pressure distribution on vehicle surface at M=0.9, α =20 deg;

Eulerian results: (a) Leeside; (c) Windside Navier-Stokes results: (b) Leeside; (d) Windside

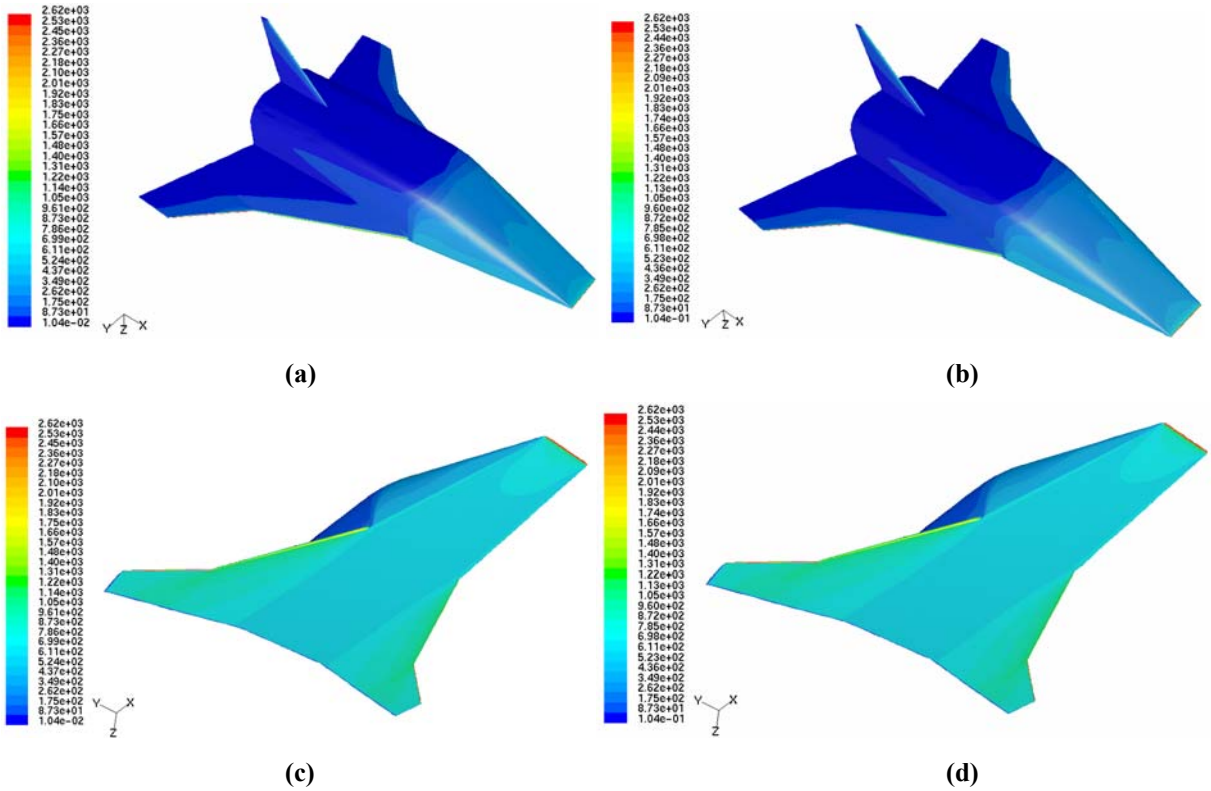

(a) **(b)**

(c) **(d)**

Figure 3-25. Pressure distribution on vehicle surface at M=5, α =13.6 deg;
Eulerian results: (a) Leeside; (c) Windside Navier-Stokes results: (b) Leeside; (d) Windside

3.2.8 Hypersonic Performance

In order to evaluate the hypersonic performance of proposed re-entry vehicle it has been compared with other seven re-entry vehicle configurations. Some of them have really flight at hypersonic conditions , i.e. the Space Shuttle and the X-15, others still remain in the minds of their designer but cancelled or delayed for different reasons by space agencies and governments. The different configurations are depicted in figure 3-26.

For hypersonic conditions, high L/D configurations have slender shapes and sharp leading edges that minimize the supersonic-wave drag of the wing. The blunt shapes of the lifting bodies necessary to produce lift at low speeds and to dissipate the heat of re-entry do not allow for good hypersonic L/D performance. A compromise is found in the form of delta-wing configurations that have triangular wing planforms, produce moderately high L/D at hypersonic speeds; yet also allow the capability to land horizontally on a normal runway [Ashley & Landhal, 1985]. The delta-wing is a compromise design that generates sufficient lift at low speeds by increasing the angle-of-attack of the wing, but also has sufficient sweepback and slenderness to perform very efficiently at high speeds. Figures 3-27 shows

how the hypersonic aerodynamic characteristics of delta-wing configurations differ from lifting bodies by the lift-to-drag ratios of four delta-wing re-entry configurations, the Shuttle, the X-34, the X-20 and the quasi-delta-wing X-15; to the planforms for three lifting-body configurations, the X-24A/SV-5D, the X-38, the X33 [Saltzman & Edwin, 1960; Franklin et al. 1959; Mort et al., 1970] These flight configurations were chosen for comparison because a fairly complete hypersonic flight and wind tunnel database exists for each.

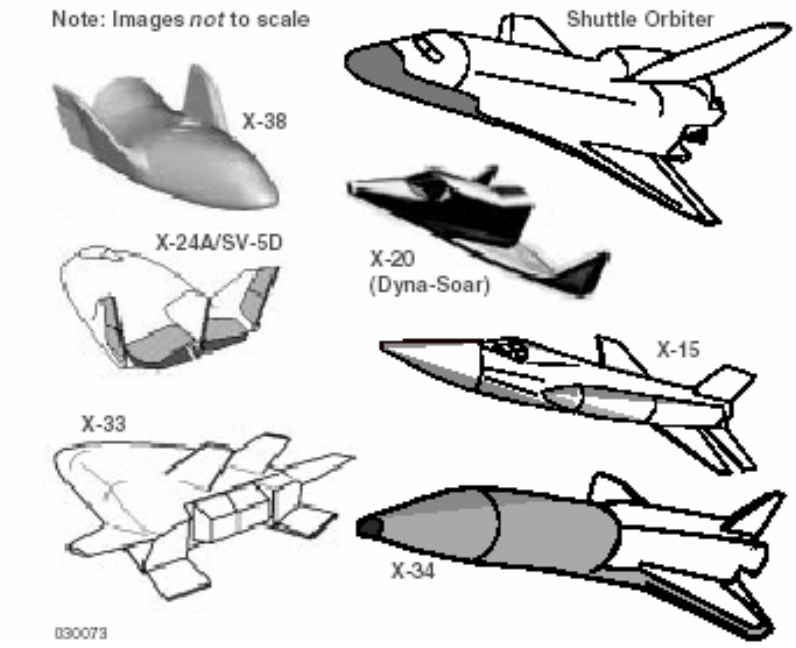

Figure 3-26. Comparisons for seven lifting re-entry configurations.

The winged configurations demonstrate a clear advantage over the lifting-body configurations. The wing-bodies exhibit L/D_{max} approximately twice that of the lifting bodies [Campbell et al. 1997; Murphy et al., 1999; Pamadi & Brauckmann, 1999]. The proposed vehicle characterized by sharp leading edges exhibits the best hypersonic lift-to-drag performance with a hypersonic L/D_{max} of approximately 2.7. This value is comparable to X-34 and X-15 maximum but it must be noted that such L/D ratios for the X-34 and X-15 configurations are a bit misleading. These data are for hypersonic Mach numbers lower than the other wing-body configurations and as such should have lower overall wave-drag and higher lift coefficients. Near-orbital Mach numbers (greater than 20) these L/D values would be closer to the X-20 and Shuttle values. Therefore the proposed vehicle exhibits a L/D ratio 50 per cent larger than other winged bodies and almost three times the L/D for the lifting-body configurations that barely exceeds 1.0.

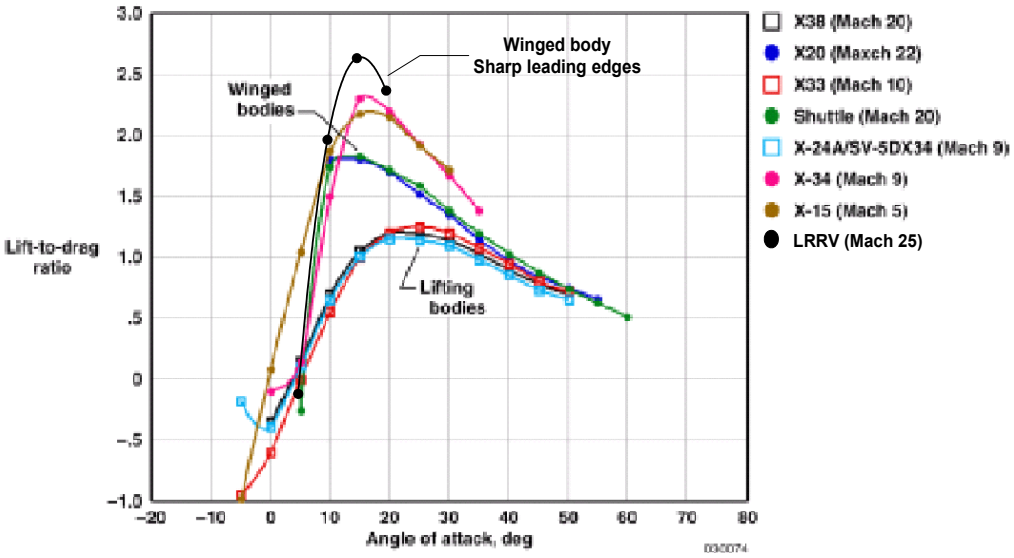

Figure 3-27. Comparison of hypersonic lift-to-drag ratio fordifferent lifting re-entry configurations.

3.2.9 Aerodynamic Efficiency at Landing Conditions

An analysis has been performed to evaluate the aerodynamic performances at landing conditions. Different runs have been made to compute the aerodynamic coefficients at low Mach number (M=0.2) and different angles of attack. The baseline vehicle configuration has been used for computations, not taking into account geometry modifications due to landing gear deployment and/or control surfaces deflections. Furthermore, ground effect has not been taken into account. The importance of ground effect on aerodynamic coefficients for this kind of configurations can be estimated from fig. 3-28, taken from Pamadi & Brauckmann (1999) and concerning the X-34 aerodynamic database development. Figure 3-28 shows the wind tunnel measured incremental aerodynamic coefficients in function of the nondimensional distance from the ground, at different angles of attack. In particular, h is the distance from ground and b is the body length. The effect of a reduced distance from the ground is to increase all aerodynamic coefficients, the increase being greater for larger angles of attack. Figures 3-29, 3-30 and 3-31 show the computed lift, drag and pitch moment coefficients.

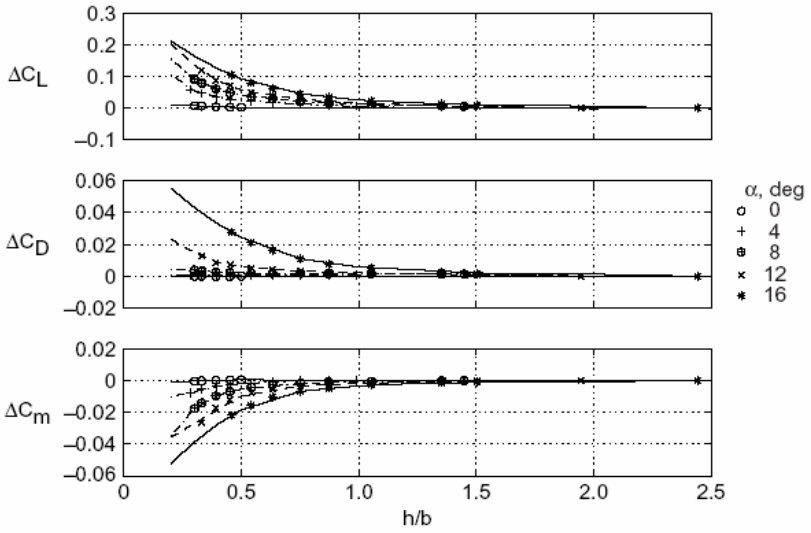

Figure 3-28. Incremental lift, drag and pitching moment coefficients in ground effect for the X-34 vehicle.

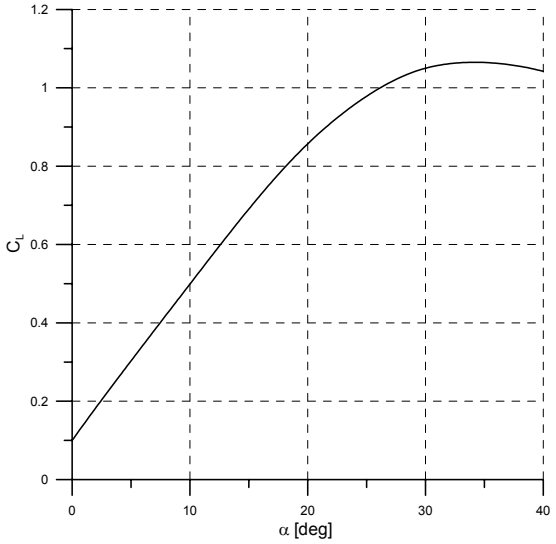

Figure 3-29. Lift coefficient vs. angle of attack (M=0.2)

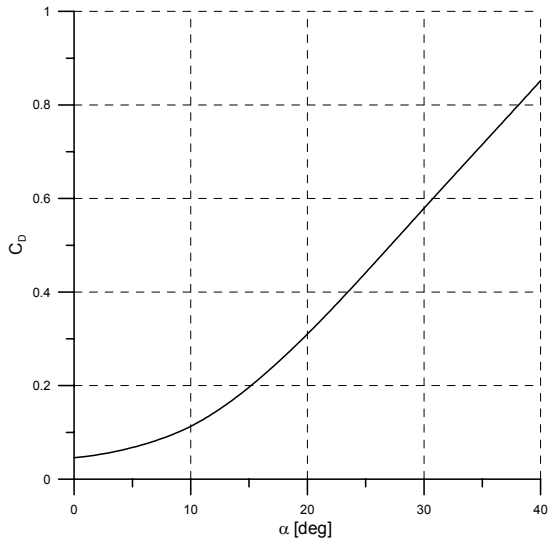

Figure3-30. Drag coefficient vs. angle of attack (M=0.2)

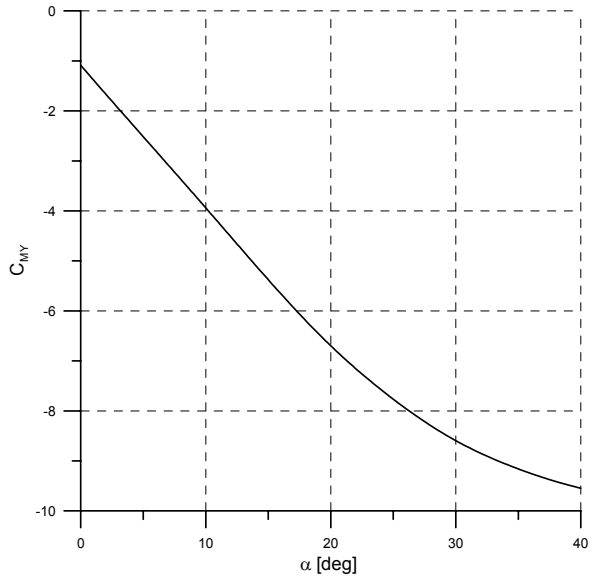

Figure 3-31. Pitch moment coefficient vs. angle of attack (M=0.2, moment center=nose)

It is interesting to note that lift maximum occurs at very high incidence (>30°). This is a known effect on double delta wings, and can be explained by highly stable conical vortices formed on the upper wing surface [Riebe & William, 1956]. Each vortex core has low pressure, so that lift is produced. The stalling mechanism is altered and occurs when vortices burst over upper surfaces.

The computed efficiency is shown in fig. 3-32. To make a comparison the aerodynamic efficiency on the X-34 vehicle, at different Mach numbers and angle of attack, is shown in fig. 3-33. It can be seen that both graphs show, at low Mach numbers, a maximum of efficiency at about 6 deg of angle of attack

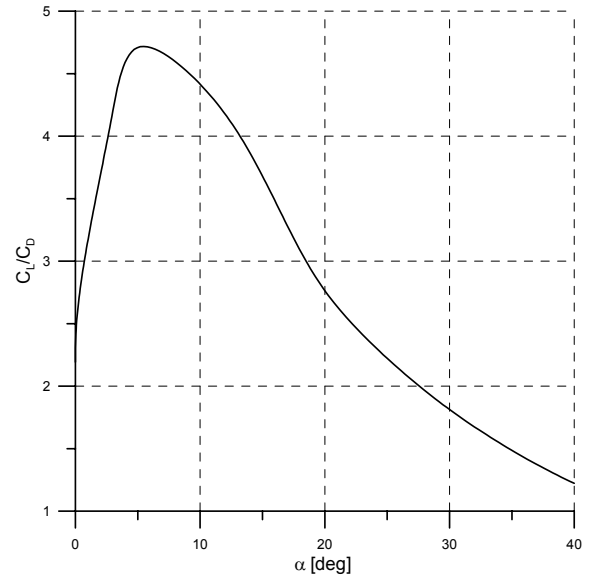

Figure 3-32. Aerodynamic efficiency vs. angle of attack (M=0.2)

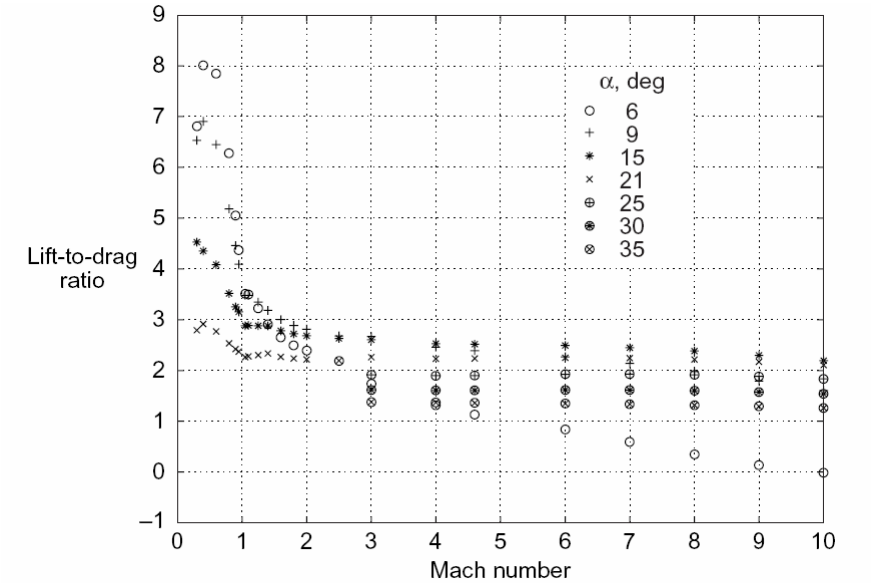

Figure 3-33. Lift to drag ratio for the X-34 vehicle (Ref. 1)

Figure 3-34 shows the computed untrimmed pitching moment coefficient with respect to the vehicle Center of Gravity (CoG). It must be noted that, in these conditions, the vehicle is longitudinally stable up to 20-25°. Furthermore, equilibrium around the pitch axis can only be reached if an appropriate control surface deflection is provided.

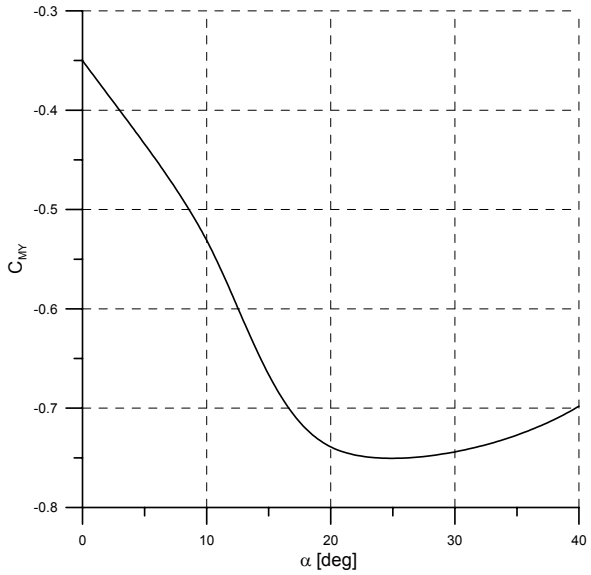

Figure 3-34. Pitch moment coefficient vs. angle of attack around the center of gravity (M=0.2)

3.3 Structure and Thermal Protection

The re-entry vehicle is configured as an hot structure concept with an Ultra High Temperature-Ceramic for the leading edges and a Ceramic-Metallic Composite (CMC) structure for the wings, fins and fuselage. The body structure consists of γ Titanium-Aluminid (γ-TiAl) titanium for wing and fuselage frames and spars and SiC/SiC for the fuselage and wings hull. (fig. 3-35).

The pressurized crew compartment and unpressurized compartment for the equipment in the fuselage are a separate aluminum shell suspended in the body and insulated. The body flap and elevons are configured as the wing γ-TiAl for the spars and SiC/SiC for the skin.

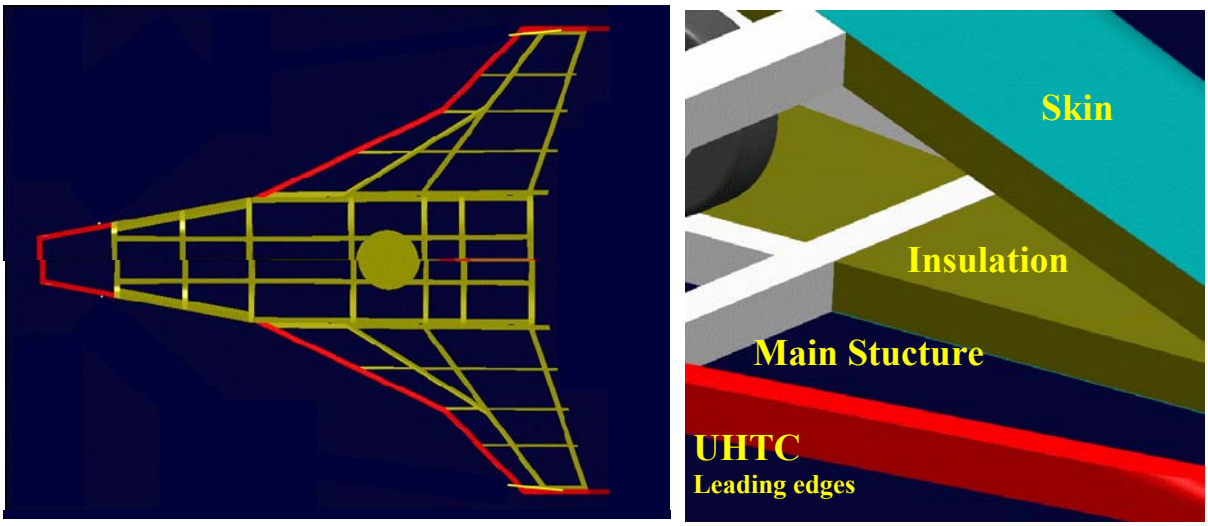

Figure 3-35. Vehicle frame and thermal and structure detail.

3.4 Summary and Comments

A vehicle baseline has been identified following the requirements indicated in the previous chapter and a preliminary design has been carried out in order to identify the materials for structure and thermal protection system together with the internal configuration of the vehicle. Aerodynamic coefficients (lift, drag and pitching moment) on the complete vehicle configuration have been computed at different angles of attack, and different Mach numbers (from low subsonic to hypersonic regimes). It is shown that the lift coefficient, in the investigated range of angles of attack, is almost linear with α in the subsonic regime, and approaches a quadratic dependence at very high Mach numbers in the hypersonic regime. It is further shown that the pitching moment coefficient has a linear dependence on lift coefficient.

Results show that, at higher altitudes along the re-entry trajectory where Reynolds number is sufficiently low, viscous effects cannot be neglected. An increasing of the drag coefficient up to 30% has been computed, while their influence on lift and pitching moment coefficients is negligible.

The aerodynamic efficiency of the baseline vehicle configuration at hypersonic conditions has been compared to those of other lifting re-entry vehicle showing the best performances. This parameter has been evaluated with satisfactory result at landing conditions, too.

References

Anderson J. D. Jr, "Introduction to Flight", Mc Graw-Hill Company, New York, 2001.

Anderson J. D. Jr., "Hypersonic and High Temperature Gas Dynamics", American Institute of Aeronautics and Astronautics, 2000, pp. 271-280.

Ashley H, Landahl M., *Aerodynamics of Wings and Bodies*, Dover Publications, Inc., August 1985.

Campbell, C., and Caram, J., Berry, S., DiFulvioi, M., Horvath, T. "Overview of the X-38 Hypersonic Wind Tunnel data and Comparisons with Numerical Results," AIAA paper 97-0576. Presented at the 35th Aerospace Sciences meeting, Reno, NV, January 1997.

Encyclopedia Astronautica, "X-23 (SV-5D) Prime", http://www.astronautix.com/craft/prime.htm

"Fluent 6.2 User's Guide", Fluent Inc., Lebanon, NH, USA, 2004.

Franklin, Arthur E., and Lust, Robert E., *Investigation of the Aerodynamic Characteristics of a 0.067-Scale Model of the X-15 Airplane (Configuration) at Mach Numbers of 2.29, 2.98, and 4.65*, NASA/TMX- 38, November 1959.

Janovsky, R., Tausche, M., Scheper, M., Orth, M., Monti, R., Savino, R. " Spaceplane – A new way for atmospheric re-entry?",1st International ARA Days. Atmospheric Re-entry Systems, Missions and Vehicles, July 3-5, 2006, Arcachon, France.

MacConochie, I.O. and Klich, P.J., Techniques. for the Determination of Mass Properties of Earth-To-. Orbit Transportation Systems, NASA Technical Memorandum 78661, 1978.

Murphy, K. J., Nowak, R. J., Thompson, R. A., andHollis, B. A., "X-33 Hypersonic Aerodynamic Characteristics," AIAA Paper 99-4162. Presented at the Atmospheric Flight Mechanics Conference, Portland, OR, August, 1999.

Mort, Kenneth W., and Falarski, Michael D., *Full-Scale Wind-Tunnel Investigation of the Aerodynamic Characteristics of the X-24A Lifting Body Aircraft*. NASA/TN-D-5932, August 1970.

Orbiter Operational Aerodynamic Data Book, Boeing, Human Space Flight and Exploration, Huntington Beach, CA, Boeing Document STS85-0118 CHG 9, 2000.

Pamadi, B. N., and Brauckmann, G. J., "Aerodynamic Characteristics and Development of the Aerodynamic Database of the X-34 Reusable Launch Vehicle." Paper presented at the International Symposium on Atmospheric Re-entry Vehicles and Systems Conference, March 16-18, 1999, Arcachon, France.

Papadopoulos P, Venkatapathy E, Prabhu D, Loomis MP, Olynick D. 1999. Current grid generation strategies and future requirements in hypersonic vehicle design, analysis, and testing. Appl. Math. Model 23:705–35

Riebe, J.M., William C., *Low-Speed Stability Characteristics of a Cambered-Delta-Wing Model*, NACA RM-L55L21a, 1956.

Saltzman, Edwin J., Preliminary Full-Scale Power-Off Drag of the X-15 Airplane for Mach Numbers 0.7 to 3.1, NASA/TM-X-430, December 1960, Declassified, April12, 1961.

Savino R., Paterna D., "Blunted Cone-flare in Hypersonic Flow", Computers & Fluids, N. 34, pp. 859-875, 2005.

Van Dyke M. D., "A Study of Hypersonic Small-Disturbance Theory", NACA TN 3173, 1954.

Weiss J. M., Maruszewski J. P., and Smith W. A., "Implicit Solution of Preconditioned Navier-Stokes Equations Using Algebraic Multigrid". AIAA Journal, 37(1), pp. 29-36, 1999.

CHAPTER 4

RE-ENTRY TRAJECTORIES EVALUATION

4.1 Introduction

In order to determine the angle of attack (α) time profile necessary to follow a trajectory at constant, prescribed, heat flux $\dot{q}_s$ the equations of a planar trajectory for an un-powered vehicle over a non rotating spherical planet have been solved under the assumption of 3 d.o.f. In this chapter a sensitivity analysis has been performed, too, to find the conditions at the entry interface that allows the vehicle to re-entry, together with the ΔV required for de-boost.

4.2 Trajectory Code Description

In order to compute entry trajectories, the dynamic equations of a spacecraft, considered as a point mass, with three degrees of freedom have been numerically solved. The vehicle is supposed to fly inside a planetary atmosphere in convenient frames of reference, shown in figure 1. The description of the reference system can be found in Ashley (1974).

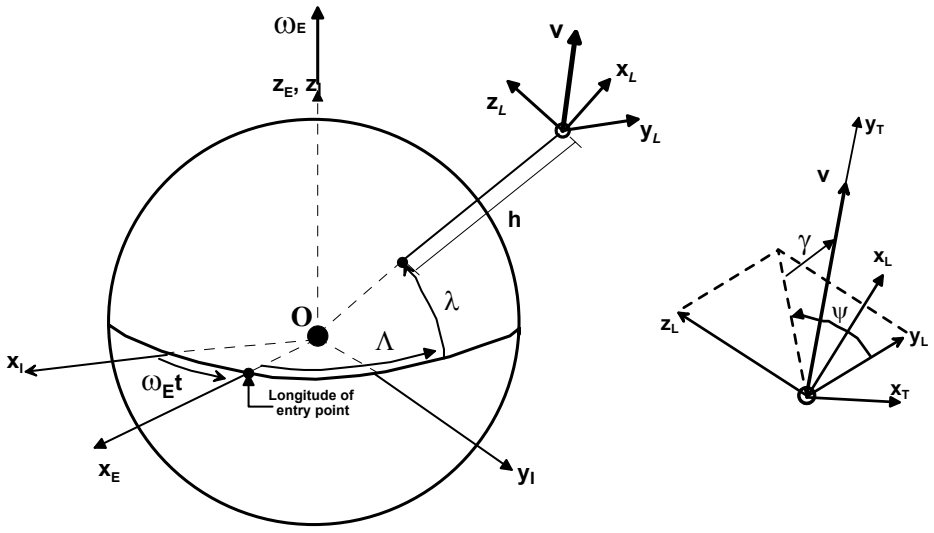

Figure 4-1. Atmospheric entry reference system and nomenclature

Thus, for a planar trajectory of an un-powered vehicle over a rotating spherical planet, the equations of motion of a point mass, read:

$$\frac{dv}{dt} = -\frac{D}{m} - g\sin\gamma + \omega_E^2 r\cos\lambda\left[\sin\gamma\cos\lambda - \cos\gamma\sin\psi\sin\lambda\right] \tag{1}$$

$$v\frac{d\gamma}{dt} = \frac{L\cos\beta}{m} - \left(g - \frac{v^2}{r}\right)\cos\gamma + 2\omega_E\cos\psi\cos\lambda + \omega_E^2 r\cos\lambda\left[\cos\gamma\cos\lambda - \sin\gamma\sin\psi\sin\lambda\right] \tag{2}$$

$$v\frac{d\psi}{dt} = \frac{L\sin\beta}{m} - \frac{v^2}{r}\cos\gamma\cos\psi\tan\lambda - 2\omega_E\left(\sin\lambda - \tan\gamma\sin\psi\cos\lambda\right) - \omega_E^2 r\frac{\cos\psi\sin\lambda\cos\lambda}{\cos\gamma} \tag{3}$$

while the equations for the altitude (z), and the equations for the longitude (Λ) and latitude (λ) coordinates are:

$$\frac{dz}{dt} = v\sin\gamma \tag{4}$$

$$\frac{d\Lambda}{dt} = \frac{v\cos\gamma\cos\psi}{r\cos\lambda} \tag{5}$$

$$\frac{d\lambda}{dt} = \frac{v\cos\gamma\sin\psi}{r} \tag{6}$$

The first three equations are the Newton's equations of motion for the spacecraft moving at a distance *r* from the planet center. In the equations (2-3) β is the bank angle.

Besides the state and control variables, the equations depend on different vehicle and environmental parameters, such as the vehicle mass, the reference surface, the vehicles positions, the aerodynamic forces and the gravitational acceleration:

$$D = \frac{1}{2}\rho v^2 C_D S_r \tag{7}$$

$$L = \frac{1}{2}\rho v^2 C_L S_r \tag{8}$$

$$g = g_o\left(\frac{R}{r}\right)^2 \tag{9}$$

For the Earth atmosphere, density ρ, pressure p, and temperature T are based on the 1976 U.S. Standard Atmosphere Model.

The six first order nonlinear ordinary differential equations (eq. 1-6), with the relevant planetary and spacecraft physical properties, are solved by numerical integration at discrete time-steps. The results provide the re-entry trajectory for a lifting space vehicle, according to the chosen strategy, and to the specified boundary conditions.

In the present computations the Earth rotation has been neglected (Λ coincides with the down-range angle and λ with the cross-range). This assumption leads to negligible errors in the evaluation of the heat fluxes and of the aerodynamic forces.

4.2.1 Approximate Aerothermal Analysis

An approximate evaluation of the heat fluxes, which allows to identify the entry corridor and/or to achieve a constant heat flux entry strategy, may be accomplished by suitable engineering formulas.

The engineering formula employed for the evaluation of the stagnation point convective heat flux, in the hypersonic regime ($M_\infty >> 1$), is provided by Tauber (1987):

$$\dot{q}_s = K_z \sqrt{\frac{\rho_\infty}{R_N}}\ v_\infty^3\ \left(1 - 0.18\sin^2\Phi\right)\cos\Phi \tag{10}$$

where K_z=1.29x10^{-4} if metric units are used and Φ is the sweep angle of the wing.

For the evaluation of the surface heat flux on the vehicle windside for a surface point at a distance x from the tip, an approximate formula for the flat plate at an angle of attack α≠0 has been considered [Tauber, 1987]:

$$\dot{q}_{FP} = 2.53x10^{-5}\ \rho_\infty^{0.5} V_\infty^{3.2} (\cos\alpha)^{0.5}\ \sin\alpha\ x^{-0.5}\left(1 - \frac{h_w}{H_0}\right) \tag{11}$$

4.2.2 Entry Code Validation

The trajectory code developed has been validated against the Apollo re-entry trajectory computed by NASA [Young & Smith, 1967] and compared with the ASTOS code. Two trajectories were computed for a "nominal" Apollo-type vehicle entering the atmosphere of a spherical Earth at near parabolic velocity.

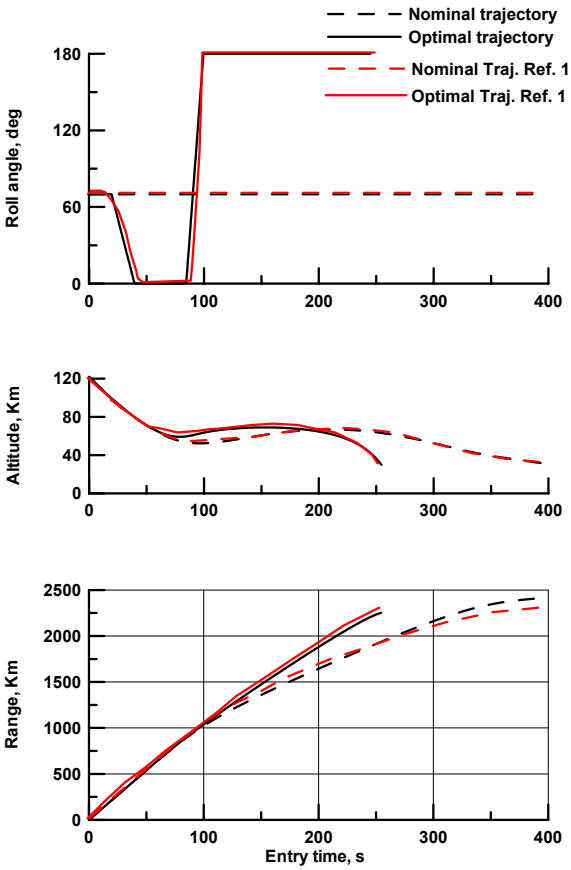

Figure 4-2. Nominal and optimal Apollo re-entry trajectories comparison between present computation and Young &Smith, 1967.

The vehicle considered is characterized by a lift-drag ratio of 0.5 and a ballistic parameter m/C_DS of 322 kg/m^2. Lift modulation is obtained by rolling the vehicle. The nominal initial entry conditions considered are: 1. a non rotating atmosphere, 2. an altitude of 122 km, 3.an entry velocity of 11 km/s and 4. an initial flight path angle of -6.5°.

The final altitude is 30 Km.

Figure 4-2 shows the roll angle control law, the altitude and the range as functions of the flight time. The dashed lines show the nominal trajectories with a constant roll angle of 70°. The solid lines show an optimal trajectory obtained by roll modulation to reduce the entry time of the trajectory . The present computation have been obtained applying the roll angle history obtained by Young and Smith (1967). As can be noted, a good agreement is obtained between the present code and the literature results for both the control laws.

Considering the winged vehicle with a wing loading (m/S) of 80 kg/m^2 another a tre-entry trajectory computation has been compared with the results of the ASTOS code. The trajectory of a vehicle entering the atmosphere of a spherical Earth at orbital velocity is considered.

The initial conditions at an altitude of 120 km are: a velocity of 7.8 Km/s and a flight path angle of -1.1°.

In figure 4-3, the red curves show the trajectory obtained by the in-house code with a constant angle of attack of 20°; the blue curves show the same trajectory obtained by the ASTOS solver. Figure 4-3 shows a good agreement between the two codes, in terms of altitude and downrange history.

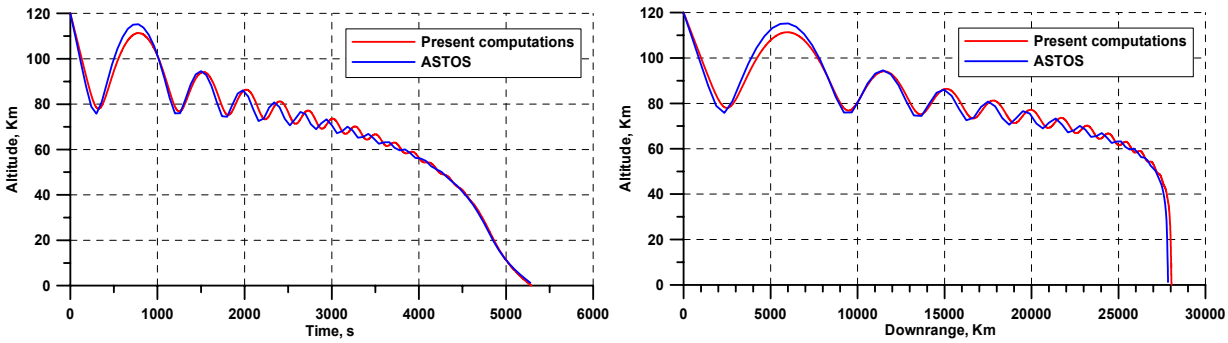

Figure 4-3 – Re-entry from orbit comparison between present computation and ASTOS

In what follows the in-house trajectory solver will be used, which is easily customizable to different control laws, different planets and vehicle models.

4.3 Entry Corridors

A sensitivity analysis has been performed to find the conditions at the entry interface (entry velocity and entry flight path angle) that allows the vehicle to manoeuvre and be able to get onto the low risk, aero thermal limit (i.e. the constant stagnation point temperature).

The assumption is that the initial altitude is 400Km at the orbital speed (7688 m/s) and the wing loading is 80Kg/m2. The angle of attack is modulated in order to enforce the re-entry trajectory to follow a constant stagnation point heat flux (1.7 MW/m2, corresponding to a local radiative equilibrium temperature of 2470 K for a 1.5 cm curvature radius at the nose leading edge, and an emissivity value ε=0.8).

The re-entry manoeuvre consists in decelerating the vehicle by ΔV by means of an impulsive thrust (de-boost) in the opposite direction of the vehicle motion, tangent to the orbit(γ=0°). Varying the de-boost, the condition at the re-entry interface (120Km) in terms of the flight path angle and velocity are shown in fig.4-4.

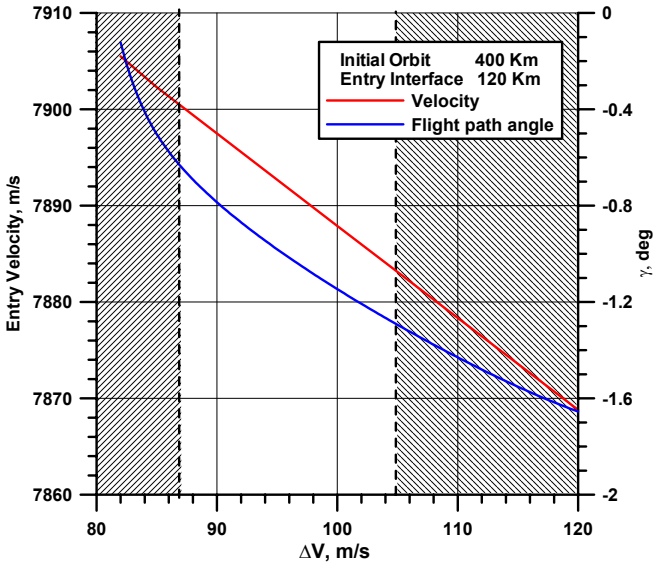

Figure 4-4. Conditions at the entry interface by a single de-boost ΔV

Figure 4-5 shows that the envelope of the possible couples of values for V_e and γ_e able to perform the constant heat flux re-entry are confined:

1. by an upper curve "skip" above which the vehicle will not re-enter and will be bounced back into space.
2. by a lower curve "thermal barrier" below which the trajectory encounters heat flux larger than the maximum allowable by the selected materials (UHTC and structural).

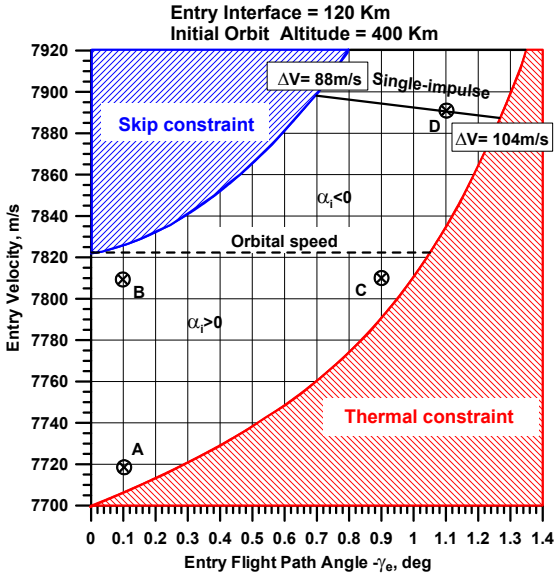

Figure 4-5. Conditions at the entry interface

The envelope shown in fig. 4-5 appears to be sufficiently wide and is divided into two zones corresponding to sub-orbital and super-orbital circular velocity at the re-entry interface(120

Km). For the case of super-orbital velocity an initial negative lift is needed to re-entry, that could be obtained with a negative angle of attack (α_i<0).

For a single de-boost manoeuvre from 400Km (ISS Orbit) values of de-boost ΔV ranging from 88[m/s] to 104 [m/s] are compatible with re-entry corridor constraint(fig.5). Point D of fig. 4-5 (V=7890m/s; γ=-1.1°) is taken to be as nominal condition at the entry interface corresponding to a single de-boost re-entry of ΔV=96m/s. All the other single impulse manoeuvres fall on a straight line(88≤ΔV≤104m/s).

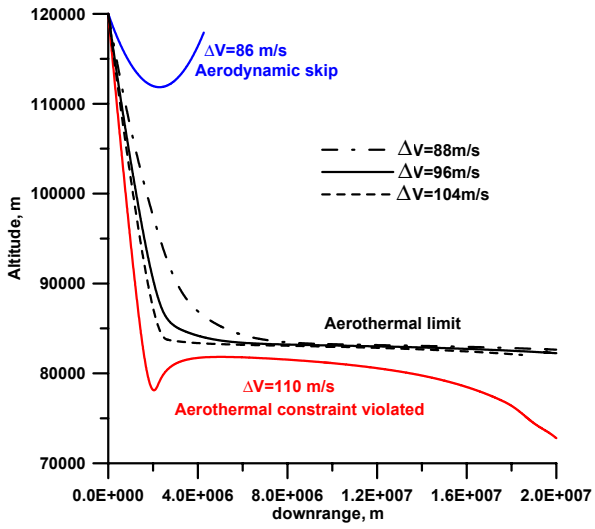

Figure 4-6. Trajectories obtained with different single de-boost ΔV

To get into the envelope of Fig.4-5 two de-boosts must be made; Figure 4-7 shows the trajectories in the altitude/velocity plane corresponding to points A, B, C and D i.e. at the borders of the footprint shown in Fig. 4-5.

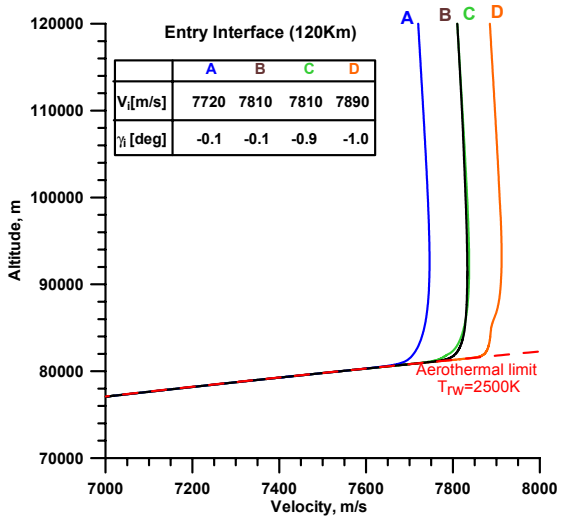

Figure 4-7. Re-entry trajectories

Figure 4-8 shows the time history of the angle of attack vs. altitude along the different trajectories from the re-entry interface to about 80Km.

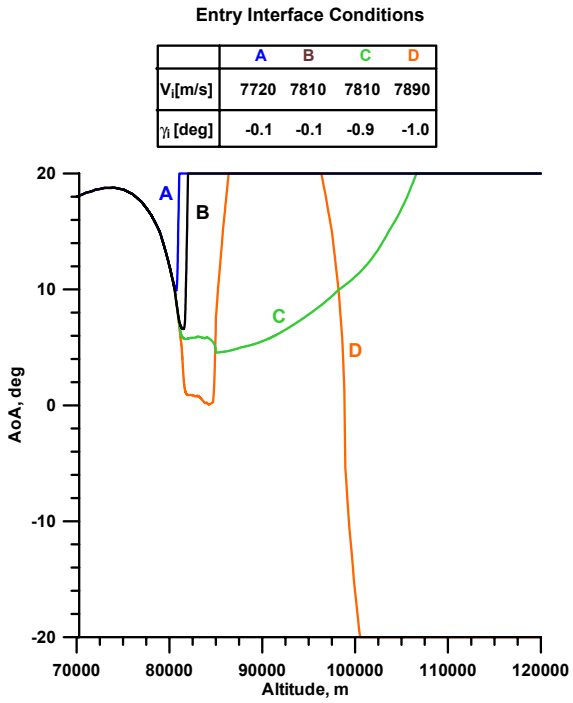

Figure 4-8. Angle of attack necessary to enter the Aerothermal curve (from 120 to 80 Km)

4.4 Computation of Entry Trajectories

The vehicle wing loading considered for computations is 80 Kg/m^2, the aerothermal constraint is 1.7 MW/m^2 corresponding to a local radiative equilibrium temperature at the stagnation point of 2470K. The initial condition at the entry interface (Z=120Km) are V=7890m/s and γ=-1.1°. Figures from 4-9 to 4-20 show the main parameters of the trajectory, comparing the results obtained with the Euler aerodynamic dataset with the viscous aerodynamic dataset. The main difference between the two cases is the re-entry time, which is reduced by about 1000s if the viscous drag is taken into account.

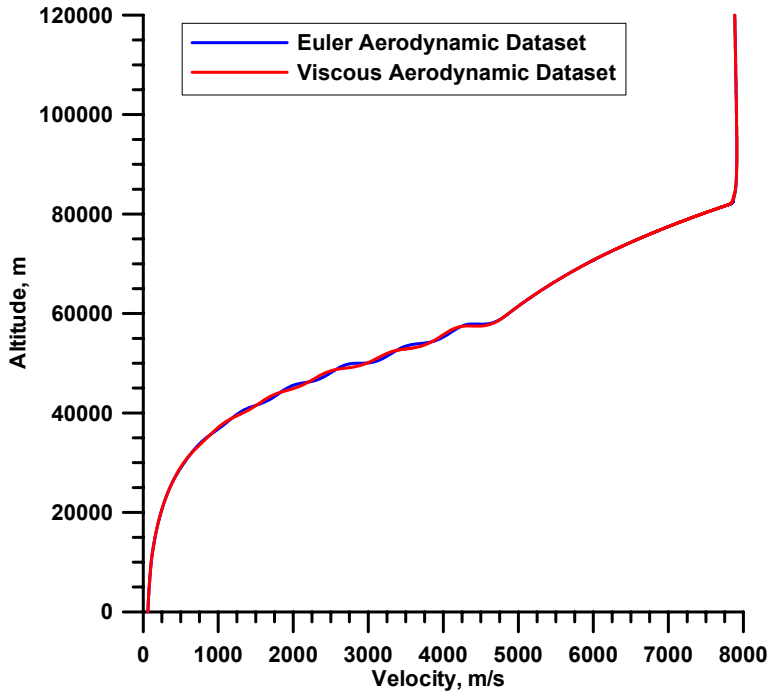

Figure 4-9. Nominal trajectory in Z-V plane

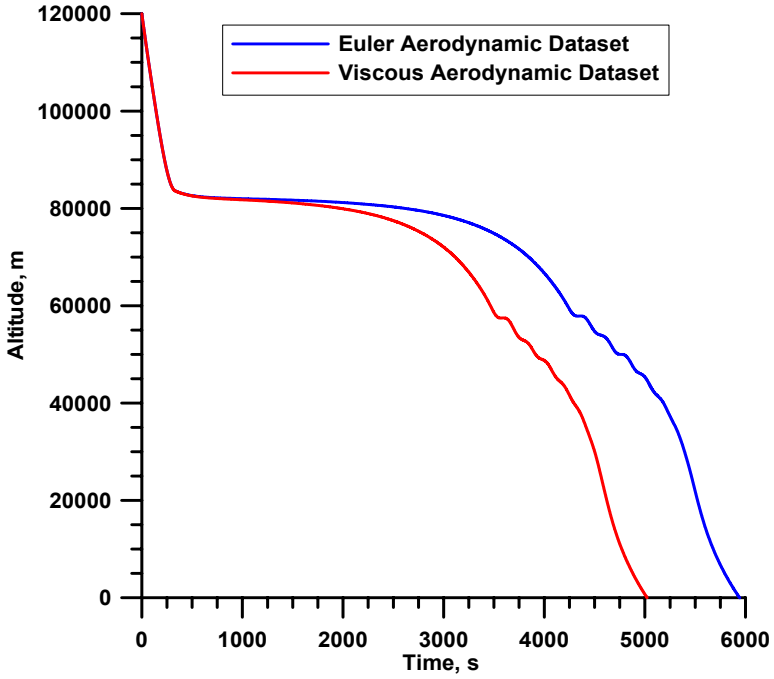

Figure 4-10. Nominal trajectory in Z -t plane

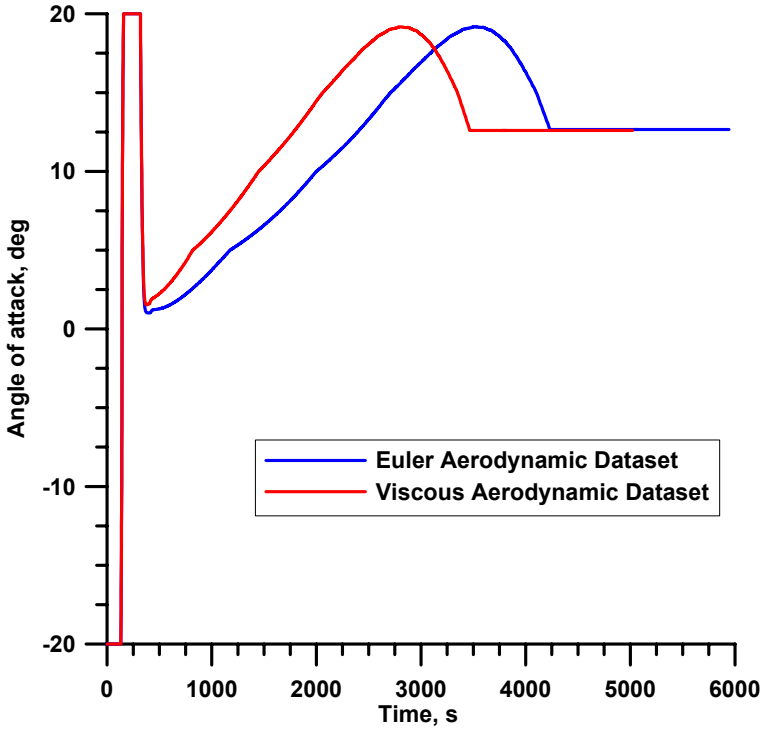

Figure 4-11. Angle of attack evolution along nominal trajectory

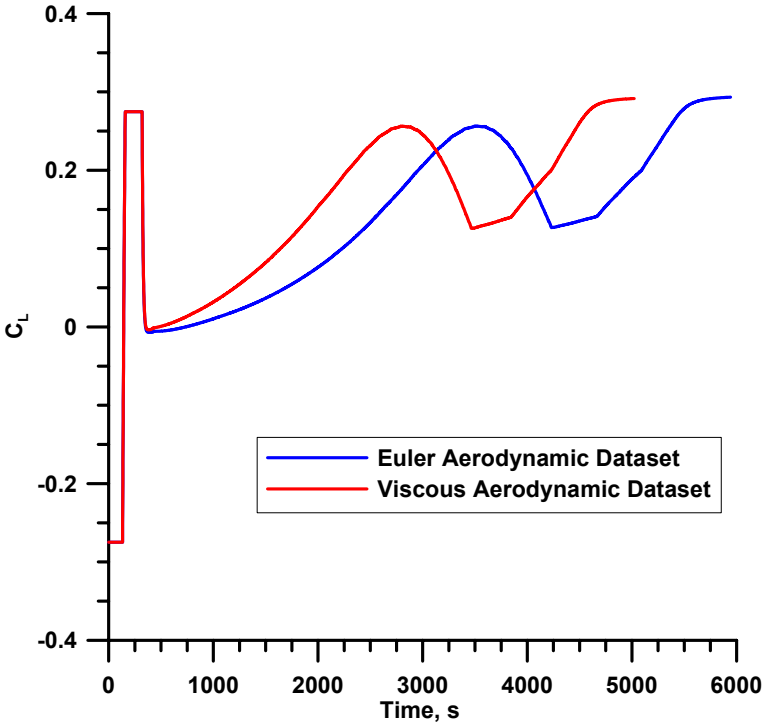

Figure 4-12. Lift coefficient evolution along nominal trajectory

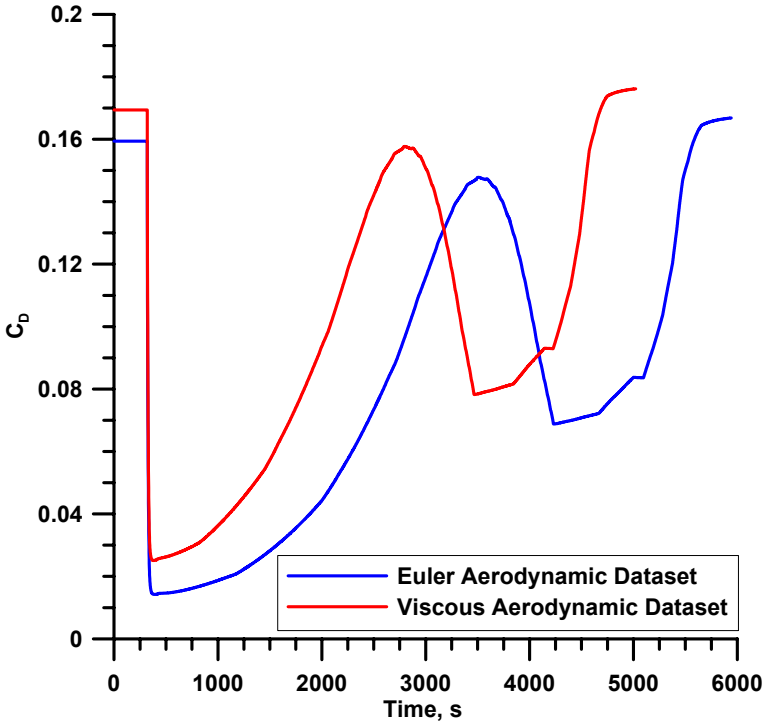

Figure 4-13. Drag coefficient evolution along nominal trajectory

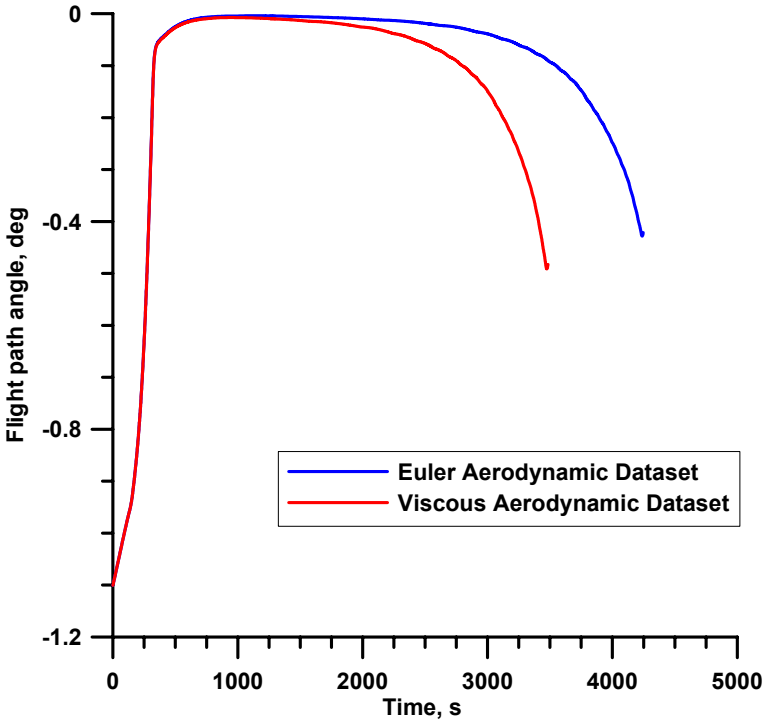

Figure 4-14. Flight path angle evolution along nominal trajectory

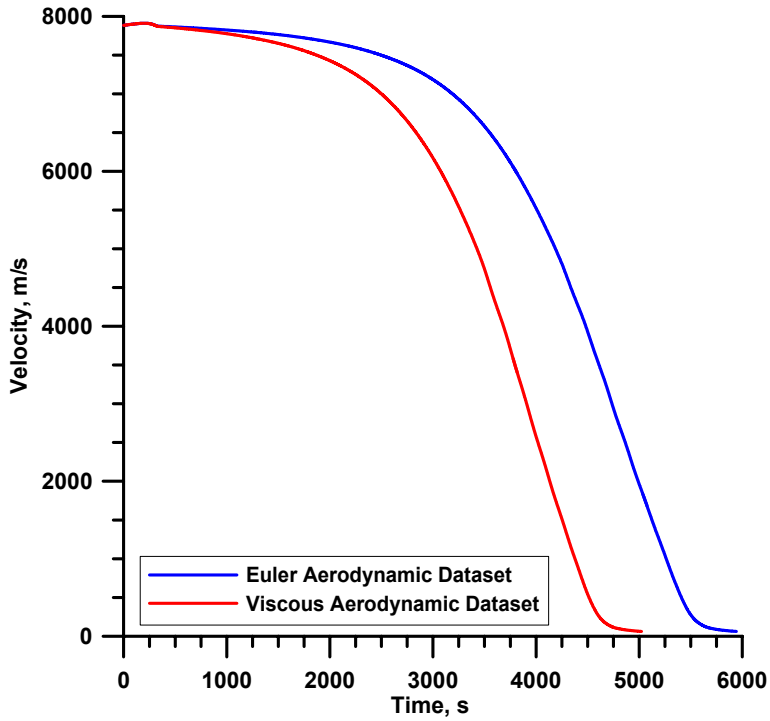

Figure 4-15. Velocity evolution along nominal trajectory

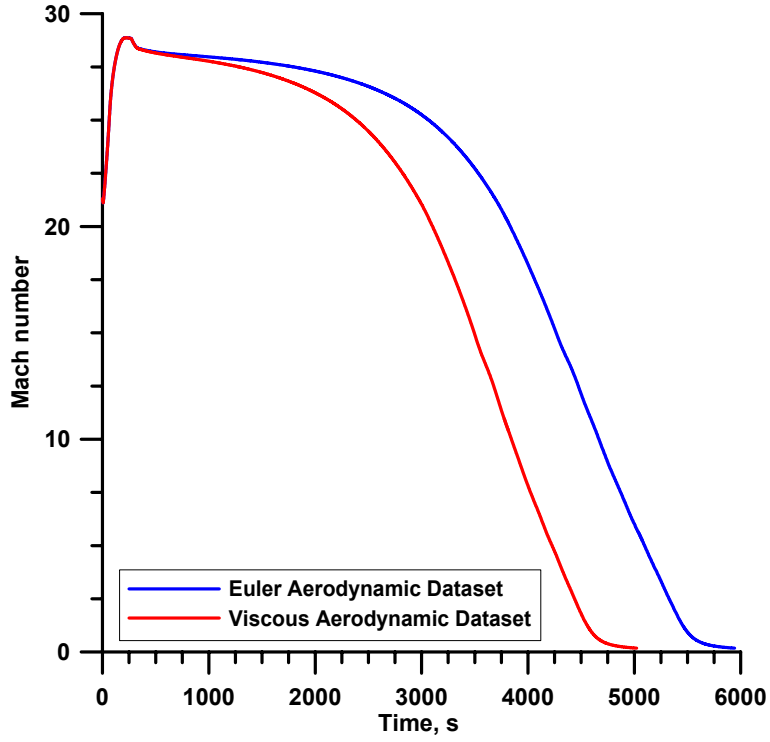

Figure 4-16. Mach number evolution along nominal trajectory

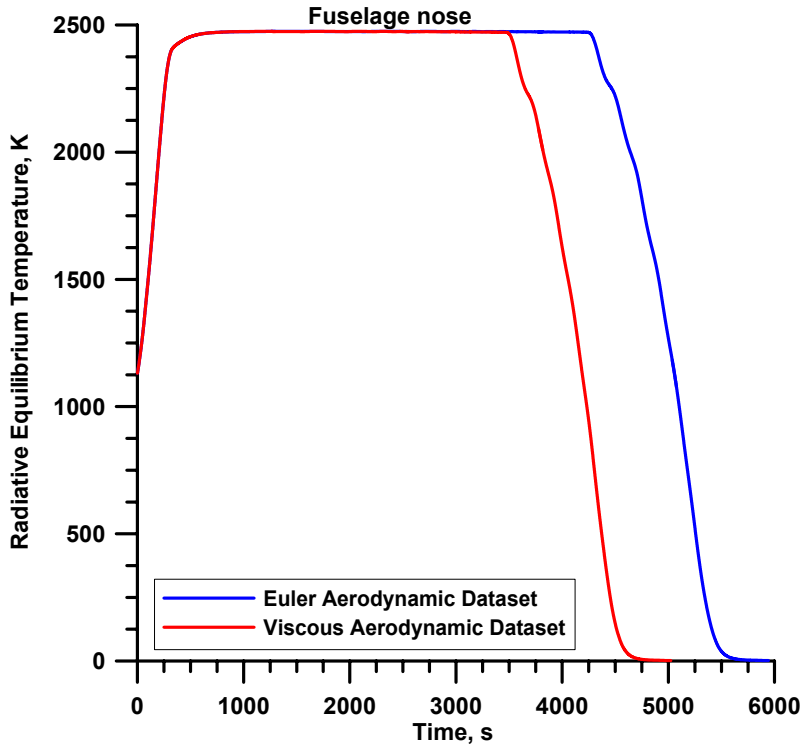

Figure 4-17. Radiative equilibrium stagnation point temperature evolution along nominal trajectory

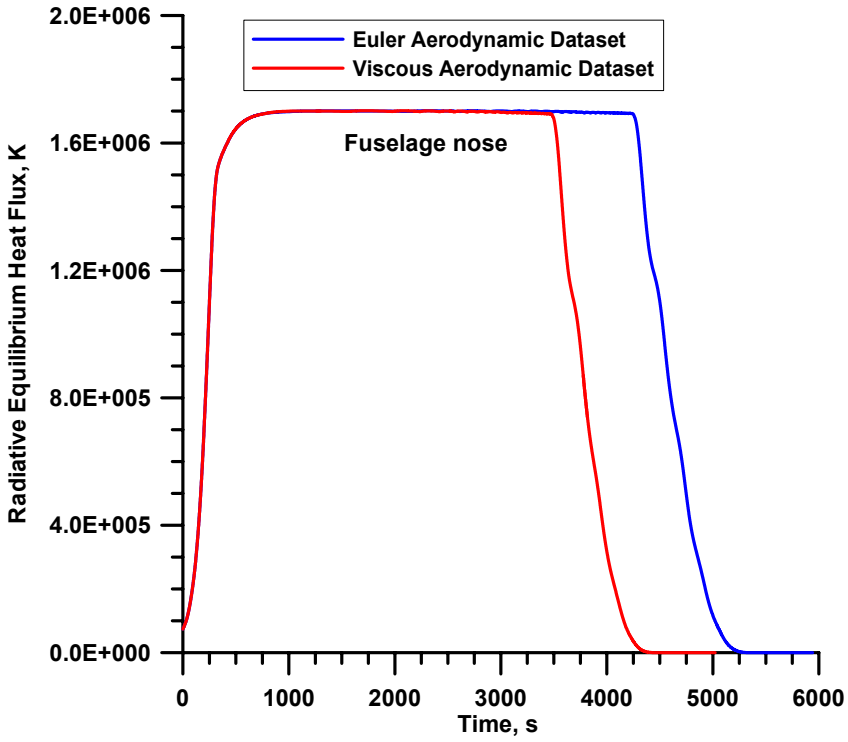

Figure 4-18. Radiative equilibrium stagnation point heat flux evolution along nominal trajectory

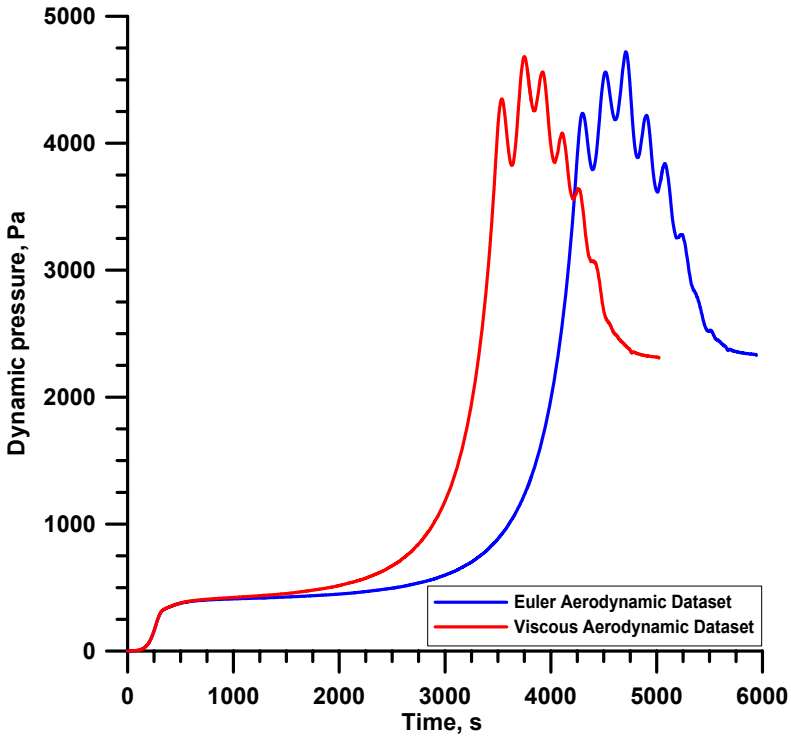

Figure 4-19. Dynamic pressure evolution along nominal trajectory

4.5 Effect of Aerodynamic Bank Manoeuvre

Vehicle lift vector and angle of attack are the two primary control parameters used by the vehicle guidance . Controlling the direction of the vehicle lift vector is the primary control mechanism available to achieve the desired landing point. A combination of angle of attack modulation and vehicle roll ensure that the vehicle will dissipate the proper amount of energy and arrive at the desired landing site location.

Figure 4-20 demonstrates how lift vector control results by rolling the vehicle about the relatively velocity vector.

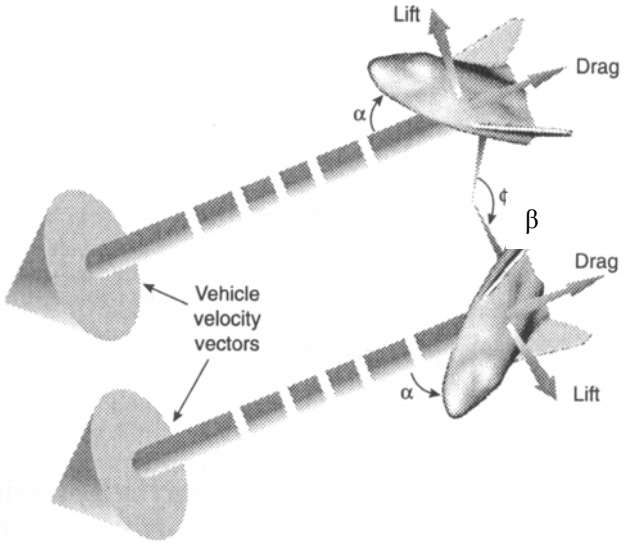

Figure 4-20. Bank manoeuvre.

Rotating the lift vector out of the vertical plane defined by the position and velocity of an angle β, called bank angle, the vehicle can fly out of the initial plane. This manoeuvre is necessary to create an envelope of the possible landing points.

A simplified formula [Eggers, 1959] shows how higher is the aerodynamic efficiency higher is the cross-range and that the maximum cross-range is obtained for a bank angle of 45°.

$$c = R\left(\frac{\pi^2}{48}\right)\left(\frac{L}{D}\right)^2 \sin 2\beta$$

This is intuitively reasonable because the lift vector is evenly divided between turning (90°) and staying in the air (0°) long enough to realize the result of the turn.

It must be pointed out that the bank manoeuvres have a certain effect on downrange. In fact, considering the equilibrium glide phase($\gamma<<1$) for a vehicle in a planar flight, the downrange can be written as:

$$d = \frac{1}{2}R\left(\frac{L}{D}\right)\ln\left[\frac{1}{1-V_e^2/gR}\right]$$

the bank manoeuvre can be considered as a reduction of sustaining lift, i.e. L must be substituted by Lcos(β).This implies that a bank angle of 30° reduces of about the 15% the downrange while a bank angle of 60° halves it. All these results are shown in figure.

For this reason it is fundamental to identify the optimum bank angle in such a way that the downrange is not unduly reduced and the cross range is that necessary for the appropriate landing point.

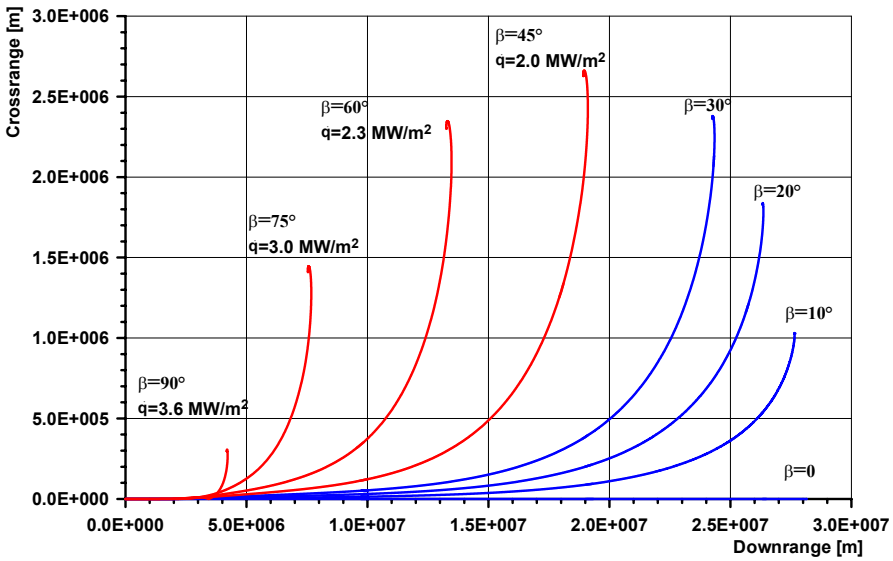

Figure 4-21. Crossrange versus downrange for different bank angle.

Considering the re-entry strategy, the vehicle flies for a part of the trajectory along a constant heat flux curve. To follow this path the vehicle needs a certain lift coefficient.

As stated above the effect of the bank angle is a reduction of sustaining lift so the introduction of a bank manoeuvre affects the maximum stagnation point heat flux achievable by the vehicle as reported in figure. For the considered vehicle and the re-entry interface conditions the thermal constraint of 1.7 MW/m^2 is achievable with a bank angle up to 30° (blue curve). To obtain the maximum cross range the value of the maximum stagnation point heat flux must be increased to 2.0 MW/m^2.

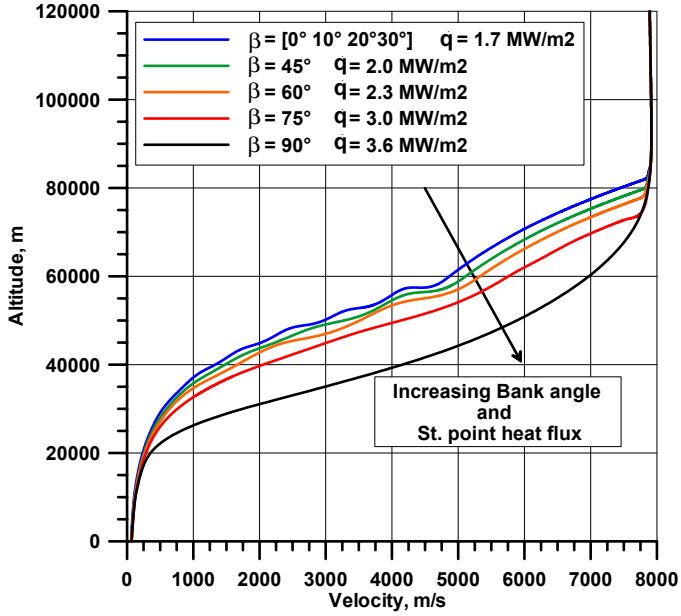

Figure 4-22. Re-entry trajectories for different constant bank angle.

4.6 The ground track

All these data are referred to non rotating earth computations, i.e. the vehicle are flying on a circle and the re-entry trajectory is independent from the initial orbit inclination.

When considering earth rotation, it is interesting to plot the ground track of the re-entry vehicle.

Figure 4-23 and 4-24 show the ground tracks obtained for a re-entry vehicle docked to the ISS, i.e. to an initial condition of 400 km and of an initial orbit inclination of 51°, when a de-boost of 97 m/s is fired with the station at 51° of latitude and 30° East of longitude.

The figure 4-23 shows the difference due to the bank angle. It is interesting to note that the effectiveness of bank angle manoeuvre starts at an altitude lower of 80 km where the density and therefore the aerodynamic forces, in particular the lift become significant.

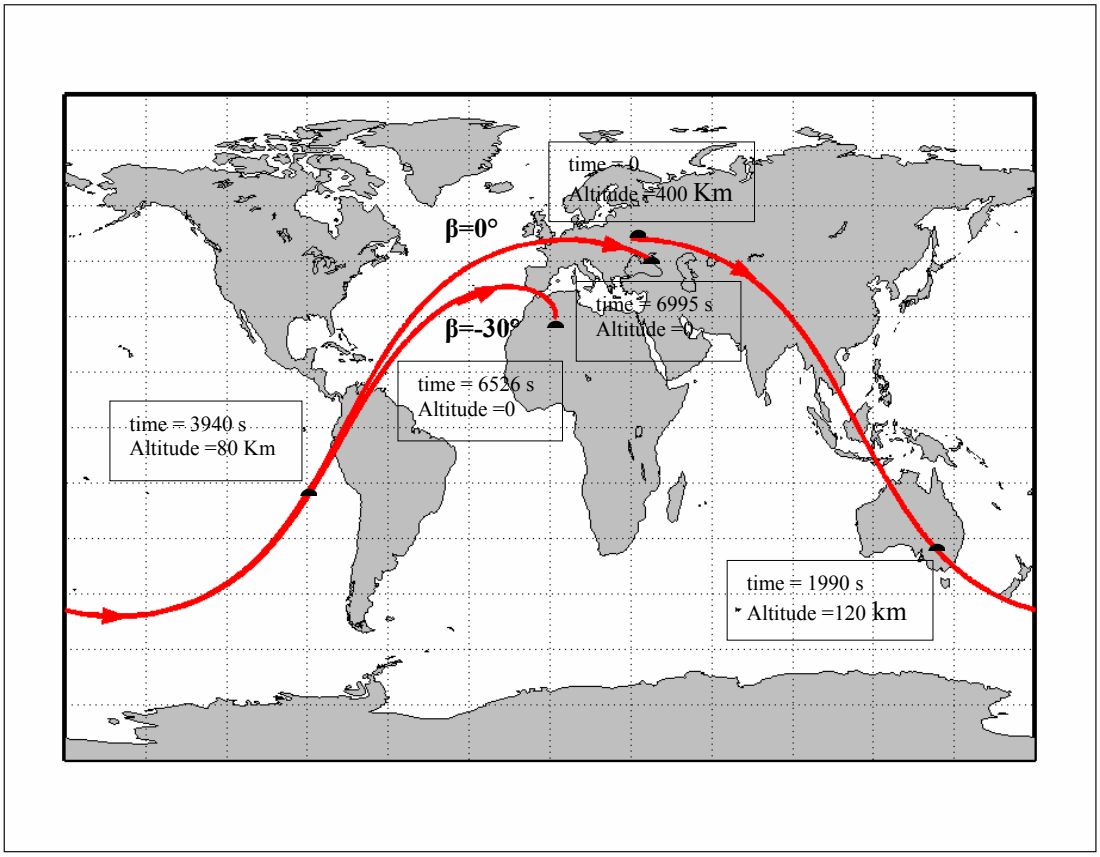

Figure 4-23. Effect of the bank on the ground track.

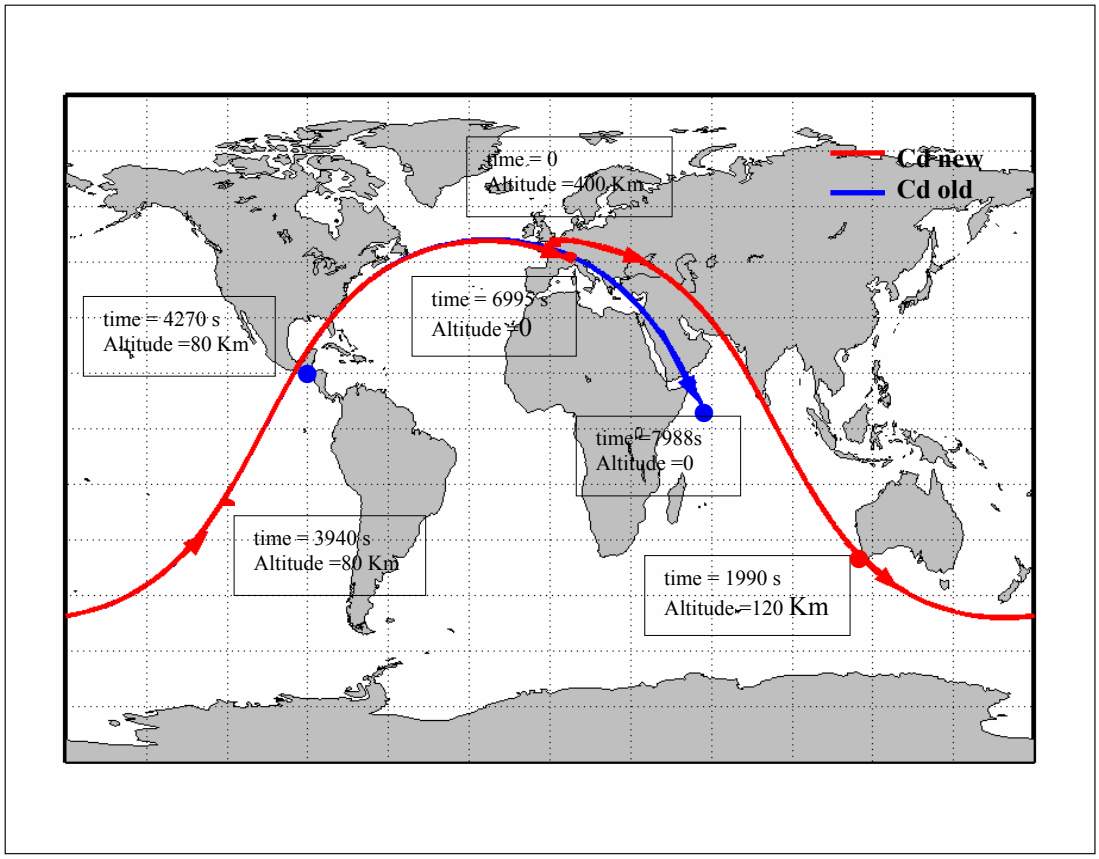

Figure 4-24. Effect of the aerodynamic database on the ground track.

Figure 4-24 shows the effect of the two different aerodynamic database on the re-entry trajectory. Also by this visualization it is underlined the effect of an increase of the drag in the reduction of the downrange.

4.7 Comparison with the Space Shuttle re-entry.

Considering the different vehicle parameter and re-entry strategy of the Space Shuttle, it is interesting to compare the main trajectory data of the two type of re-entry.

A first analysis can be done taking into account the strong difference of the two re-entry vehicles, the Space Shuttle has a wing loading of 350 kg/m^2 more than four times of the considered re-entry vehicle and a hypersonic aerodynamic efficiency slightly larger than, less than the half of proposed vehicle. For this reasons the Space Shuttle in the hypersonic part of flight re-enters at an angle of attack of 40° and it deeps in the atmosphere less than a capsule but much more than a glider. Figure 4-25 shows the main difference in the trajectories.

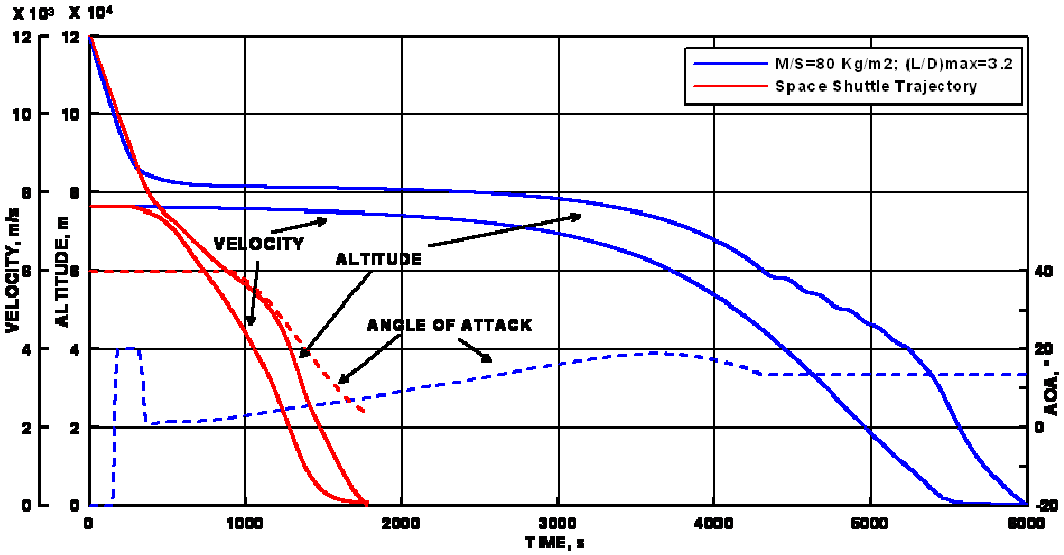

Figure 4-25. Trajectories comparison.

The peak of acceleration level for the Space Shuttle is twice of the high lift re-entry vehicle as shown in figure 4-26. The stagnation point heat flux is obviously lower for the Shuttle considering the radius of curvature of 0.6 m respect to the very sharp nose of the proposed vehicle.

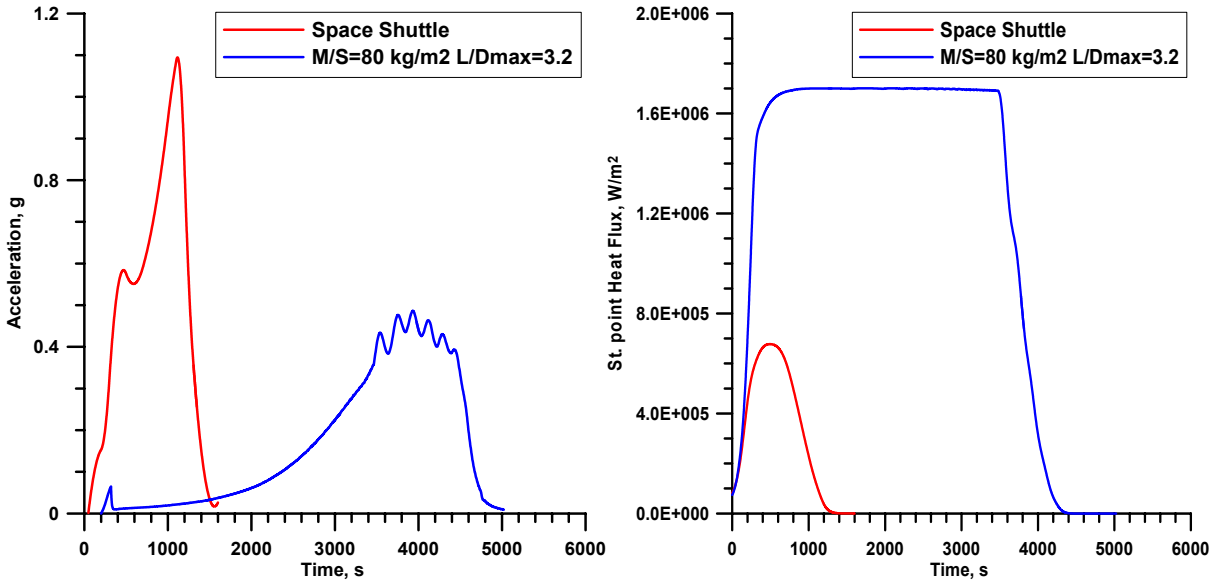

Figure 4-26. Acceleration and Stagnation point heat flux comparison.

In order to compare the mechanical load a figure of merit can be defined. The average mechanical loads transferred to the vehicle can be evaluated as:

$$\bar{q}_{free-stream} = \frac{\int \frac{1}{2}\rho V^2 dt}{\Delta t}$$

Figure 4-27 shows the comparison between the dynamic pressure profile for the proposed and the Shuttle trajectories.

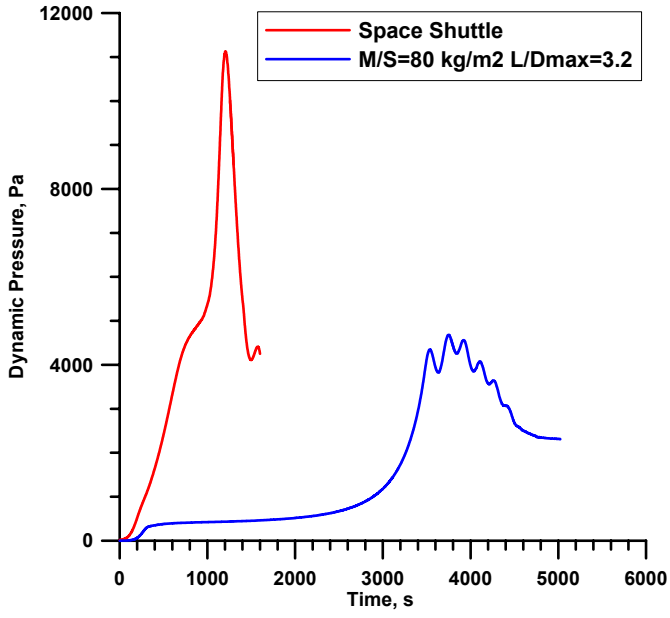

Figure 4-27. Dynamic pressure comparison.

The maximum dynamic pressure along the proposed nominal trajectory is only 4500 Pa and occurs at an altitude of about 55Km , whereas for the Shuttle trajectory it is 11000 Pa, occurring at an altitude of 47 Km. The result, in term of the average mechanical load, is 1330 Pa for the proposed trajectory and 5750 Pa, i.e. four times higher, for the Shuttle trajectory.

4.8 Summary and Comments

A numerical code has been developed in order to compute the re-entry trajectory for a point mass with three degree of freedom and it has been validated through comparison with two different codes.

A sensitivity analysis on the re-entry corridor and on the conditions at the re-entry interface has been carried out.. A de-boost of 96m/s has been evaluated for the re-entry from the ISS orbit that gives a velocity of 7890m/s and a flight path angle of -1.1° at the re-entry interface.

Preliminary computations on the effect of a constant bank angle have shown that a re-entry trajectory with a bank angle of 30° results in a cross range of about 3.6 $x10^6$m, i.e. about one tenth of the earth circumference.

The sensitivity of the trajectory with respect to the aerodynamic dataset has been investigated. The nominal re-entry trajectory has been computed with both Euler and Viscous aerodynamic dataset and the results show that the only parameters affected are the re-entry time, which is reduced of about 1000s, and the downrange, which is reduced of about the 20%.

Finally a comparison with the re-entry trajectory of the Space Shuttle has been executed in order to compare some of the typical re-entry parameters to underline the advantage of the proposed strategy.

References

Ashley H., “Engineering analysis of flight vehicles”, Dover, New York, 1974.

ASTOS, aerospace Trajectory Optimization software, Software Package, Institute of Flight Mechanics and Control, University of Stuttgart, Germany, 2002.

Eggers, A. J., “The possibility of a safe Landing”, Space Technology, edited by H.S. Seifert, Wiley, New York, Chap. 13, 1959

Monti, R.; Paterna, D.M. “A low risk re-entry: looking backward to step forward”, Aerospace Science and Technology, Volume 10, Issue 2, 1 March 2006, Pages 156-167.

Regan, F., Anandakrishnan, S. M., Dynamics of Atmospheric Re-entry, American Institute Of Aeronautics and Astronautics Inc., Washingthon D.C.,1993.

Tauber M.E., “ A Review of High Speed Convective, Heat-Transfer Computation Methods, NASA Technical Paper 2914, 1989.

”U.S. Standard Atmosphere 1976”, NASA, NOAA, U.S. Air Force, Washington D.C., 1976.

Vinh, N. X., Hypersonic and Planetary Entry Mechanics, The University of Michigan Press, Ann Arbor, 1980.

Young J. W., Smith Jr, R. E., “Trajectory optimization for an Apollo-type vehicle under entry conditions encountered during lunar return”, NASA Technical Report R - 2 5 8, 1967.

Wiesel, W., Spaceflight Dynamics, The Mc Graw-Hill Companies Inc., Boston, 1997.

CHAPTER 5

AEROTHERMAL LOAD AND THERMAL PROTECTION SYSTEM

5.1 Introduction

This chapter is devoted to the analysis of the aerothermal load of the most stressed part of the vehicle by a thermal point of view: the fuselage nose and the wing. This analysis will be performed by a CFD code. Following the thermal load computation different thermal design of the nose and wing leading edges will be proposed.

5.2 Evaluation of Heat Fluxes for the Most Critical Re-entry Conditions

A steady CFD analysis at an altitude of 60 Km and a Mach number of 15, at different angles of attack (0 and 20°) has been carried out to identify the aero-thermal loads.

The Navier-Stokes equations have been solved with a finite volume numerical code. The model is based on the assumption of perfect gas. In this way one can speed up the computation, obtaining accurate results, due to the fact that for a sharp leading edge and for the considered flight conditions the flow is almost chemically frozen in the shock layer [Monti et al., 2005].

The numerical computations have been performed on the front part of the fuselage(nose) and on the double delta wing.

5.2.1 Fuselage Nose

A 70x70x70 structured grid shown in fig. 5-1 has been employed for the computations.

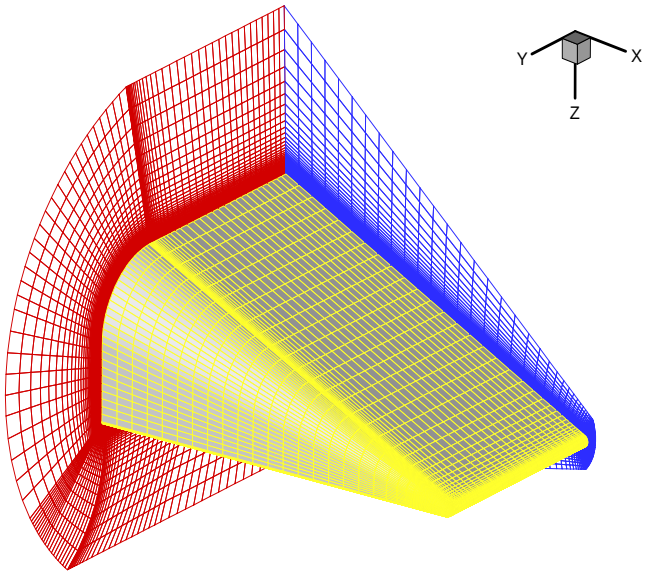

Figure 5-1. Nose Computational mesh

The distributions of the surface temperature and of the corresponding convective heat flux (figures from 5-2 to 5-10 have been computed considering the local radiative equilibrium condition on the wall and an emissivity value ε=0.8).

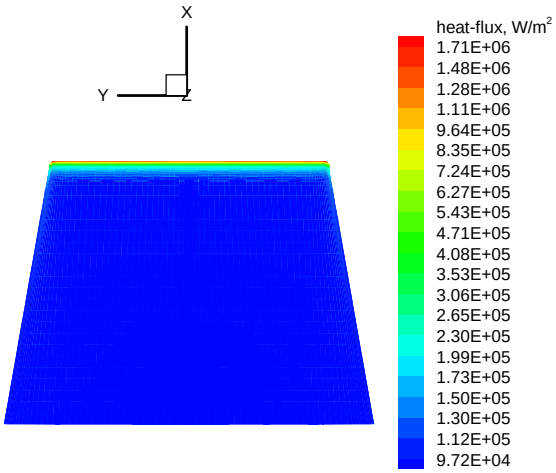

Figure 5-2. Convective Heat flux on the Bottom side AoA=0°. Local Radiative Equilibrium.

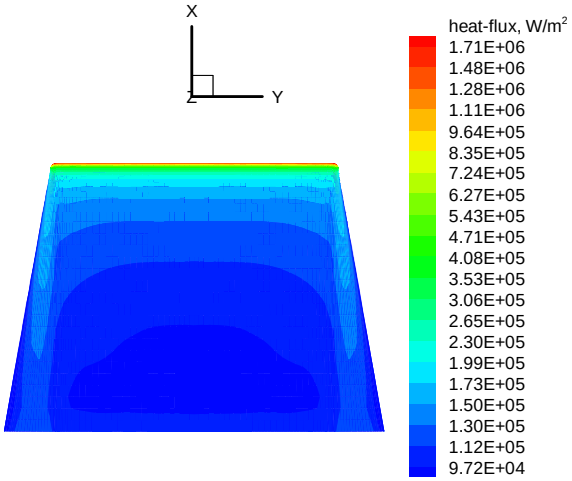

Figure 5-3. Convective Heat flux on the Top side AoA=0°. Local Radiative Equilibrium.

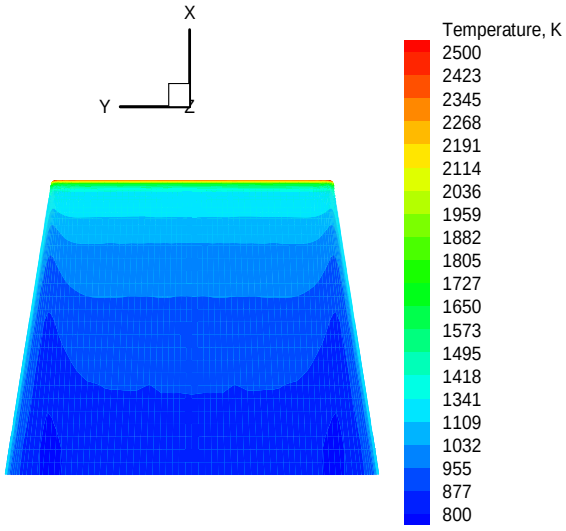

Figure 5-4. Surface Temperature on the Bottom side, AoA=0°. Local Radiative Equilibrium.

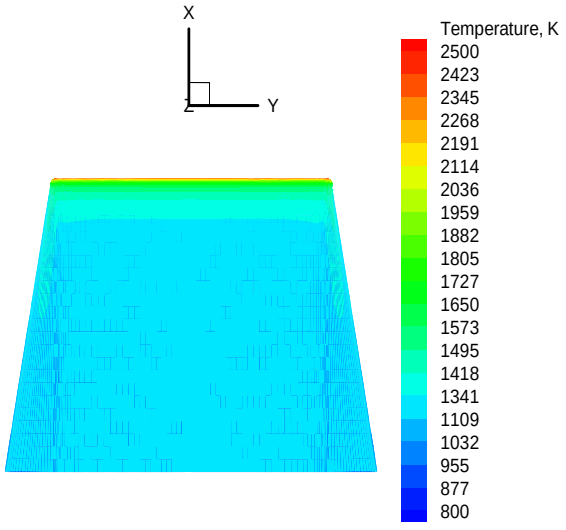

Figure 5-6. Surface Temperature on the Top side, AoA=0°. Local Radiative Equilibrium.

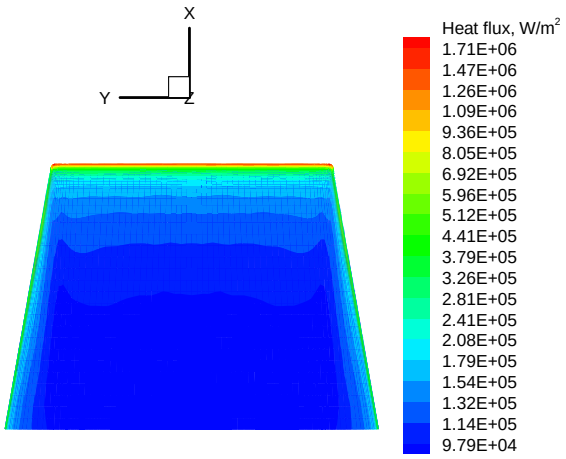

Figure 5-7. Convective Heat flux on the Bottom side AoA=20°. Local Radiative Equilibrium.

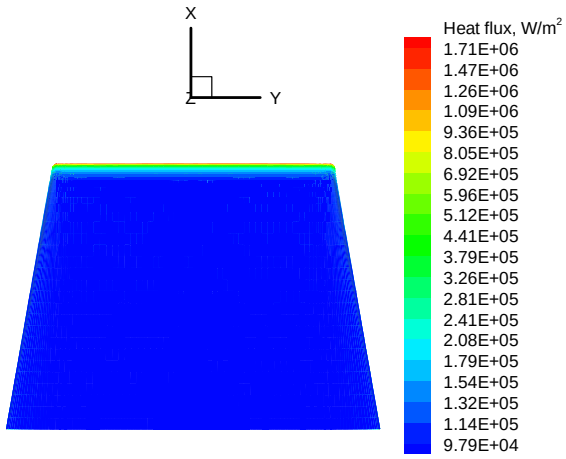

Figure 5-8. Convective Heat flux on the Top side AoA=20°. Local Radiative Equilibrium.

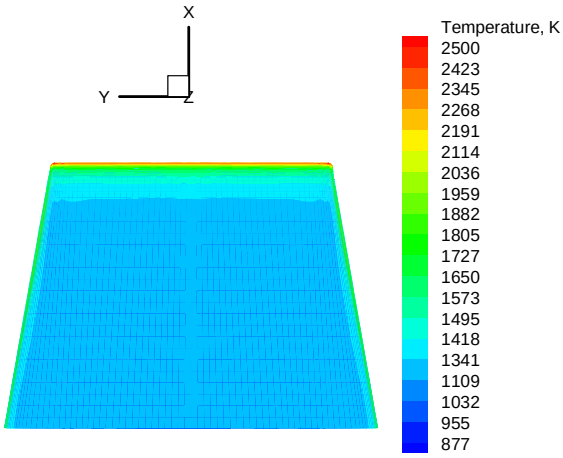

Figure 5-9. Surface Temperature on the Bottom side, AoA=20°. Local Radiative Equilibrium.

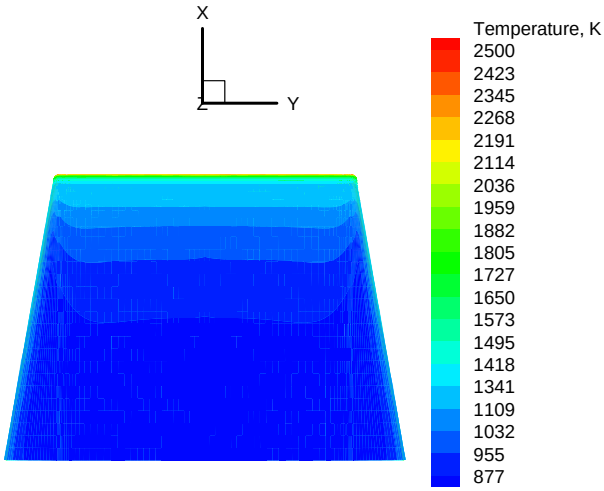

Figura 5-10. Surface Temperature on the Top side, AoA=20°. Local Radiative Equilibrium.

Figures show that the aero-heating along the edge between top and bottom sides is very high(>1500K), because of the low curvature radius at the junction between the upper side (ramp) and the flat bottom.

For this reason the nose lateral edges have been rounded in order to reduce the high peak heating and temperatures. Figures 5-11 show the three different sections analyzed (1 cm , 10 cm and 50 cm distance from the leading edge). Figures 5-12, 5-13 and 5-14 show the computed temperature at the considered sections at the maximum aeroheating flight condition (Z=60Km M=15).

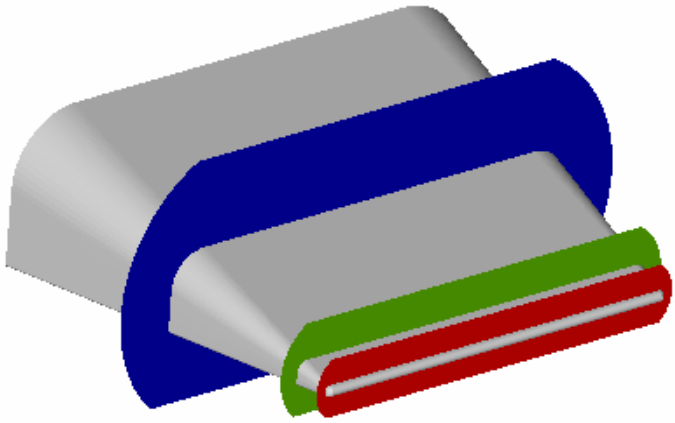

Figure 5-11. Sections at 1cm, 10 cm and 50cm from leading edge.

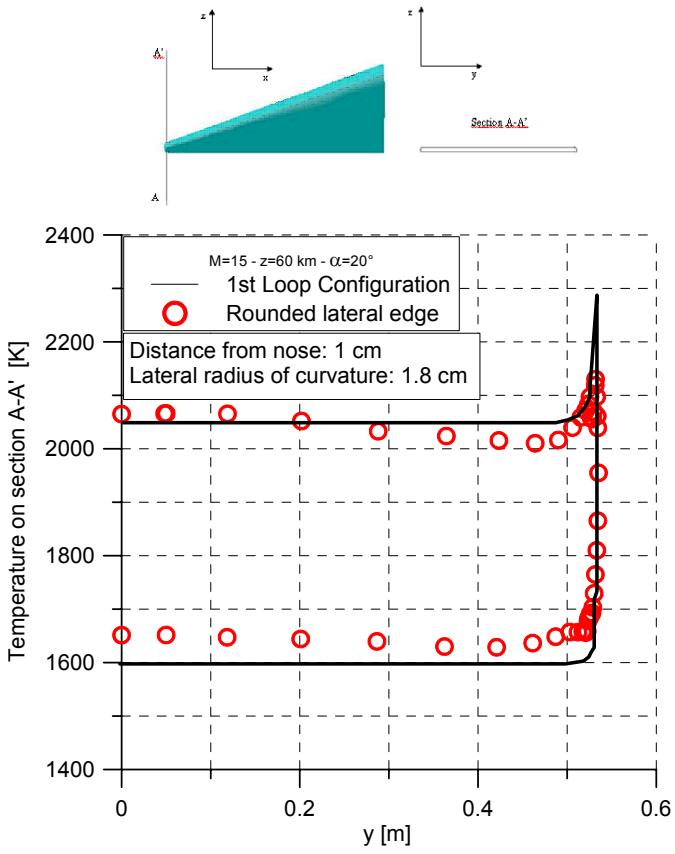

Figure 5-12. Temperature comparison between preliminary and rounded nose geometry along the section at 1cm from leading edge for windside and leeside

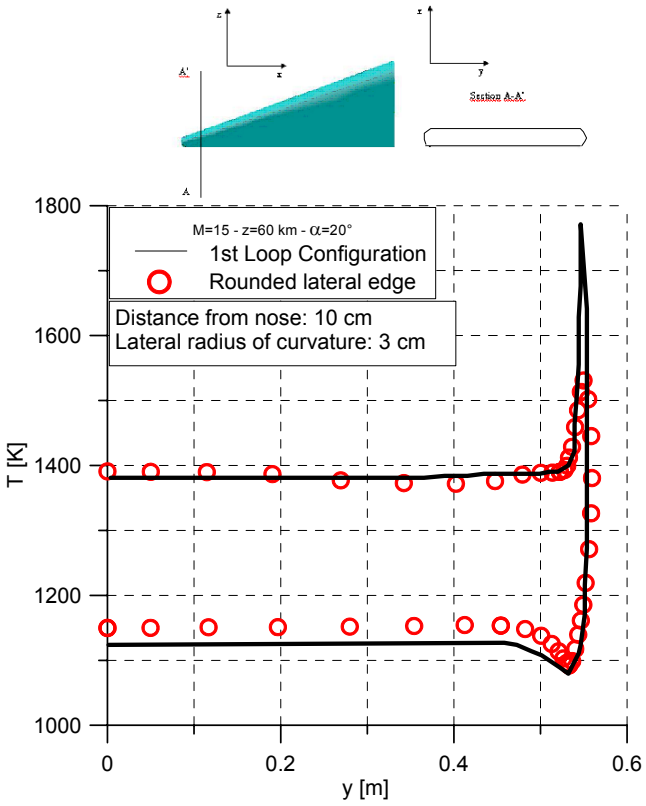

Figure 5-13. Temperature comparison between preliminary and rounded nose geometry along the section at 10cm from leading edge for windside and leeside

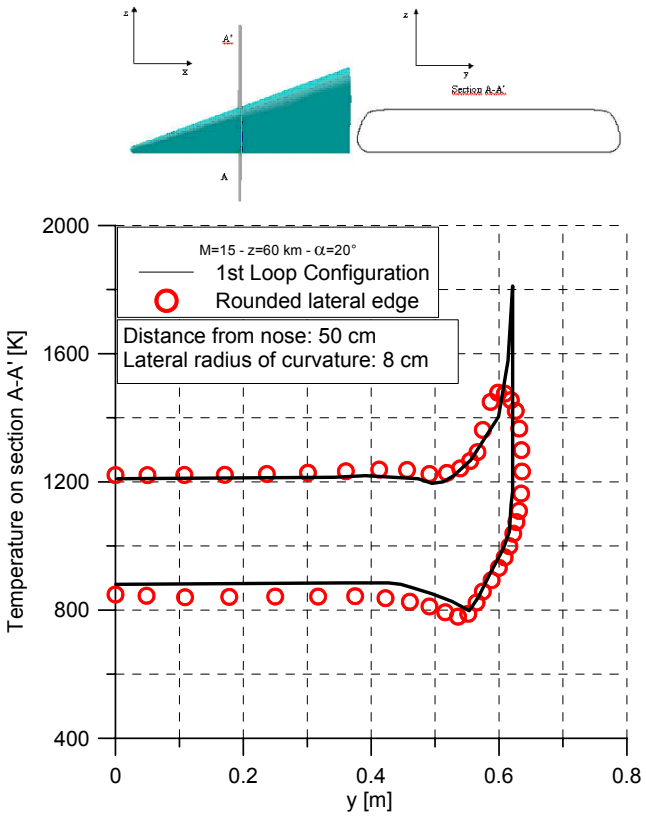

Figure 5-14. Temperature comparison between preliminary and rounded nose geometry along the section at 50cm from leading edge for windside and leeside

The maximum temperature at the lateral edge is reduced by about 200 K, and this must be taken into account according to the limit imposed by the skin, in terms of maximum temperature achievable.

Figure 5-15 shows that in terms of maximum surface temperatures there are negligible differences flying at angles of attack of 0 or 20° . The only change is that in the first case the higher temperatures occur on the top side, while in the former case they occur on the bottom side. The best angle of attack to reduce the thermal load for a flat bottom geometry with a ramp angle of 20° is 10°. In fact, in this condition the top and bottom surfaces exhibit almost the same temperature distributions(fig. 5-16).

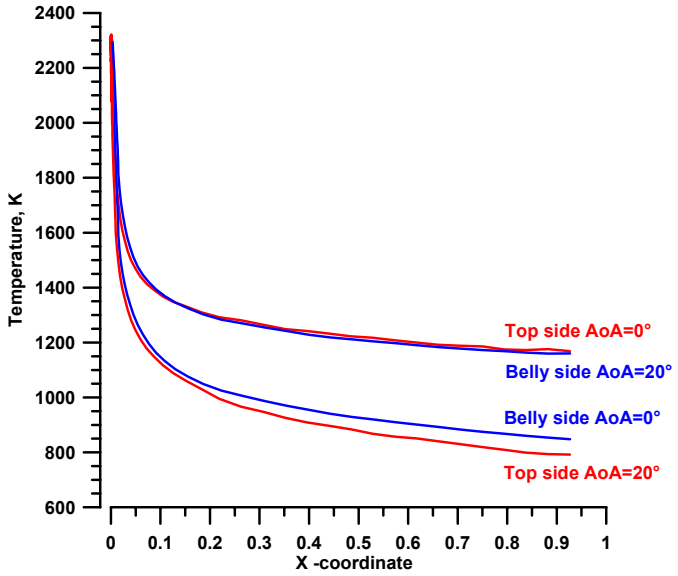

Figure 5-15. Surface temperature on nose symmetry plane at 0 and 20° of the angle of attack.

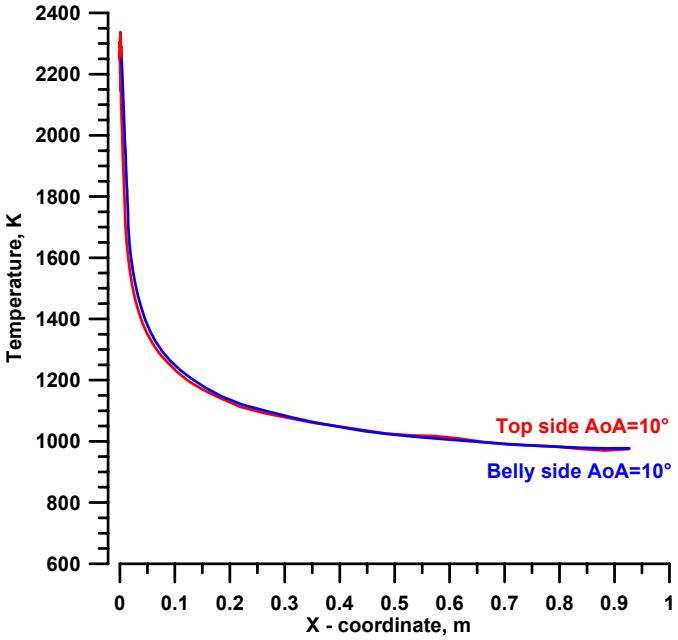

Figure 5-16. Surface temperature on nose symmetry plane at 10° of the angle of attack.

5.2.2 Wing

For the computation of the aerothermodynamic field around the wing a 70x80x80 structured grid shown in fig.5-17 has been employed.

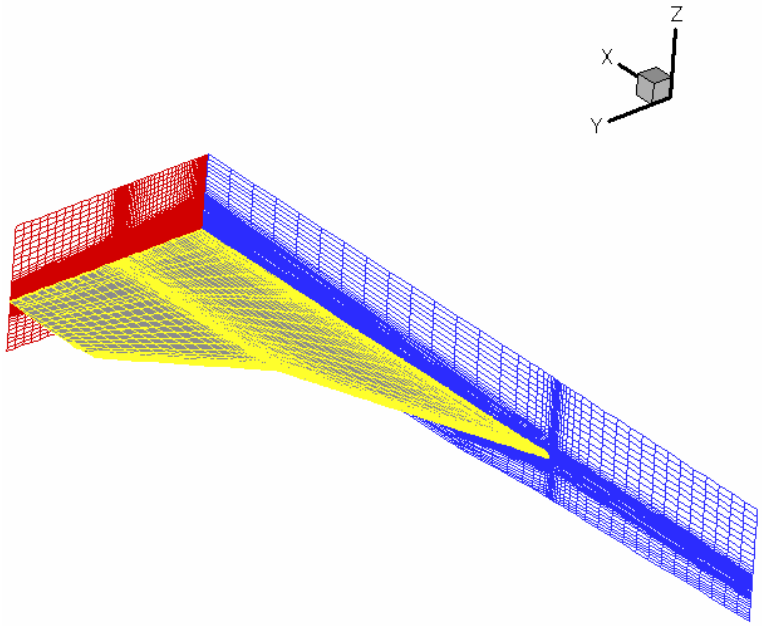

Figure 5-17. Wing Computational mesh

The numerical CFD simulation has been carried out at the same flight conditions and double delta wing at an angle of attack of 20°. Figure 5-18 shows surface temperature distributions. The temperature profiles are shown in fig. 5-19 at two different sections along the wing semi-span (y=0.8m and y=2.5m from the wing root).

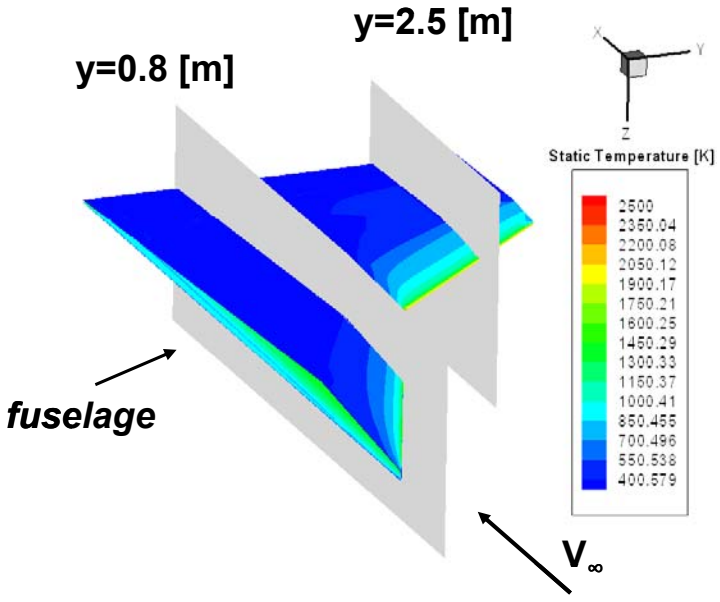

Figure 5-18. Radiative equilibrium temperature at Z=60 Km and M=15

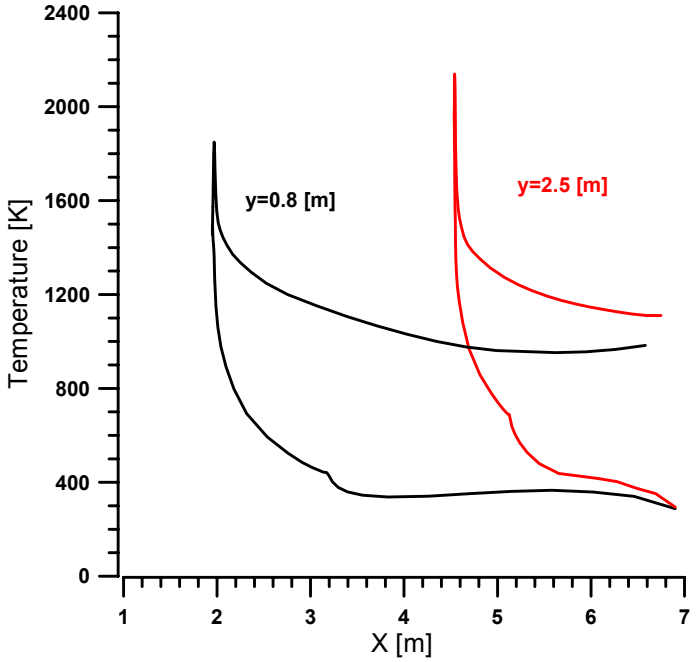

Figure 5-19. Radiative equilibrium temperature at two different sections along wing semi-span (y=0.8m and y=2.5)

The proper design of the wing leading edge TPS must be carried out according to the predicted temperature distributions of figures 5-18 and 5-19.

5.3 A simplified analysis for comparison with Space Shuttle heating.

A figure of merit can be also defined to evaluate thermal load as the average convective heat flux on the wetted area:

$$\bar{q}_{wetted\ area} = \max\left(\frac{\int_S \dot{q}_c\, dS}{\int_S dS}\right)$$

This figure of merit has been computed on a flat plate (L=1m) at different angles of attack both for the Shuttle (α=40°) and for the considered vehicle maximum aeroheating conditions (α=20°). Similar computations have been performed on sphere-cone geometry. The maximum aeroheating condition of the Space Shuttle corresponds to an altitude Z=67Km and a Mach number M=21. The results shown in figure 5-20 provide a sufficient approximation for the centerline of flat belly side vehicles as the Shuttle or the present vehicle and provide an indications of the influence of the angle of attack on the overall heat load.

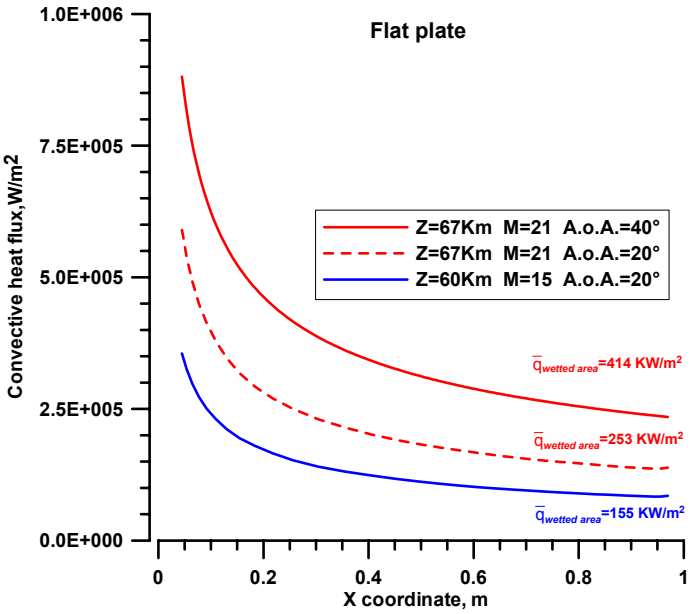

Figure 5-20. Distribution of convective heat flux along a flat plate at different angle of attack for the conditions of maximum aeroheating along the Shuttle(red) and Low Risk(blue) re-entry trajectory

The average convective heat flux in the Shuttle conditions is almost three times the LERV one. In addition, the comparison between two values of the angle of attack (20° and 40°) at the worse Shuttle conditions shows an increase of the average convective heat flux more than 50 per cent.

Figure 5-21 compares the results obtained for axis-symmetric computation of the Shuttle nose and the flat plate computations. The more realistic case of an angle of attack of 40° is, however, worse than axis-symmetric computation (strictly correct only for the stagnation point).

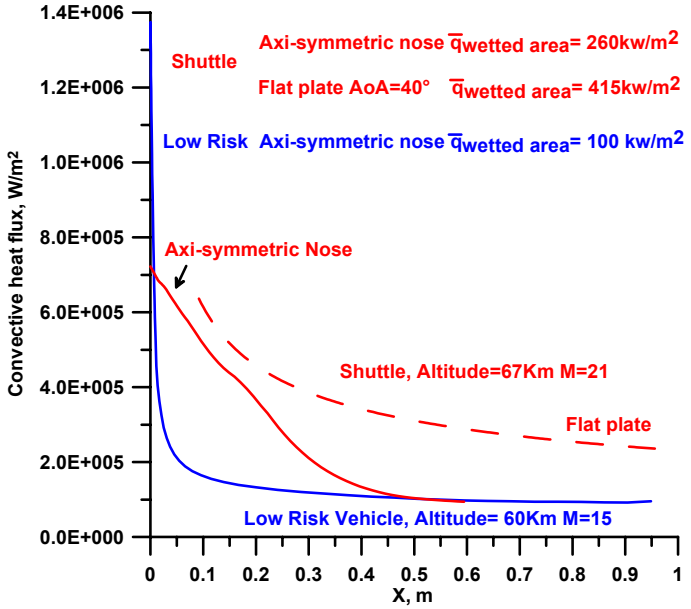

Figure 5–21. Distribution of convective heat flux along a flat plate at 40°of angle of attack (red dashed line),an axis-symmetric sphere-cone (R=0.6m) nose (red solid line) for the conditions of maximum aeroheatingof the Shuttle and axis-symmetric sphere-cone (R=0.01m) nose (blue solid line) for LERV trajectory

Even though the maximum surface heat flux at the stagnation point is higher for the LERV than the Shuttle, considering the fuselage nose, the average heat flux at the maximum aeroheating condition is lower for the low risk vehicle than the shuttle.

5.3.1 Laminar-Turbulent transition evaluation

The design of the re-entry vehicle thermal protection system was based on the following logic: the most severe operational mission was selected to define the design heating environment. One of the major consideration in defining the entry heating environment was the time at which boundary layer transition occurs. Two of the primary parameters that affects boundary layer transition are the local Reynolds number and local Mach number. One prediction method [Leslie Gong, 2000] that has been used for hypersonic transition is based on the following equation that incorporates these parameters:

$$\log \mathrm{Re}_L > \log \mathrm{Re}_t \qquad \log \mathrm{Re}_t = 5.5 + C_M M$$

Based on this equation, if the log of the local Reynolds number (Re_L) at a given point in the trajectory, is greater than the log of the local transition Reynolds number, taking into account compressibility effect related to the local Mach number, then turbulent flow values are calculated. If the log of the local Reynolds number is equal to or less than this value, then laminar flow are calculated. Table 4-1 lists the Mach number coefficients:

Table 5-1. Recommended Mach number coefficients

	C_M
Fuselage	0.2
Wing – no sweep	0.2
Wing – with sweep	0.1

Figure 5-22 shows the transition occurring at two selected points on the fuselage for the Low risk trajectory(x/L=0.9: Z=42Km, t=5200s; x/L=0.1: Z=29Km, t=5500s).

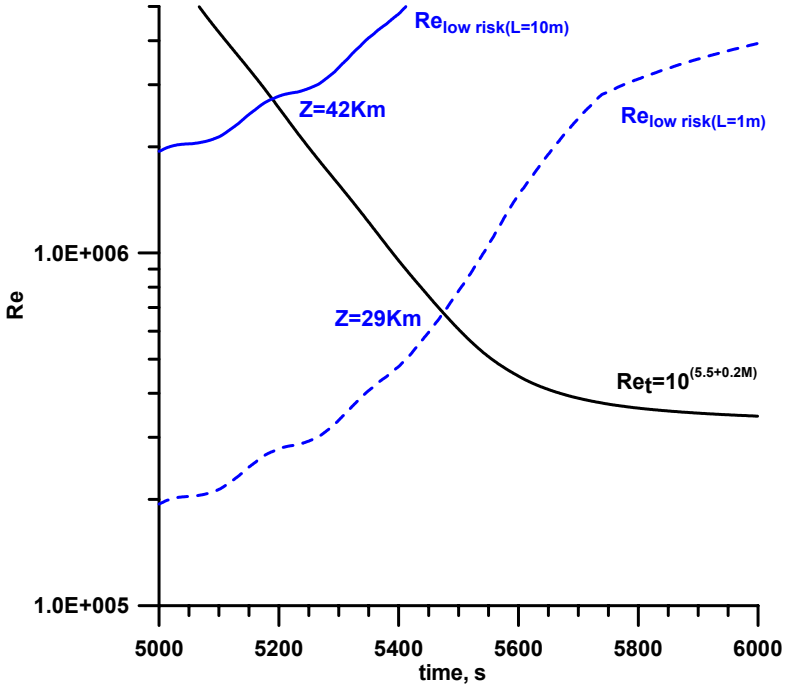

Figure 5-22. Laminar turbulent transition for Low Risk Trajectory at x/L=0.9 and x/L=0.1

Figure 5-23 shows the predicted transition occurring on the Space Shuttle fuselage, based on the same criterion (x/L=0.9: Z=47Km, t=1250s; x/L=0.1: Z=35Km, t=1350s).

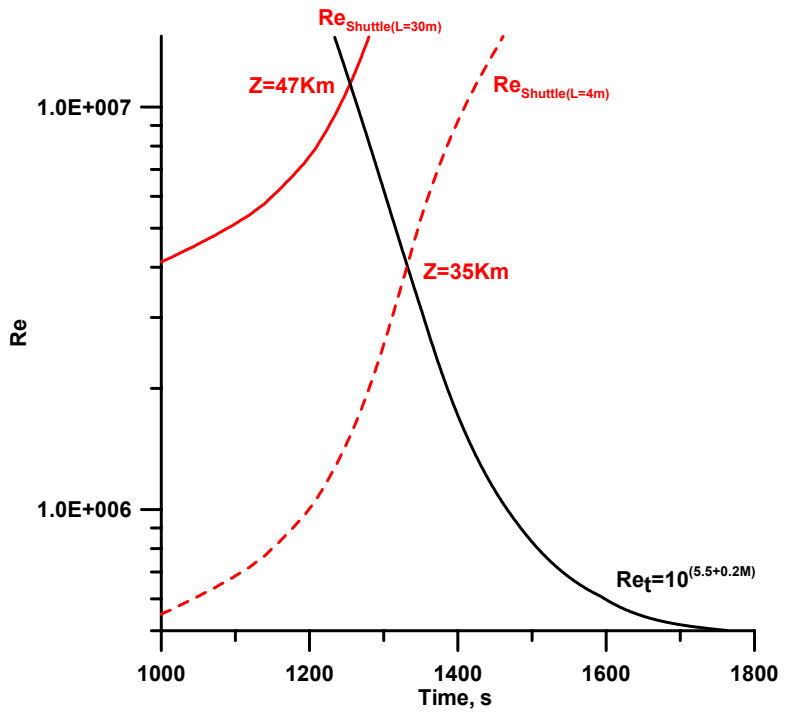

Figure 5-23. Laminar turbulent transition for ShuttleTrajectory at x/L=0.9 and x/L=0.1

To estimate the effect of the turbulent boundary layer on the heat flux along the flat lower surface of the vehicle, semi-empirical formulas [Anderson, 2000] have been applied to

compute the laminar and turbulent surface heat fluxes at different lengths of the body. For a laminar flat plate:

$$\dot{q}_c = 2.53x10^{-9}\ \rho_\infty^{0.5} V_\infty^{3.2} (\cos\phi)^{0.5} \sin\phi\, x^{-0.5}\left(1-\frac{h_w}{H_0}\right) \quad \frac{W}{cm^2}$$

For a turbulent flat plate, for $V_\infty \le 3962 m/s$:

$$\dot{q}_c = 3.89x10^{-8}\ \rho_\infty^{0.8} V_\infty^{3.37} (\cos\phi)^{1.78} (\sin\phi)^{1.6}\ x^{-1.5}\left(\frac{T_w}{556}\right)^{-0.25}\left(1-1.11\frac{h_w}{H_0}\right) \qquad \frac{W}{cm^2}$$

for $V_\infty > 3962 m/s$:

$$\dot{q}\, c = 2.2x10^{-9}\ \rho_\infty^{0.8} V_\infty^{3.7} (\cos\phi)^{2.08} (\sin\phi)^{1.6}\ x^{-1.5}\left(1-1.11\frac{h_w}{H_0}\right) \qquad \frac{W}{cm^2}$$

where:

ρ_∞ = asymptotic density, Kg/m^3;

V_∞ = asymptotic velocity, m/s;

ϕ = local body angle with respect to the free stream;

x = distance measured along the body;

h_w = specific wall enthalpy, J/Kg;

H_0 = specific total enthalpy, J/Kg;

Figures 5-24 shows, respectively, the radiative equilibrium temperature at x/L=0.1 and x/L=0.9.

A comparison with the Space Shuttle trajectory data [Harthum et al., 1983](fig. 5-25) shows that along low risk re-entry trajectory transition occurs at enough low altitudes were aero-heating are not of major concern.

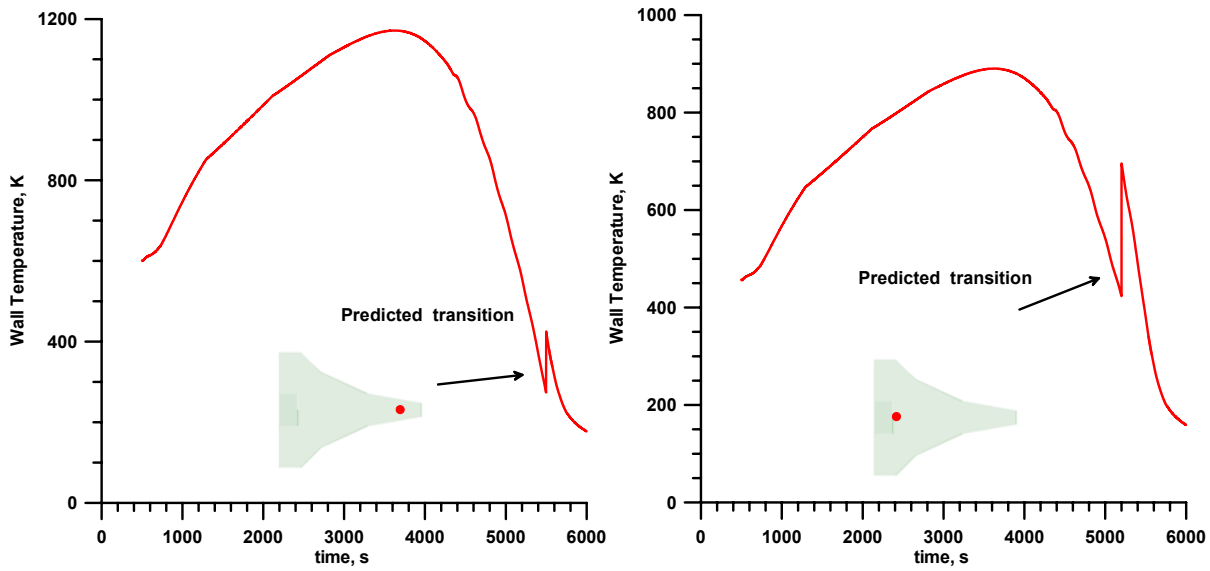

Figure 5-24. RV Temperature history on fuselage lower surface centerline at x/L=0.1 and at x/L=0.9.

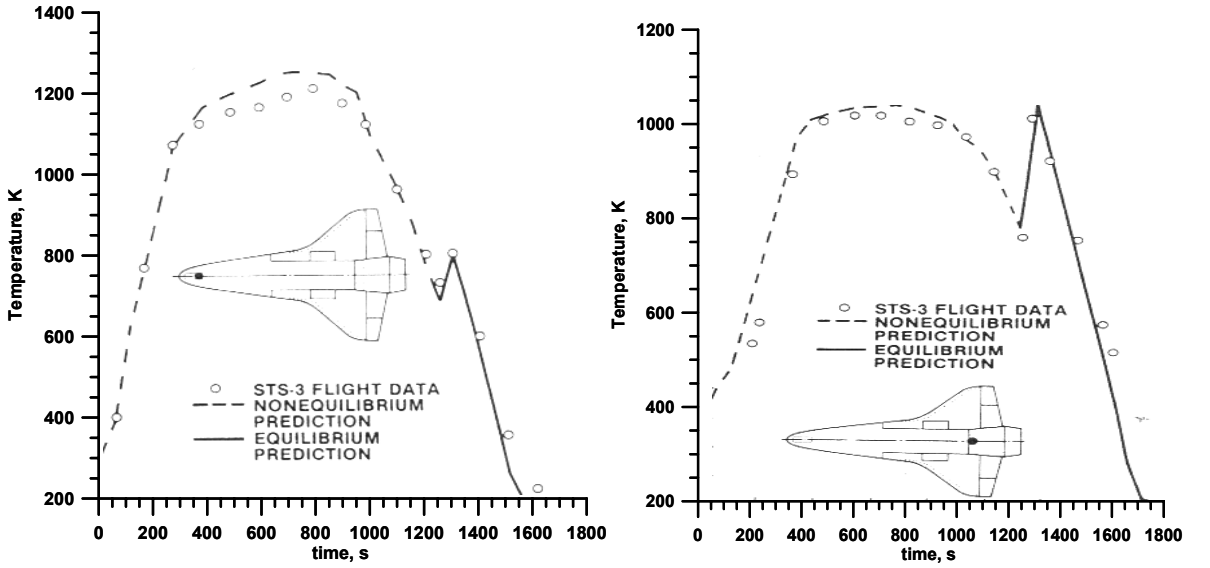

Figure 5-25. Shuttle temperature history on fuselage lower surface centerline at x/L=0.1 and at x/L=0.9.

In particular figure 5-25 shows that at x/L=0.9 the turbulent peak heating for the Space Shuttle is of the same order of magnitude of the laminar peak heating, occurring earlier and at higher altitudes along the trajectory.

The LERV is affected by laminar-turbulent transition; in turbulent regimes the local temperature does not exceed the laminar regime temperature that occurred at previous time.

In order to evaluate the temperature jump caused by the laminar–turbulent transition CFD simulations on a flat plate have been carried out. The considered flight conditions refer to the trajectory point corresponding to an altitude of 42 Km and Mach number 4 with an angle of attack of 20°. For turbulent simulations the Spalart-Allmaras model (1992) has been used.

Figure 4-32 shows that the temperatures achieved with the local radiative equilibrium condition for the turbulent case are lower than the maximum temperature sustainable by any materials that could be utilized for the vehicle. Lower altitudes along the trajectory correspond to lower heat fluxes both in the case of laminar and turbulent flow and therefore to lower temperature achieved by vehicle structure.

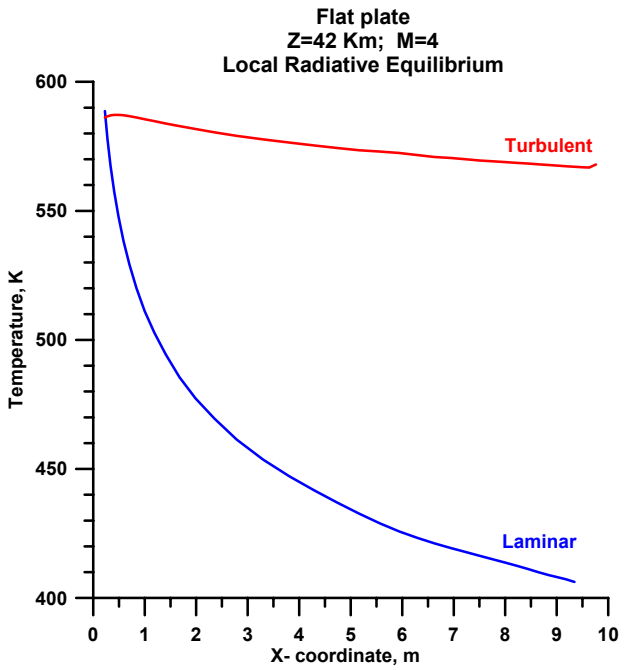

Figure 5-26. Laminar and turbulent wall temperature computations (Z=42Km; M=4)

5.4 Thermal Analysis

At the selected orbital re-entry conditions, convective heat transfer to the surface is partly conducted to the solid and partly re-radiated into the atmosphere. When a steady state is achieved, global radiative equilibrium is established, in the sense that the (surface) overall convective heat flux is perfectly balanced by the overall surface radiative flux. When conduction in the solid may be neglected (i.e. TPS materials with very low thermal conductivity), local equilibrium is established between radiative and convective heat transfer. The corresponding surface temperature will be referred to as "local"(for $\lambda_s=0$) and "global"(for $\lambda_s\neq0$) "radiative equilibrium temperature", respectively [Monti and al., 2005]. TPS realized so far are characterized by refractory low conductivity materials, acting as thermal insulators in order to cover and protect the metallic structure; the heat flux is alleviated making use of blunt configurations. The proposed new scenario for re-entry

vehicles introduce sharp geometries that are subjected to much higher heat fluxes and temperatures that conventional TPS materials would not sustain.

A preliminary configuration of the nose considered for the present computations is represented in fig.5-27 (more realistic configuration will be considered later). A massive nose of UHTC with length 10 cm has been considered, coupled to a thin shell of PM -1000 (1mm thick) The physical properties of the materials are reported in Table 5-2.

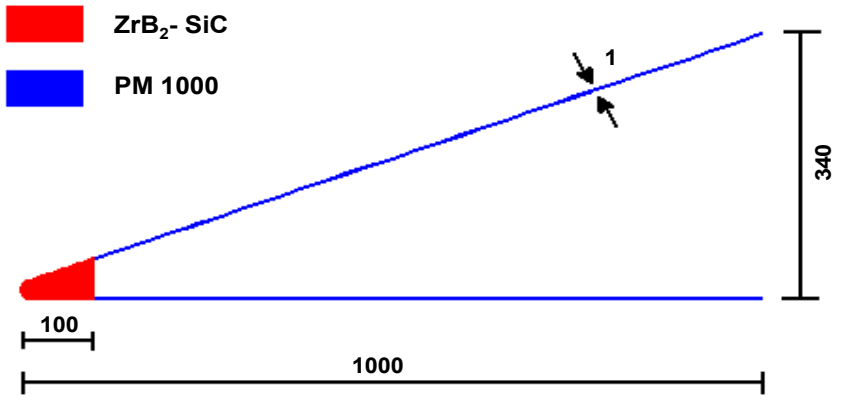

Figura 5-27. Internal configuration of the nose (symmetry plane).The dimensions are in mm.

Table 5-2. Material properties

Material	Density, ρ Kg/m^3	Specific heat, c_p J/Kg K	Th. conductivity, λ_s W/m K	Max temperature achievable K
ZrB_2	6000	628	66	2500(?)
PM-1000	8300	400	15	1400
SiC/SiC	2700	680	22	1800

Figure 5-28 shows the comparison between the symmetry plane surface temperature distributions at the local and global radiative equilibrium at zero angle of attack. Due to the relatively high thermal conductivity of the UHTC the maximum tip temperature decreases and the temperature at the end of the massive UHTC nose increases with respect to the local radiative equilibrium condition. For this condition a temperature of about 1600K occurs at the end of the 100mm massive UHTC.

This temperature value seems to be too high to be sustained by any metallic material. The above results show that this preliminary configuration is not able to guarantee sustainable temperatures on the structure; therefore a trade-off between weight and metallic structure temperature should be carried out.

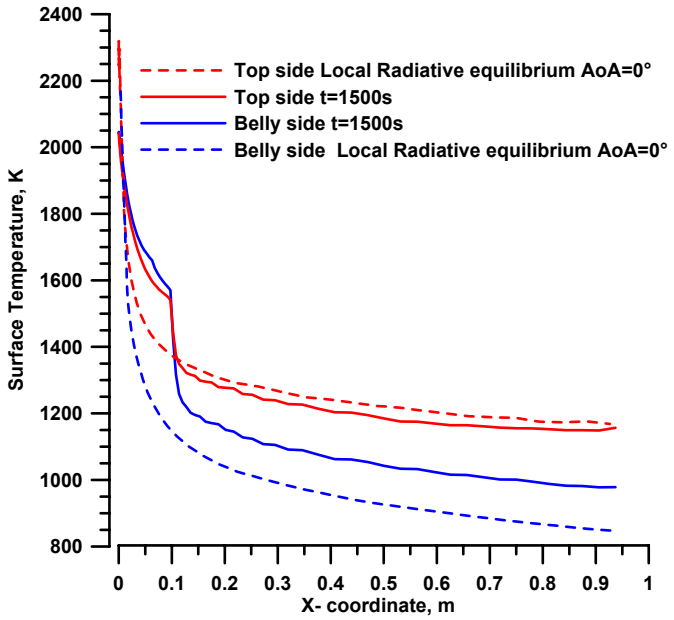

Figure 5-28. Surface temperature on the nose symmetry plane for local radiative condition at zero angle of attack(dashed line) and at1500s during re-entry (solid line)

The possibility to reduce the overall mass of the vehicle while still protecting the vehicle has been explored. For the thermal analysis of the structure, the length of the bulk UHTC has been reduced from 10 cm to 5 cm, and a skin of UHTC 5 cm long has been considered between the bulk and the SiC/SiC (preferred to the heavier PM1000) skin, with a thickness decreasing from 3 mm to 1 mm . Figure 5-29 shows the comparison between the two considered thermal configurations.

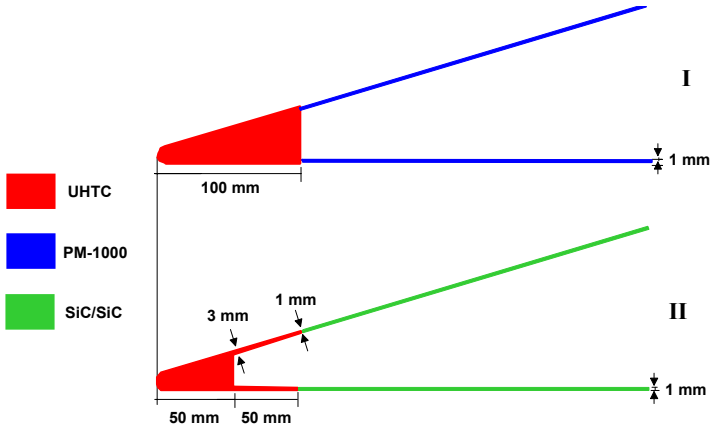

Figure 5-29. Comparison of the preliminary and second configuration

Aerothermal heating computations have been performed considering the conditions corresponding to an altitude of 60 km (M=15). The angle of attack is 20°. The figure 5-30 shows the comparison of the two configurations for the nose leading edge. The comparison shows that the second solution is better from a thermal point of view because also if the

temperature is higher in the UHTC tip than in the first configuration, it is lower at the interface with SiC/SiC skin that can better sustain these high temperature than a metallic skin.

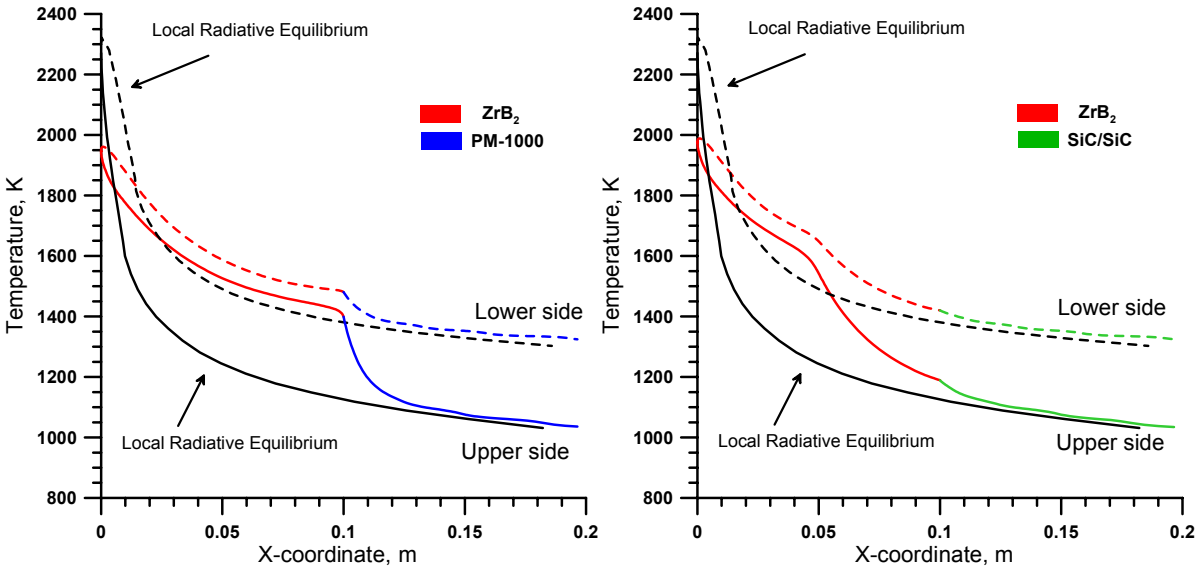

Figure 5-30. Surface temperature of nose leading edges. Configurations comparison

The same configurations of the nose leading edge has been considered for the wing leading edges as reported in figure 5-31.

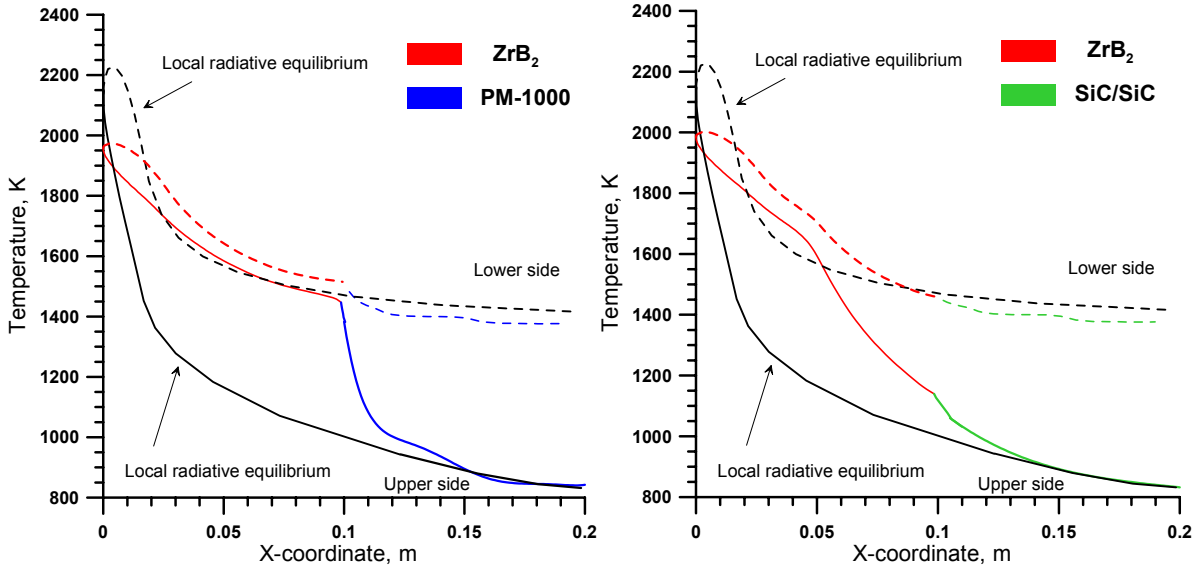

Figure 5-31. Surface temperature of wing leading edges . Configurations comparison

Figures 5-32 and 5-33 show the temperature contours for the nose in the first and second configurations and figure 5-34 and 5-35 show the wing leading edge at the same conditions (Z=60Km; M=15).

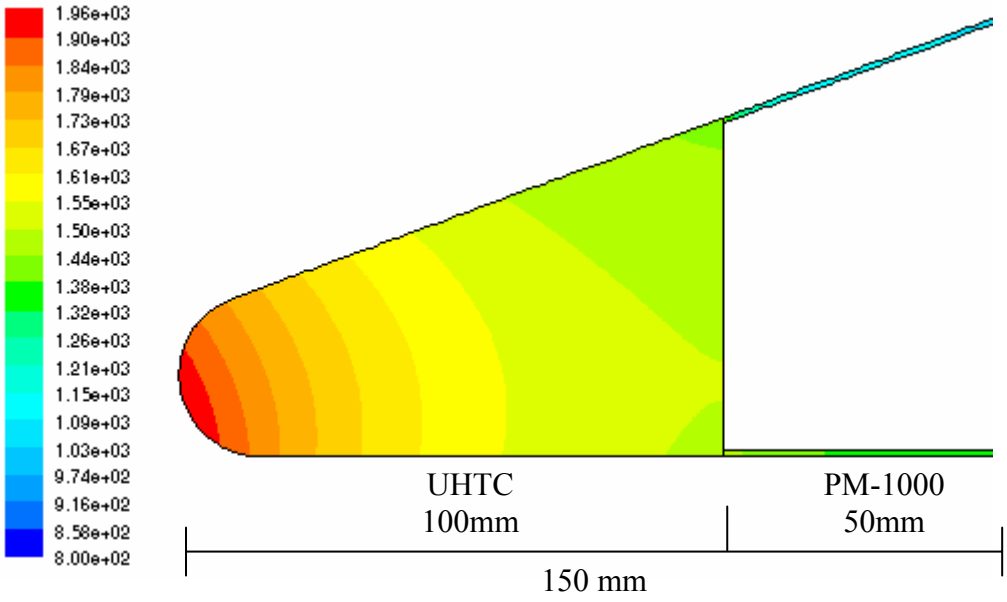

Figure 5-32. Steady state surface temperature contours of nose leading edge in the symmetry plane with preliminary configuration.

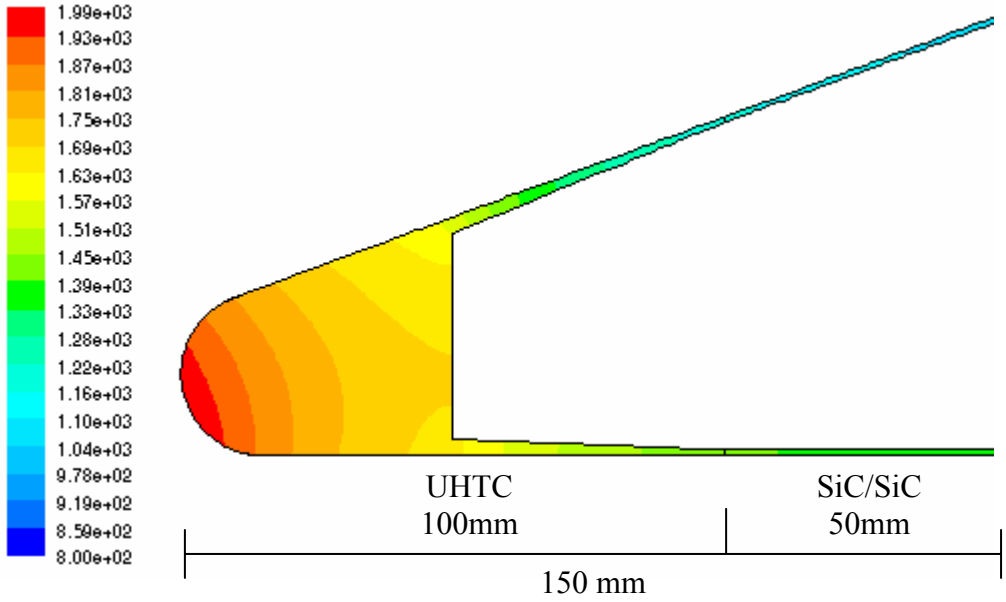

Figure 5-33. Steady state surface temperature contours of nose leading edge in the symmetry plane with second configuration.

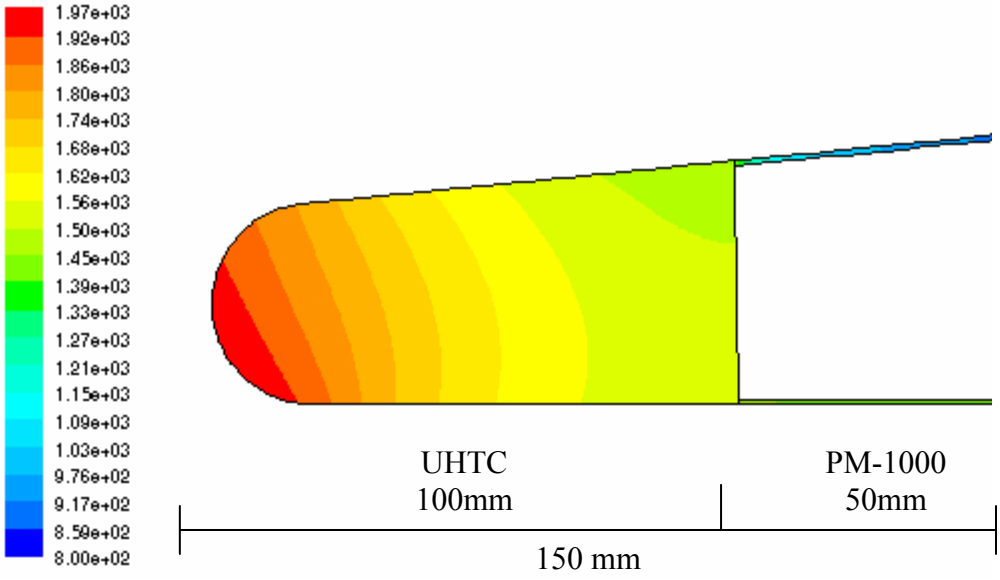

Figure 5-34. Steady state surface temperature contours of wing leading edge in the symmetry plane with preliminary configuration.

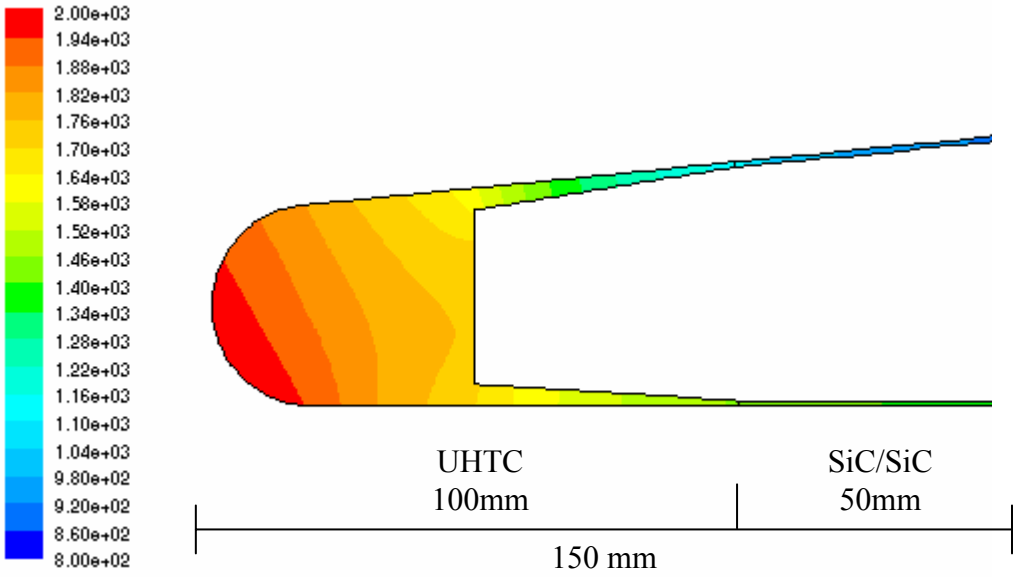

Figure 5-35. Steady state surface temperature contours of wing leading edge in the symmetry plane with 2nd configuration.

5.5 Time- dependent computations

To better evaluate the time evolution of the temperature field in the solid structure, time-dependent computations have been performed considering the nose architecture and the high thermal conductivity of the UHTC materials.

An uncoupled approach, computationally less expensive than the coupled approach, has been employed to compute the time evolution of the surface temperatures and heat flux distribution during re-entry [Savino et al., 2005].

In this approach the vehicle trajectory is discretized in time intervals of Δt=1s. Since the fluid-dynamic characteristic times are typically of the order of few milliseconds, the fluid-dynamic field may be considered steady.

1. The surface distribution of the non-dimensional convective heat transfer ratio, h/h_0 $[h = \dot{q}_c/(H_0 - h_w)]$, where h_0 is the maximum heat transfer coefficient on the body, has been evaluated from the steady heat flux distribution at the flight condition corresponding to Z=60Km and M_∞=15. The main assumption is that this ratio is almost constant along the hypersonic part of the trajectory.

   The maximum heat transfer coefficient h_0 changes continuously along the trajectory according to the instantaneous value of the stagnation point heat flux computed by the Tauber formula [Tauber, 1986].

2. The energy equation in the solid is solved in the time interval (t, $t+\Delta t$), assuming as boundary condition a time-dependent surface heat flux $q(t)$:

$$\dot{q}_c(\bar{t}) = \left(\frac{h}{h_0}\right) h_0(t)\,(H_0(t) - h_w(\bar{t})) - \varepsilon\sigma T_w^4(\bar{t})$$

   with $\bar{t} \in [t, t+\Delta t]$.

   In this way the heat flux heating the structure is the difference between the convective heat flux and the radiative heat flux at each time $\bar{t}$.

   This computation provides the new surface temperature distribution, $T_w(t+\Delta t)$, which is then input to update the surface heat flux, $q_w(t+\Delta t)$, at the flight conditions corresponding to time $t+\Delta$t. The inner wall is considered adiabatic.

Figure 5-36 shows the evolution on the temperature of three points on symmetry plane, corresponding to the leading edge (red) and at the junction between TPS and structure on the top side(green) and on the flat bottom side (blue).

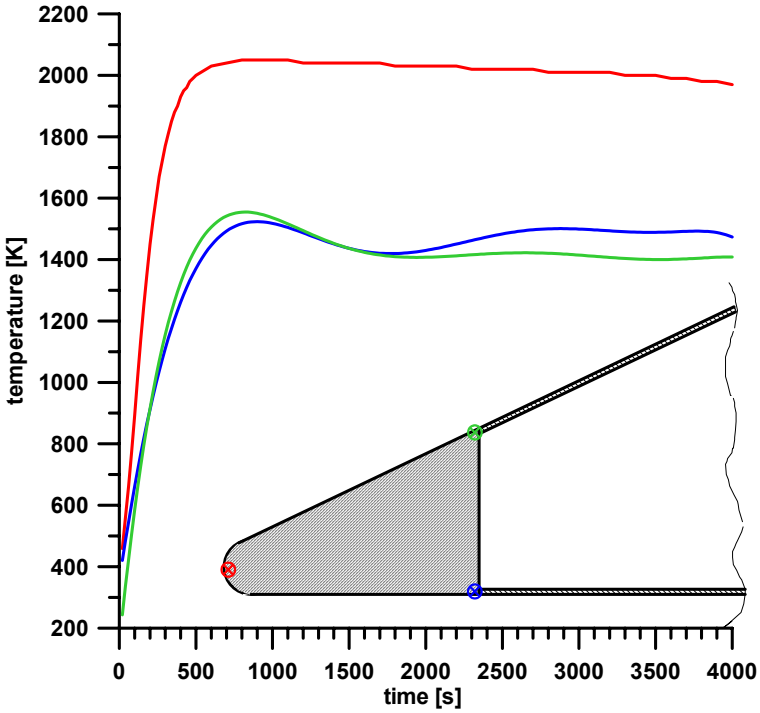

Figure 5-36. Temperature evolution on three control point in the symmetry plane of the nose.

Figure 18 shows that the change of the angle of attack influences the temperature evolution; initially, at high angle of attack the highest temperature at the junction occurs on the belly side; when the angle of attack decreases the temperature grows faster on the upper side until a global radiative equilibrium is reached.

The steady-state is achieved in about 1000 s . This is confirmed by the evolution of the thermal load

$$Q = \int_S (\dot{q}_c - \sigma \varepsilon T_w^4) dS$$

shown in fig. 5-37. About 1000s after the re-entry starting time (corresponding to the entry interface located at an altitude of 120Km) the overall aero-thermal load is almost zero.

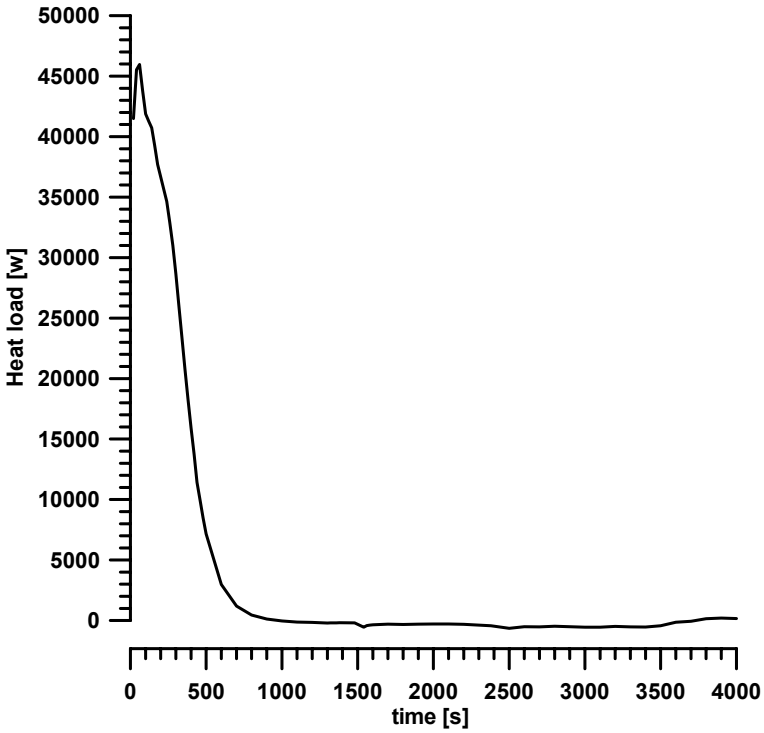

Figure 5-37. Heat load evolution along the trajectory.

Figures 5-38 to 5-46 show the surface temperature distributions and the temperatures in the symmetry plane of the body at three different times along the trajectory (500s, 1000s, and 1500s). The stagnation point temperature reaches the maximum value of 2050K in about 500 s (see also fig.5-36).

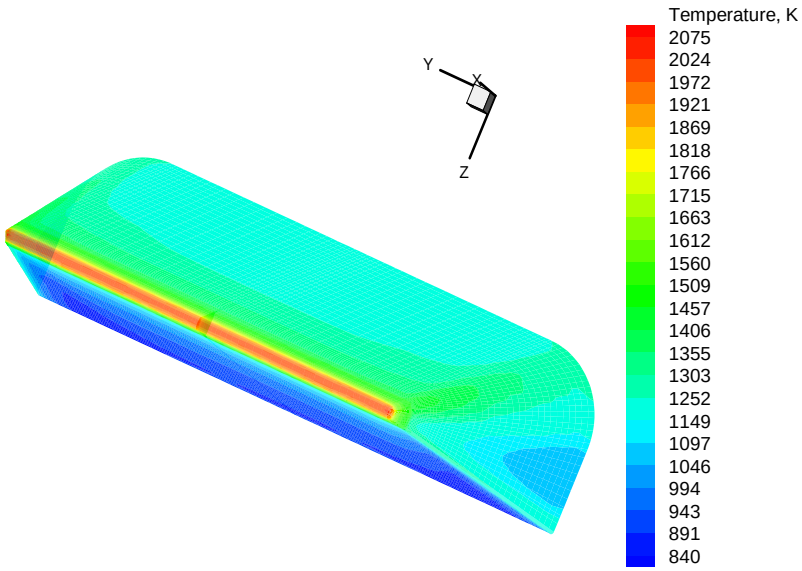

Figure 5-38. Surface temperature at 500s of the re-entry time.

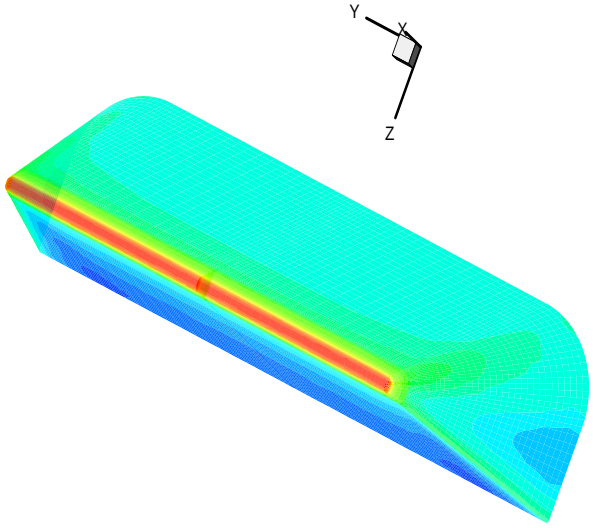

Figure 5-39. Surface temperature at 1000s of the re-entry time.

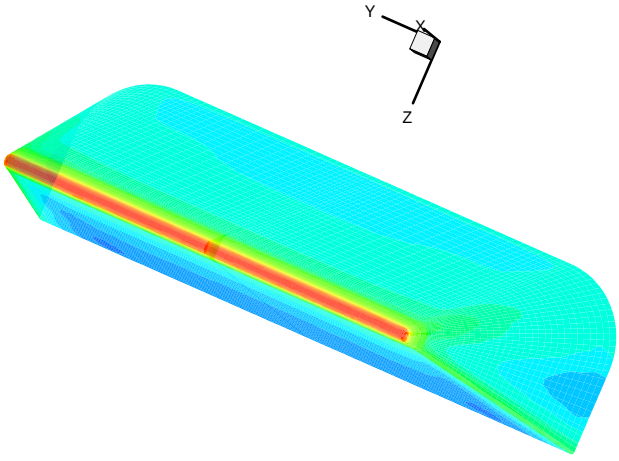

Figure 5-40. Surface temperature at 1500s of the re-entry time.

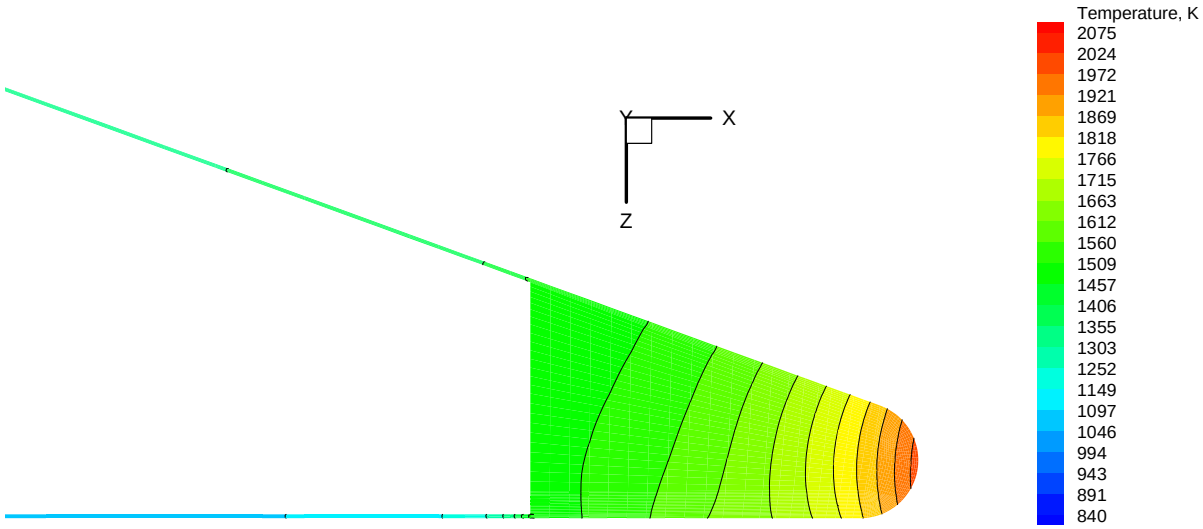

Figure 5-41. Surface temperature in the symmetry plane at 500s of re-entry time.

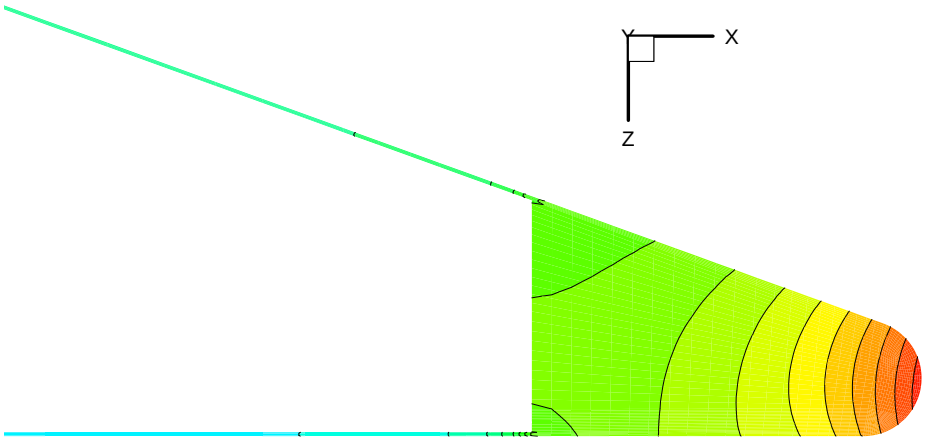

Figure 5-42. Surface temperature in the symmetry plane at 1000s of re-entry time.

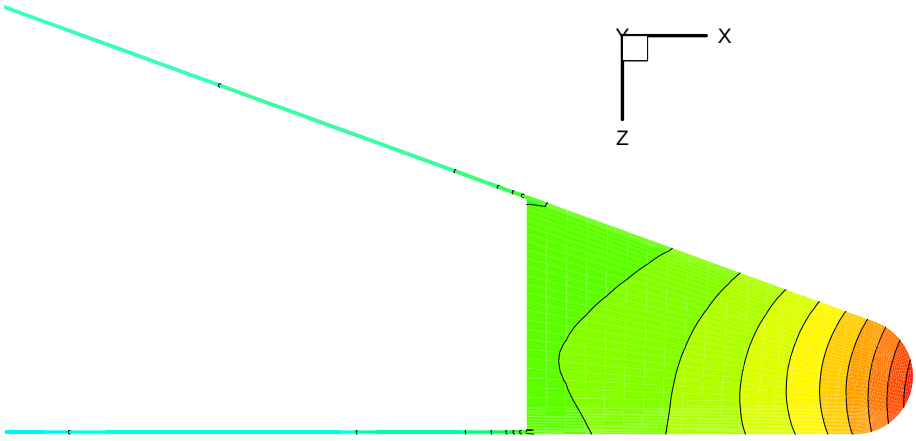

Figure 5-43. Surface temperature in the symmetry plane at 1500s of re-entry time.

Comparing these values with the corresponding local radiative equilibrium temperature, the maximum temperature reached at the stagnation point(2050K) is about 400K lower than the corresponding value in the local radiative equilibrium(fig. 5-44).

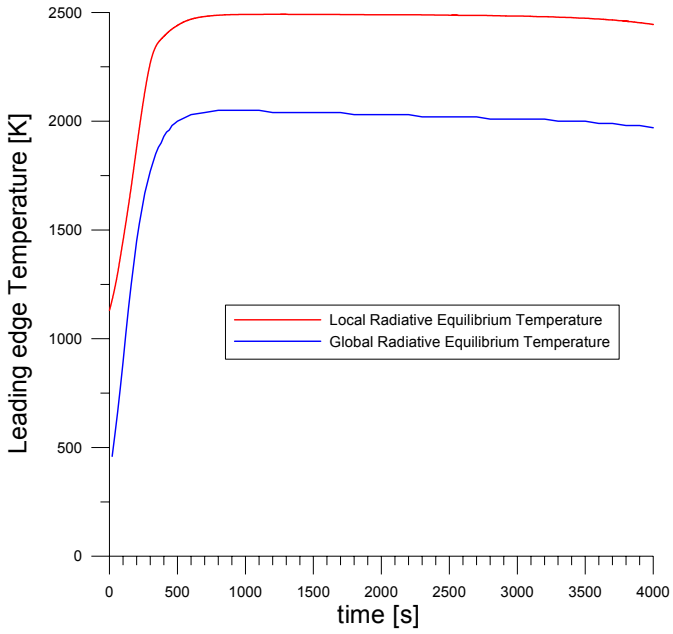

Figure 5-44. Comparison between local and global radiative equilibrium temperature along the trajectory.

5.6 Thermal Protection System Layout

5.6.1 Nose and Wing Leading Edges Concept

Ultra high temperature ceramic (UHTC) material is being considered for leading edge applications on reusable launch vehicles (RLV's) [Tului et al., 2002]. The high use temperature capability they provide may allow for un-cooled, or passively cooled, sharp leading edge vehicle designs. This positively increases the lift to drag ratio for the RLV, and at the same time decreases vehicle complexity.

While ceramic materials have the design benefit of allowing sub-components to run hot, they also provide a design challenge in that these hot sub-components invariably must be in contact with cooler parts elsewhere in the structure. This can lead to the development of severe thermal stresses if the attachment design is not properly addressed.

A cross-sectional view of an original NASA Ames design [Thomas, 1992] for the attachment is shown in fig. 5-45. The design calls for the leading edge to be comprised of multiple UHTC tiles or segments or a one-piece continuous edge[Fossati et al. 2006].

The leading edge is captured between two ceramic matrix composite (CMC) brackets. The brackets are then bolted directly to the ballast of the vehicle. This design approach is very conducive to minimizing stresses in the UHTC leading edge – there are no mechanical fasteners, and the CMC bracket is also a hot sub-component.

The sharp nose should be made of the UHTC ZrB_2-SiC (zirconium di-boride with silicon carbide secondary phase). SiC/SiC (carbon fibre with a melt infiltrated silicon carbide matrix) has been selected for the bracket and skin material.

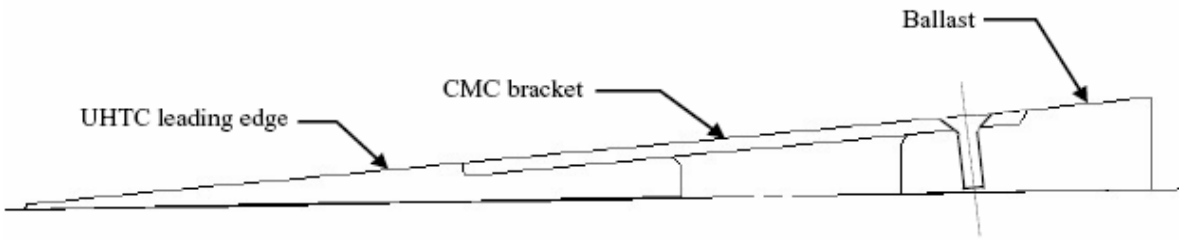

Figure 5-45. The design of leading edges assembly.

5.6.2 Fuselage TPS

The fuselage has the main task to protect the crew, the equipment and the metallic structure from the hot external environment. The proposed configuration consists , as already presented in the third chapter, of an external skin of SiC/SiC (of the order of few mm) and of an internal insulator (fig 5-46).

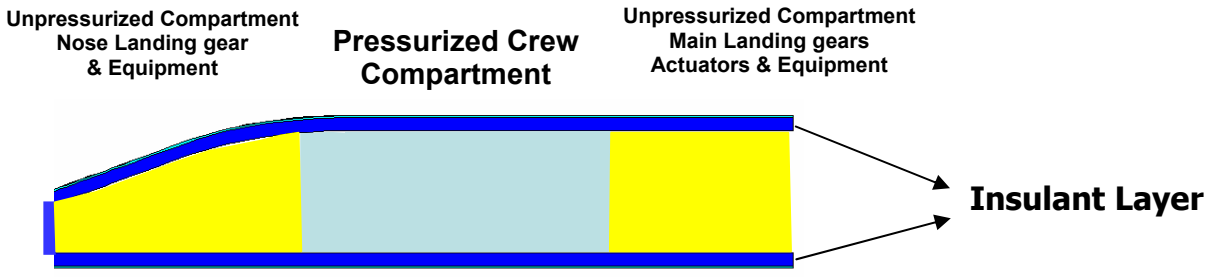

Figure 5-46. Fuselage TPS configuration.

The thermal insulation necessary to protect the crew cabin, tanks, equipment, etc., is shown in fig. 5-47. The internal temperature of the crew and the equipment compartments must remain below the allowed limits; therefore the High Temperature Insulator (HTI) layer must be

dimensioned to accomplish this task. A realistic value of some cm (up to 10-20cm) is foreseen.

An extremely efficient insulator can be provided by a HTI material that exhibits a microporous molecular structure that minimizes heat conduction through the solid (fig. 5-48). The interstices (micro-pores) between the silica particles trap air molecules and prevent them from transmitting heat by convection. The addition of infrared opacifiers in powder form minimizes heat transmission due to radiation. This material is installed in the fuselage inside the main structure.

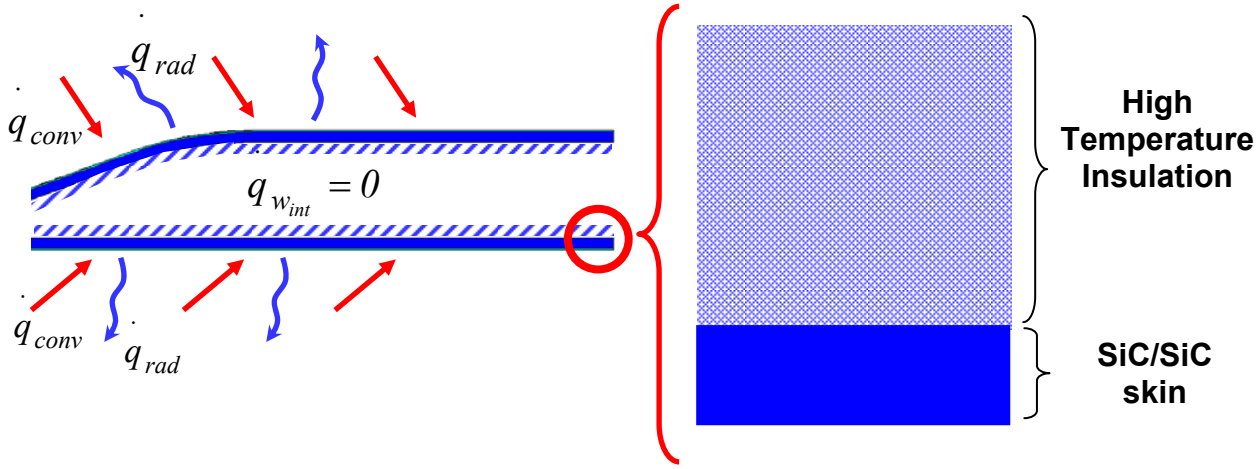

Figure 5-47. Fuselage TPS layout.

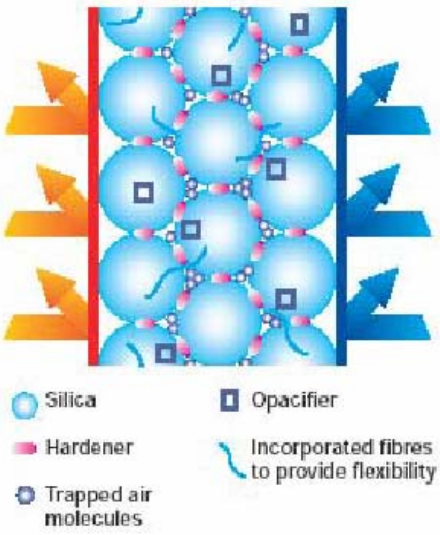

Thermal conductivity (Standard pressure)
At room temp : 0.019-0.021 (W/(m-K))
At 200°C mean temperature: 0.023-0.025 (W/(m-K)
At 600°C mean temperature: 0.034-0.041 (W/(m-K)

Bulk density : 50 – 150 (kg/m3)

Service temperature range : -190 – 1100 (°C)

Figure 5-48. Internal insulator scheme.

5.7 Summary and Comments

The aero-thermal loads on the fuselage nose and on the wing have been identified. The maximum temperature obtained with the local radiative equilibrium conditions was about 2500K almost at the nose leading edge and 2200 K at the wing leading edges. Even these values, that overestimate the expected temperature, seem to be sustainable by UHTC materials.

The geometry of the fuselage nose has been slightly modified rounding the nose lateral edge to reduce the peaks heating observed in the preliminary results.

The preliminary configuration of the TPS has shown a maximum temperature on the UHTC nose tip of 2050 K but the temperature on the metallic skin seems to be too high. For this reason a second configuration has been investigated, a hollow nose of UHTC and a skin of SiC/SiC, instead of the PM1000. This material give also a large benefit in term of weight of the structure. The maximum temperature on the UHTC nose tip is about 2000 K and the SiC/SiC skin achieves temperatures lower than 1500 K. The maximum temperature on the wing leading edges is about 1950 K and the SiC/SiC skin achieves temperatures lower than 1500 K. Also, time dependent computations along the trajectory show similar results.

A simplified analysis of the maximum aero heating between the proposed sharp re-entry configuration and the Space Shuttle nose shows the advantage of the considered sharp configuration compared to the blunt one of the Shuttle.

Engineering formulas have been applied to provide an evaluation of the laminar turbulent transition effect on the proposed re-entry compared to what happens during Shuttle re-entry. The results show that laminar-turbulent transition is not a major issue for the considered trajectory and vehicle.

Some solutions have been identified for the thermal protection system layout.

References

"Fluent 6.2 User's Guide", Fluent Inc., Lebanon, NH, USA, 2004.

Harthum, M. H., Blummer, C. B., Miller, B. A., "Orbiter Windward surface entry heating: Post Orbital Flight Test Program Update", Shuttle Performance Lesson Learned, Part 2, pp 781-804, NASA Conference Pubblication 2283, 1983

Fossati F., D'Aversa E. , Marino G. , Marchetti M., Tului M., "ASA - Exploring Materials and Solutions for Hot Structures to beImplemented in Next-Generation Re-entry/Hypersonic

Vehicles", Proceedings 5th European Workshop on Thermal Protection Systems and Hot Structures Noordwijk, The Netherlands, 17 - 19 May 2006 (ESA SP-631, August 2006).

Leslie Gong, R.Q., "A new method for calculating transient surface temperatures and surface heating for high speed aircraft", NASA Technical Paper 2000-209034, 2000.

Monteverde F., and Bellosi A., Effect of the addition of silicon nitride on sintering behaviour and microstructure of zirconium diboride, *Scripta Materialia*, **46**, 223-228, 2002.

Monti R., Savino R., De Stefano Fumo M., "On Wind Tunnel Testing of Low Risk Re-entry Trajectory", 4th International Symposium Atmospheric Re-entry Vehicles& Systems, March 21-23, 2005, Arcachon, France.

Monti, R., De Stefano Fumo, M**.,** Savino, R., "Thermal shielding of a re-entry vehicle by UHTC materials", 13th International Space Planes and Hypersonic Systems and Technologies Conference, May 16-20, 2005, Capua, Italy. Pubblicato in Journal of Thermophysics and Heat Transfer, Vol. 20, n.3, pp 500-506, 2006.

Savino, R., De Stefano Fumo M., Paterna, D., Serpico, M., "Aerothermodynamic Study of UHTC-based Thermal Protection Systems", Aerospace Science and Technology, Vol. 9, pp.151-160, 2005.

Spalart, P. R. and Allmaras S. R.. "A one-equation turbulence model for aerodynamic flows". AIAA Paper 92-0439, 1992.

Tauber M.E., " A Review of High Speed Convective, Heat-Transfer Computation Methods, NASA Technical Paper 2914, 1989.

Thomas D. J., "Design and Analysis of UHTC Leading Edge Attachment", NASA CR-2002-211505, July 2002.

Tului M., Marino G., Valente T., High Temperature Characterization of an UHTC Candidate Materials for RLV's, Proc. 4th European Workshop 'Hot Structures and Thermal Protection Systems for Space Vehicles', Palermo, Italy, 2002 (ESA SP-521).

Upadhya K, Yang J-M., and. Hoffmann W.P, Materials for ultrahigh temperature applications, Am. Ceram. Soc. Bull., 58, 51-56, 1997.

Zhang G-J., Deng Z-Y., Yang J-F., and Ohji T., Reactive hot pressing of ZrB_2-SiC composites, *J. Am. Ceram. Soc.*, 83, 2330-2332,2000.

CHAPTER 6

CONCLUSIONS

The object of this work was to demonstrate the feasibility of a winged body with high aerodynamic efficiency and with sharp leading edges for a Low Earth Orbit re-entry by means of a new re-entry strategy, containing mechanical and thermal stresses, within the limits allowed for both the spacecraft and the flight crew.

In contrast to conventional re-entry missions, the proposed strategy drastically extends the re-entry duration. These trajectories are characterized by a long-duration glide phase in the upper atmosphere. As a consequence, the kinetic energy is dissipated into thermal energy over a longer period of time, reducing drastically heat flux, dynamic pressure and vehicle deceleration compared to conventional re-entry vehicles. Furthermore, down- and cross-range capability of the vehicle are drastically increased whereas landing velocity may be reduced to some 40 m/s, providing much more flexibility with regard to the selection of landing sites including conventional airports/runways.

These aspects are favorable with regard to the risk of a vehicle failure, but also with regard to crew comfort, making these trajectories and the related vehicles attractive for any human mission like ISS-return or space tourism, but also for the return of ill or de-conditioned crew from space missions.

The main results achieved during this study are the identification of an innovative system concept for a space vehicle re-entering from LEO and the definition of a satisfactory vehicle configuration based on the exploiting of the Boundary Layer Thermal Protection System concept and the use of innovative high temperature materials as the UHTC. In particular, thanks to the sharp leading edges, the aerodynamic analysis shows a high aerodynamic efficiency and a good manoeuvrability at landing conditions.

A numerical code has been developed and validated in order to compute the re-entry trajectories. The flight corridor constraining these re-entry trajectories has been defined, based on some fundamental equations of flight physics and aero-thermal heating and feasible de-orbiting manoeuvres have been identified. The comparison with the re-entry trajectory of the Space Shuttle has shown the advantage of the proposed strategy.

The aero-thermal loads on the fuselage nose and on the wing have been identified and the expected temperatures are sustainable by UHTC materials.

Two different configurations have been analyzed for the nose and wings. The second configuration based on a hollow nose of UHTC and a skin of SiC/SiC, instead of the PM1000 gave the best results in term of temperature of the junctions. This material give also a large benefit in term of weight of the structure. Time dependent computations along the trajectory

has shown the effectiveness of the strategy for as concern the thermal load: when radiative equilibrium condition has achieved the net heat entering the vehicle's structure is zero.
A simplified analysis of the maximum aero heating between the proposed sharp re-entry configuration and the Space Shuttle nose shows the advantage of the considered sharp configuration. Engineering approach has shown that laminar-turbulent transition is not a major issue for the considered trajectory and vehicle. Some solutions have been also identified for the thermal protection system layout.

The positive results achieved during this study suggest the investigations of some other aspects necessary for the development of the concept. They are summarized below:

- Effects of control surfaces deflection on aerodynamic dataset.
- Effects of non-equilibrium chemistry on the aerodynamic dataset.
- Lateral-directional aerodynamic database. Stability limits.
- Transition from supersonic to subsonic regime.
- Effect of the landing gear down on the aerodynamic of the landing configuration .
- A six degree of freedom model for the re-entry trajectory taking into account the attitude dynamics of the vehicle.
- Detailed analysis of aerothermal loads on the complete vehicle.
- Aeroheating conditions at different ailerons/elevons setting.
- Thermo-structural analysis and solutions.

Finally I would conclude using some words of Whitmore and Dunbar appears in a paper of few years ago:
"If a blunt lifting body or capsule shape is selected as the OSP configuration, then there is no hope of ever evolving the design into a configuration with a high degree of orbital manoeuvre agility".